THERMODYNAMIC OPTIMIZATION OF A PLANAR SOLID OXIDE FUEL CELL

James Christopher Ford
G.W. Woodruff School of Mechanical Engineering
Georgia Institute of Technology

Dissertation Submitted in Partial Fulfillment for Doctor of Philosophy

Georgia Institute of Technology
December 2012

Thermodynamic Optimization of a Planar Solid Oxide Fuel Cell

Approved by:

Dr. Samuel Graham, Co-Advisor
School of Mechanical Engineering
Georgia Institute of Technology

Dr. Andrei Fedorov
School of Mechanical Engineering
Georgia Institute of Technology

Dr. J. Rhett Mayor
School of Mechanical Engineering
Georgia Institute of Technology

Dr. Comas Haynes, Co-Advisor
Center for Innovative Battery and Fuel Cell Research
Georgia Tech Research Institute

Dr. Meilin Liu
School of Material Science and Engineering
Georgia Institute of Technology

Dr. A. Alan Burke
Division of Energy Sciences
Naval Undersea Warfare Center

Date Approved: August 29, 2012

ACKNOWLEDGEMENTS

I would like to first give thanks to my Lord and Savior Jesus Christ. It has been through His strength and Holy Spirit that have guided me through the completion of this long and challenging journey. Through the many ups and downs, trials and tribulations, it has been God's unfailing love that has carried me on. I humbly acknowledge His grace and mercy at every juncture of this Ph.D. journey. I am amazed to look back at the spiritual journey that accompanied this research journey. I came into this program with only a brief introduction to Jesus. I leave this program knowing Him intimately with numerous experiences that testify to His goodness and that He lives. I love you Jesus! Thank you for saving my soul and changing my life!

To my wonderful family, thank you for your continued love, support, and encouragement. Dad, thank you for planting seeds of scientific curiosity and research. Thank you so much for sharing your love of knowledge and learning. Your humorous words of, "Boy, use your head for me than a hat rack," have allowed me to laugh during tough research moments. I love you so much Dad! Mom, thank you so much for planting seeds of determination, encouragement, and academic excellence. Your undying faith in me has been a bright light during many dark times. I love you so much Mom! To my amazing baby sister and "Wonder Twin" Dr. Knatokie Marie Ford, thank you for truly being there *with* me through this arduous journey. We have shared this Ph.D. journey together. You have understood the battles that I have gone through better than anyone else. I am thankful to God to call you sister and dear friend. I love you baby sister! To my big brother Robert, I appreciate your unique love and

respect you have shown me through this time. I love you big brother! To my big sister Angie, I appreciate you so much for setting an awesome example of academic excellence and Christ like character. I fondly remember your great influence on both my academic and spiritual journey. I love you big sister!

To my brothers of C.O.D.E. (Christian Organization of Dynamic Engineers), thank you. I don't know where I would be without your love, support, and encouraging words. You guys gave meaning to the last two years of this Ph.D. journey. To the rest of my spiritual family, thank you so much for your words of encouragement, prayer, and undying faith in me. I cannot praise God enough for the mighty men and women of God who have supported me all these years.

To my lead advisor Dr. Comas Haynes, thank you for your patience, guidance, and love. It has been quite a journey since I met you as an undergraduate more than 11 years ago. I appreciate and respect the man of God that you are. God has taught me so many lessons from your life and our relationship. Thank you for being God's servant. To my co-advisor Dr. Sam Graham, thank you for your wise counsel, encouraging spirit, and sense of humor. You have a unique knack for providing clarity and levity in the tensest of moments. I would also like to thank the rest of my esteemed reading committee, Dr. Andrei Fedorov, Dr. J. Rhett Mayor, Dr. Meilin Liu, and Dr. A. Alan Burke. I appreciate your guidance, support, and provocation to excellence. May God bless all of you.

Last and definitely not least, I want to thank all my Georgia Tech family. I acknowledge former and current research group members, study group members, faculty, and staff. I

remember you all. Your kind words and support have meant so much. May God bless you all for enriching my life.

TABLE OF CONTENTS

LIST OF TABLES

LIST OF FIGURES

SUMMARY

Solid oxide fuel cells (SOFCs) are high temperature (600°C-1000°C) composite metallic/ceramic-cermet electrochemical devices. There is a need to effectively manage the heat transfer through the cell to mitigate material failure induced by thermal stresses while yet preserving performance. The present dissertation offers a novel thermodynamic optimization approach that utilizes dimensionless geometric parameters to design a SOFC. Through entropy generation minimization, the architecture of a planar SOFC has been redesigned to optimally balance thermal gradients and cell performance. Cell performance has been defined using the 2^{nd} law metric of exergetic efficiency. One constrained optimization problem was solved. The optimization sought to maximize exergetic efficiency through minimizing total entropy production while constraining thermal gradients. Optimal designs were produced that had exergetic efficiency exceeding 92% while maximum thermal gradients were between 219 °C/m and 1249 °C/m. As the architecture was modified, the magnitude of sources of entropy generation changed. Ultimately, it was shown that the architecture of a SOFC can be modified through thermodynamic optimization to maximize performance while limiting thermal gradients. The present dissertation highlights a new design methodology and provides insights on the connection between thermal gradients, performance, sources of entropy generation, and cell architecture.

1 INTRODUCTION

1.1 Problem Statement

One of the attractive benefits of solid oxide fuel cells (SOFCs) is their high specific energy and energy density relative to other energy conversion devices. Figure 1.1 and Table 1.1 compare the specific power and energy of various electrochemical energy conversion technologies. Despite their high specific energy, fuel cells have relatively low specific power relative to other electrochemical energy conversion technologies. This has prompted fuel cell manufacturers to focus upon improving specific power (W/kg) and power density (mW/cm^2). Accordingly, fuel cell designers have focused on designing for maximum power density. While high power density is an attractive and logical performance metric, it introduces the possibility for larger temperature gradients and may be a potentially limited metric in assessing the performance of a SOFC. As a result, the design for high power density approach has come at the detriment of the material reliability. Though fuel cell researchers are aware of the heat transfer issues in SOFCs, there has been little work in the way of offering fuel cell designs or a design approach that accounts for temperature gradients and differences.

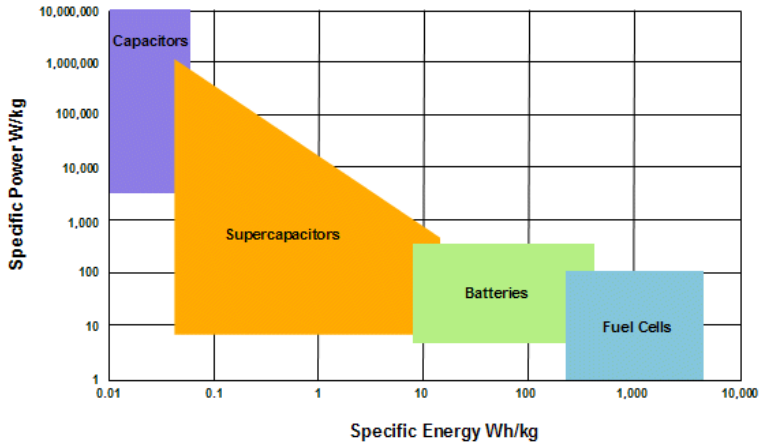

Figure 1.1. Comparison of specific power and specific energy of energy storage technologies (graphic courtesy of Cap-XX, Ltd, http://www.cap-xx.com/resources/reviews/pwr-v-enrgy.htm)

Table 1.1. Comparison of energy storage technologies. (courtesy of Cap-XX, Ltd, http://www.cap-xx.com/resources/reviews/strge_cmprsn)

Property	Supercapacitors	Capacitors	Fuel Cells	Batteries
Operating Temperature	-40 to +85 °C	-20 to +100 °C	+25 to +1000 °C	-20 to +65 °C
Operating Voltage	2.3V - 2.75V/cell	6 to 800 V	~0.6 V / cell	1.25 to 4.2 V / cell
Life	30,000+ hrs average	>100,000 cycles	1500 to 10,000 hrs	150 to 1500 cycles
Weight	1 g to 2 g	1 g to 10 kg	20 g to over 5 kg	1 g to over 10 kg
Specific Power	10 to 100 kW/kg	0.25 to 10,000 kW/kg	0.001 to 0.1 kW/kg	0.005 to 0.4 kW/kg
Specific Energy	1 to 5 Wh/kg	0.01 to 0.05 Wh/kg	300 to 3000 Wh/kg	8 to 600 Wh/kg
Pulse Load	Up to 100 A	Up to 1000 A	Up to 150 mA / cm^2	Up to 5 A

A planar anode-supported SOFC cell shown in Figure 1.2 is a metallic/ceramic-cermet composite composed of a stainless steel interconnect, a nickel-yttria stabilized zirconia (Ni-YSZ) anode, a YSZ electrolyte, and a strontium doped-lanthanum manganite (LSM) cathode. The SOFC produces electricity via electrochemical reactions that cogenerate heat. This generated

heat causes thermal expansion of the composite layers. Such thermal expansion induces a mechanical stress which can degrade performance. During steady-state operation and transitional scenarios such as start up, shut down, a thermal cycle, and a load transient, thermal stresses can cause material degradation such as crack and blister formation, and delamination as shown in Figure 1.3.

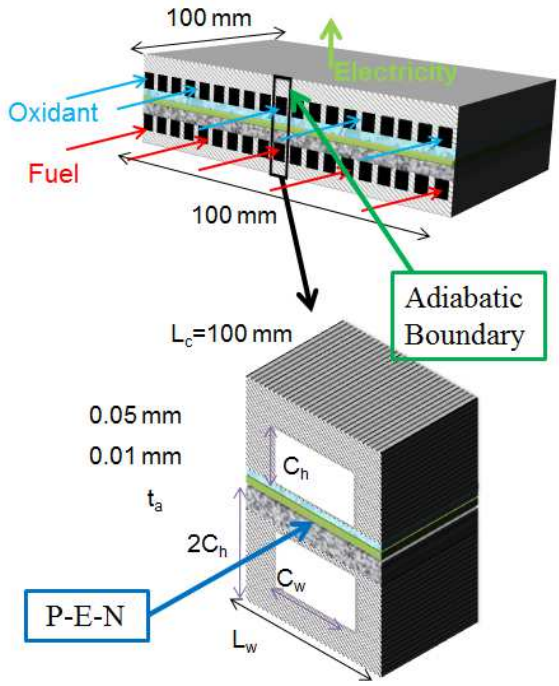

Figure 1.2. Schematics of an anode supported planar SOFC and a "unit cell." A unit cell is a pair of gas channels, interconnect, and P-E-N layers. (not to scale)

Material degradation of the brittle SOFC composite material is a key cause of poor performance and reliability. It has been reported by Atkinson [1] that high temperatures, thermal gradients, and significant temperature differences have either caused the material fracture depicted in Figure 1.3 or exacerbated resident material imperfections from cell manufacturing. In Figure 1.3, (A) represents cracking that hinders transport of reactants. (B) is cracking in the electrode that propagates into the electrolyte which diminishes available

reaction sites. (C) is a crack and blister which further degrade available reaction sites. (D) is catastrophic failure wherein no electricity can be harvested. (E, H) are blisters that limit matriculations of ions and reactants. (F) is a blister at the triple phase boundary which degrade available reaction sites. (G) is delamination between the electrode and electrolyte which destroys available reaction sites and ionic transport.

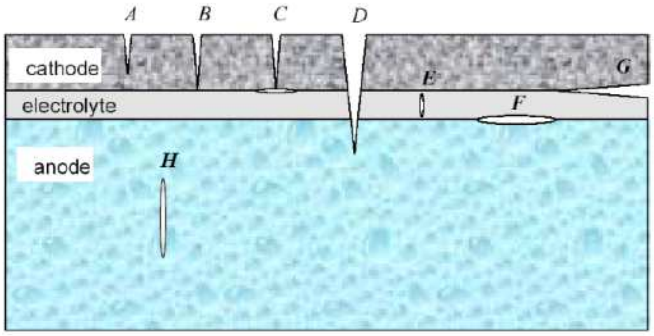

Figure 1.3. Diagram of the modes of material failure in an anode supported planar SOFC (not to scale). (Janine Johnson, GT MS Thesis 2004)

The fuel cell community has addressed the thermal gradient issue via insulation of the stack to mitigate cold spots and non-uniform heating (which leads to temperature gradients), conservative operation (*i.e.,* allowing the cell 8 hours to reach operating temperature), materials selection with matching coefficients of thermal expansion, cell geometry designs (*i.e.,* tubular, flat tube, etc.), and simulation to gain insights. Despite these efforts, current designs still experience adverse temperature gradients that can lead to potential failure or reliability issues in SOFCs.

Despite knowledge of the significance of heat transfer issues in SOFCs, little work has been done to characterize the correlation between heat transfer and cell reliability. Recently, the work of Nakajo [2] included a Weibull analysis detailing the probability of material failure of a SOFC as a function of temperature difference (inlet versus outlet of cathode) and

temperature gradient. A cell was deemed reliable if the probability of failure is less than 10^{-5}. According to Nakajo [2], as shown in Figure 1.4, this occurs when the cell temperature difference is approximately less than 100K and the temperature gradient is approximately less than 1000K/m. Despite these findings, there is not sufficient information in the fuel cell community concerning the range of temperature gradients and its impact on cell reliability and performance. In view of this fact, there is a need for more research that correlates the temperature gradients to the performance of planar SOFCs.

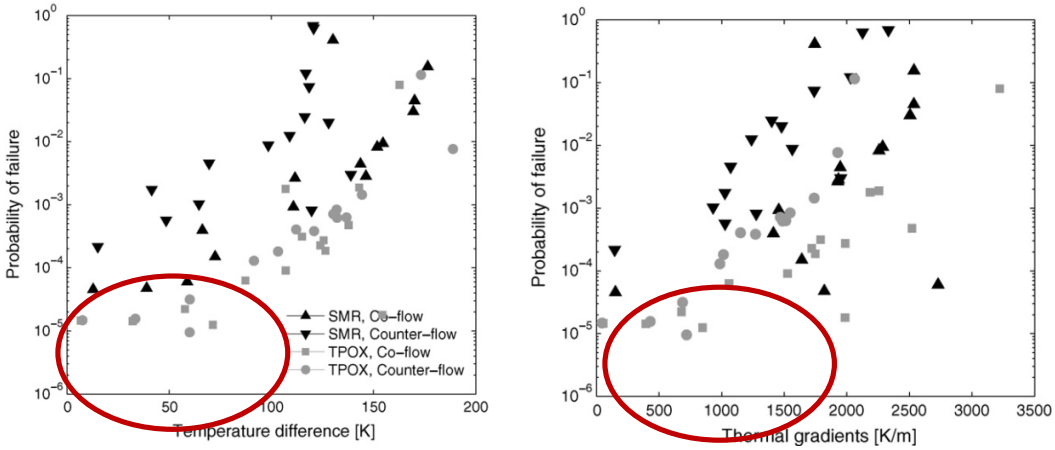

Figure 1.4. Probability of failure as a function of temperature difference and gradient [2].

Developing prototypes of SOFCs are quite expensive (*i.e.,* millions of dollars). As result, fuel cell designers rely on modeling and simulation tools to predict the impact of a range of parametric inputs on the response of SOFC systems. Modeling and simulating a SOFC is difficult due to the highly coupled nature of the physical phenomena within SOFCs. Table 1.2 depicts this complex coupling of the physical phenomena in a SOFC. Given this difficulty, numerous groups have sought to characterize the performance of a SOFC in various manners [3-22]. These performance models may be categorized as either steady-state or dynamic. Within these

categories, the performance models may be separated by spatial consideration (*i.e.* 0-D, 1-D, 2-D, or 3-D), the P-E-N (positive electrode-electrolyte-negative electrode) geometry, P-E-N material, and modeling approach (*i.e.,* finite element, finite volume, object based, etc.). While these modeling approaches allow for insight into the overall performance of a SOFC, they limit the accuracy of the results and the ability to develop effective designs. With continued improvements in computational power, higher fidelity modeling approaches can be used to develop effective SOFC designs. For the current work, a 1-D, distributed, and transient fuel cell model was developed in Matlab-Simulink™. Details of the model are presented in Chapter 5.

Table 1.2. Coupling of the physical phenomena in SOFC modeling.

Physical Phenomenon	Coupling Phenomena
Fluid transport	Heat transfer, mass transfer
Mass transfer	Fluid transport, Ionic transport
Ionic transport	Mass transfer, Heat transfer
Electrochemistry	Fluid transport, Heat transfer, Ionic transport
Heat transfer	Fluid transport, Ionic transport

1.2 Hypothesis

In view of the posed problem, the dissertation aims to offer a design approach that includes a more accurate assessment of SOFC performance and consideration for thermal gradients. In light of this, the central research question is: **"Can the architecture of a planar SOFC be computationally modified to optimally balance performance and thermal gradients?"** The current work aims to answer this question using a thermodynamic optimization that employs the entropy generation minimization (EGM) methodology. The present dissertation utilizes the Second Law of Thermodynamics metric of exergetic efficiency as the performance metric. The architecture is modified through four dimensionless geometric

parameters that relate the internal dimensions of the P-E-N thicknesses and gas channel dimensions (Figure 1.2), and the external dimensions of the cell width and interconnect height. Internal Aspect Ratio (IAR), Dimensionless Gas Channel Width (DGCW), Slenderness Ratio (SR), and Electrode-to-Electrolyte Ratio (EER) are the four dimensionless geometric parameters. The significance of each dimensionless geometric parameter and relevance to physical phenomena are detailed in Chapter 3. Two of four dimensionless parameters are optimized based upon a constrained thermodynamic optimization problem.

1.3 The Novelty and Importance of the Research

The novelty of the proposed research lies in the application of thermodynamic optimization. The proposed research will be the first reported usage of entropy generation method (EGM) to address both performance and thermal gradients in SOFCs. In traditional thermodynamic optimization, only performance parameters such as efficiency or power density are focused upon as detailed by Bejan [23]. However, Bejan noted that the design that has the minimum entropy production (*i.e.,* maximum exergetic efficiency) is not necessarily equivalent to the design that wrought maximum power density. Certain ideal scenarios such as having an infinite thermal reservoir is needed to approach such a scenario. Furthermore, Haynes and Wepfer [24] also noted that utilizing 1st law metrics such as fuel cell efficiency are limited and that exergetic efficiency is a more accurate assessment of performance. More details about previous work done in the field of thermodynamic optimization, as well as geometric design optimization, are given in Chapter 2. The proposed solution of thermodynamic optimization is novel in that both performance metrics and thermal gradients are considered. In applying thermodynamic optimization to a planar SOFC, this is understood to be the first reported

consideration of both a performance metric and thermal gradients in a thermodynamic optimization. This methodology offers a new design approach to energy systems. This new thermodynamic design methodology offers a solution to a key issue plaguing SOFCs.

1.4 Overview of Solution

One constrained thermodynamic optimization problem is solved in order to optimally balance power density and thermal gradients. The optimization is done through parametrically changing the four dimensionless parameters IAR, SR, DGCW, and EER. Assuming a 100 mm by 100 mm footprint, the cell dimensions are calculated. Table 1.3 summarizes the range of the four dimensionless parameters used for the parametric optimization and the assumed baseline values. Details of the constrained thermodynamic optimization problem are detailed in Chapter 3.

Table 1.3. Dimensionless parameters, baseline values, and respective ranges.

Ratio	Baseline	Range
Interconnect Aspect Ratio (IAR=C_w / C_h)	0.1	0.2 ≤ IAR≤5
Electrode/Electrolyte Ratio (EER=t_a / t_e)	50	10 ≤ EER≤100
Slenderness Ratio (SR =L_c /L_w)	24	5≤ SR≤100
Dimensionless Gas Channel Width (DGCW=C_w/L_w)	0.25	0.1≤ DGCW≤0.9

Prior to conducting the parametric optimization, an investigation was conducted to note the impact of each dimensionless parameter on performance and fine tune the range of values used in the optimization. Those results are included in the Methodology chapter. Following the Methodology chapter is a chapter that describes the 1D fuel cell model used in the dissertation.

Then, in Chapter 5, the optimization results are presented and discussed. Finally, Chapters 6 and 7 are devoted to highlighting conclusions and future work, respectively.

2 LITERATURE REVIEW

2.1 Issue of High Temperature Operation of SOFCs and Overview of Literature Review

The issue of designing a reliable solid oxide fuel cell (SOFC) due to high temperature operation has been previously detailed in the literature by Nakajo, Recknagle, and Yakabe [2, 25, 26]. Nakajo showed computationally how temperature gradients relate to the probability of failure for various fuel processing and operational scenarios. For the chosen design, the probability of failure decreased as thermal gradients decrease. Failure could occur during the final step of manufacturing when the cell cools, steady-state operation, and during transient episodes. As noted by Nakajo, for steady state applications, SOFCs need a probability of failure to be 10^{-5} or better. Nakajo reported temperature gradients below 1000 K/m and temperature differences below 100K for the chosen design had a probability of failure of 10^{-5} which is highlighted in Figure 2.1. Recknagle, like Nakajo, detailed the various mechanisms and scenarios by which SOFC see adverse internal thermal stresses. Both Recknagle and Yakabe note that addressing non uniform temperature fields and adverse thermal gradients are key steps in designing a reliable SOFC. Design solutions to addressing non uniform temperature fields and adverse thermal gradients have included thermodynamic optimization studies, SOFC architectural design studies, and operational strategies. The first two subjects will be covered in the following literature review. The literature review proceeds in the following manner. First, a review of thermodynamic optimization approaches will be presented. Second, a literature survey of SOFC architectural design studies will be reviewed. Lastly, a brief synopsis of how the present dissertation is distinguished from the current literature is presented.

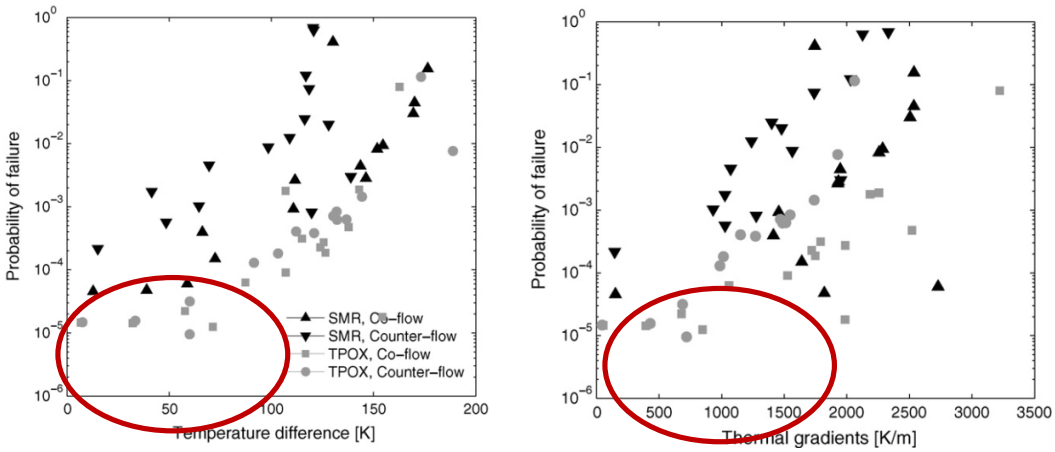

Figure 2.1. Probability of failure as a function of temperature difference and gradient [2].

2.2 Thermodynamic Optimization Approaches

The field of thermodynamic optimization has been pioneered by Adrian Bejan. Thermodynamic optimization approaches traditionally seek to minimize losses thereby maximizing power output and/or efficiency. The two prevalent thermodynamic optimizations developed by Bejan are entropy generation minimization (EGM) and constructal theory (CT). EGM and CT are discussed herein.

In a non-equilibrium energy system with flow configuration there exist a few approaches to thermodynamically optimize the system. In EGM, all sources are entropy generation (*i.e.,* heat, mass, and fluid flow, etc) are identified, tabulated, and minimized. Typically, energy systems have competing irreversibilities such as the entropy generated by heat and fluid flow (e.g., turbulent flow may improve heat transfer, but generate more fluid frictional entropy generation occurs). However, there exists some minimum entropy generation

whereby the maximum power potential can be produced along with improved thermodynamic efficiency. In conducting EGM, once all sources of entropy generation are identified and tabulated, an optimization strategy may be employed. The optimization proceeds by minimizing the gross entropy generation by varying geometric or operational parameters. This method is limited in that there is no consideration of thermal gradients.

Constructal theory is derived from observation of evolving structures in nature such as tree branches, and air passages in human lungs. Constructal theory extends EGM via the constructal law which states, "For a finite-size flow system to persist in time (to survive) its configuration must evolve in such a way that it provides easier currents that flow through it [23]." Constructal theory varies geometric parameters related to flow configuration in order to optimize performance. Like EGM, constructal theory does not consider thermal gradients.

2.2.1 Thermodynamic Optimization Applied to SOFCs.

Thermodynamic optimization has been applied to a number of engineering problems and in other disciplines such as city planning and biology [23]. For the dissertation, a review of how thermodynamic optimization has been applied to SOFC design is needed. To date, there have been a few papers by Sciacovelli [27-29] that apply EGM to a SOFC and one paper by Ordonez *et al* [30] to apply constructal theory to a SOFC. Sciacovelli optimized the architecture of a monolithic tubular SOFC via EGM. Sciacovelli [27] modeled a single channel of a monolithic cell shown in Figure 2.2 with a high fidelity CFD model (Fluent^{TM}) and simulated a stack with a thermal model. Utilizing the EGM method, Sciacovelli reduced the total entropy production by 50% which resulted in a power density increase of 10%. Sciacovelli did not include activation

losses in the EGM analysis, though it was considered in the calculation of cell potential. While these results are promising, no optimization included any constraint of thermal gradients.

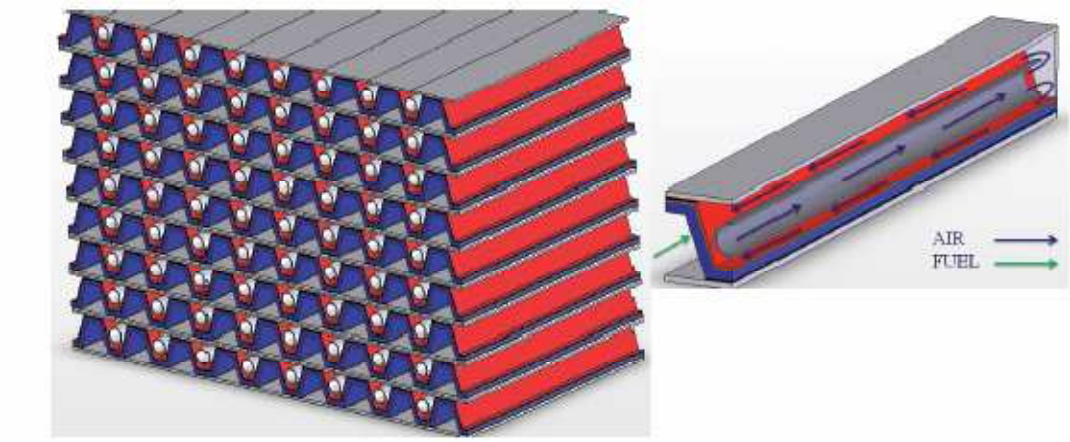

Figure 2.2. Schematic of monolithic tubular SOFC stack and one single channel [27].

Ordonez *et al* [30] utilized a control volume approach to simulate thermal and electrochemical interactions which is depicted in Figure 2.3. There were only six control volumes and therefore spatial effects are not accurately modeled. Ordonez et al report the need for more accurate temperature predictions as the power density error could reach 30%. Two key points of emphasis for the proposed work are the use of the more accurate modeling approach and the inclusion of temperature gradient as a constraint. Nonetheless, Ordonez *et al* report cases for when an optimized flow structure produced maximum power density. While contructal theory may be used to optimize flow structures, it does not account for the impact of thermal gradients.

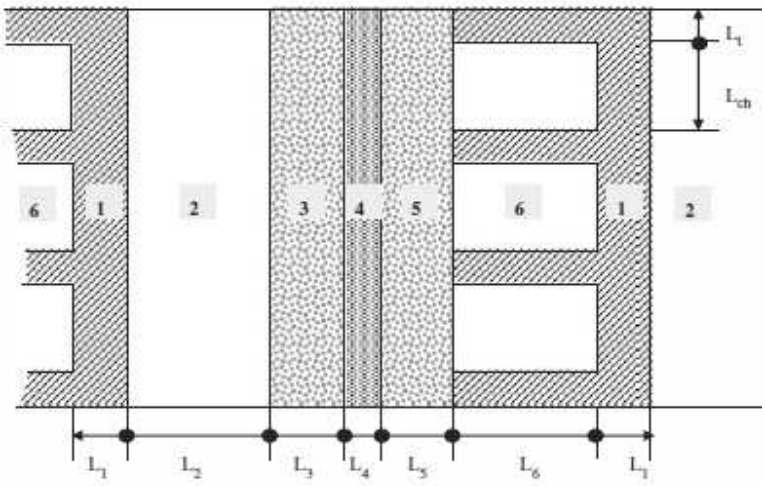

Figure 2.3. Schematic of the six control volumes employed by Ordonez *et al* [30] to simulate the electrochemical and thermal interactions in a SOFC.

2.2.2 Exergy Analysis Applied to SOFCs.

Exergy analysis of solid oxide fuel cells has primarily been done in conjunction with system analyses. The selected work [31-50] span the gamut of research done on exergy analysis of SOFC systems and SOFC unit cells or stacks. A detailed discussion of system exergy analysis of SOFCs is beyond scope of the present dissertation. However, the noted system analysis papers are noted for reference. It should be also noted that the system analysis papers do highlight the fact that SOFCs have considerable exergy destruction relative to the entire system (e.g. Dincer [38] and Hotz [44] showed the SOFC contributes between 37% and 52% of total availability destruction). Therefore, analysis of exergy destruction in a SOFC is pertinent and necessary. Given this, the papers of primary interest [35, 43, 46, 50] on exergy analysis of SOFCs are reviewed as well as their contribution to the body of knowledge relative to SOFC characterization, operation, or design.

Haynes and Wepfer [43] conducted a second law analysis of a commercial grade tubular SOFC noting the impact of operating parameters on exergetic efficiency. Utilizing a validated 1D

model, it was concluded that as fuel utilization increases there is a slight decrease in second law efficiency which is highlighted in Figure 2.4. Whereas, air stoichiometric number and operating voltage both increased second law efficiency as their values increased. Air stoichiometric numbers beyond 4 did not improve second law efficiency as shown in Figure 2.5. Exergetic efficiency linearly increased as operating voltage increased as shown in Figure 2.6. Second law efficiencies ranged between 75% and 90%. Furthermore, irreversibilities were quantified, compared, and the impact of operating parameters were noted. Electrochemical irreversibilities increase slightly as air stoichiometric number increased as highlighted in Figure 2.7. Thermal irreversibilities due to sensible heating decreases as air stoichiometric number increased. Irreversibilities from power conditioning were not impacted by varying air stoichiometric number. As shown in Figure 2.8, exergetic efficiency decreases as operating pressure increases. Although Haynes and Wepfer added insight to the importance of second law analysis in SOFC operation and characterization, there was no consideration of the impact of geometric parameters or architectural design optimization.

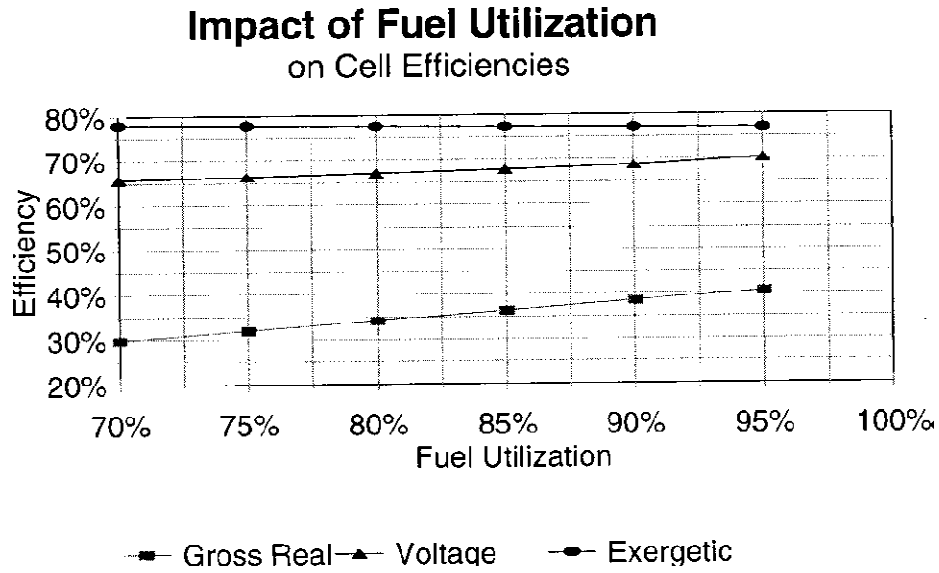

Figure 2.4. The influence of fuel utilization on cell efficiencies. Haynes and Wepfer [43].

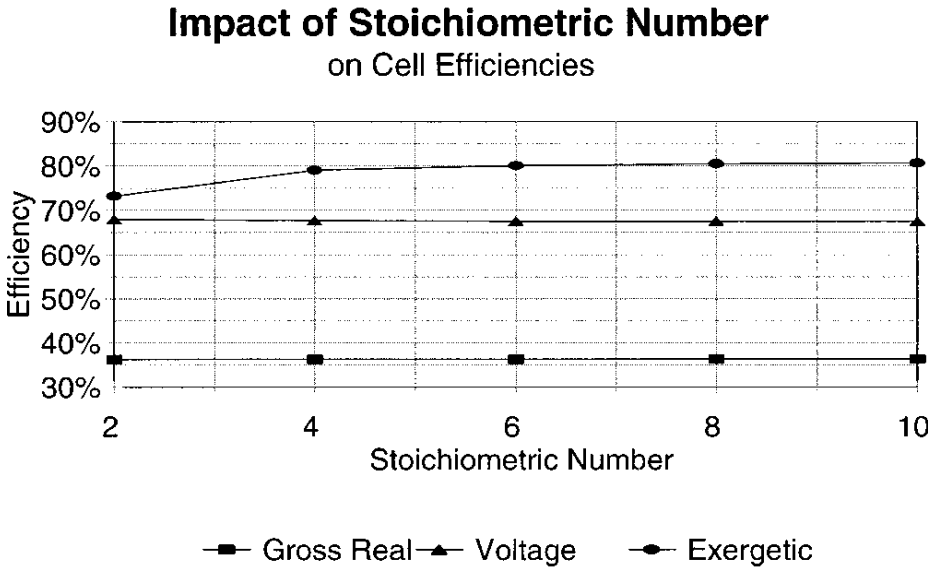

Figure 2.5. The impact of stoichiometric number on cell efficiencies. Haynes and Wepfer [43].

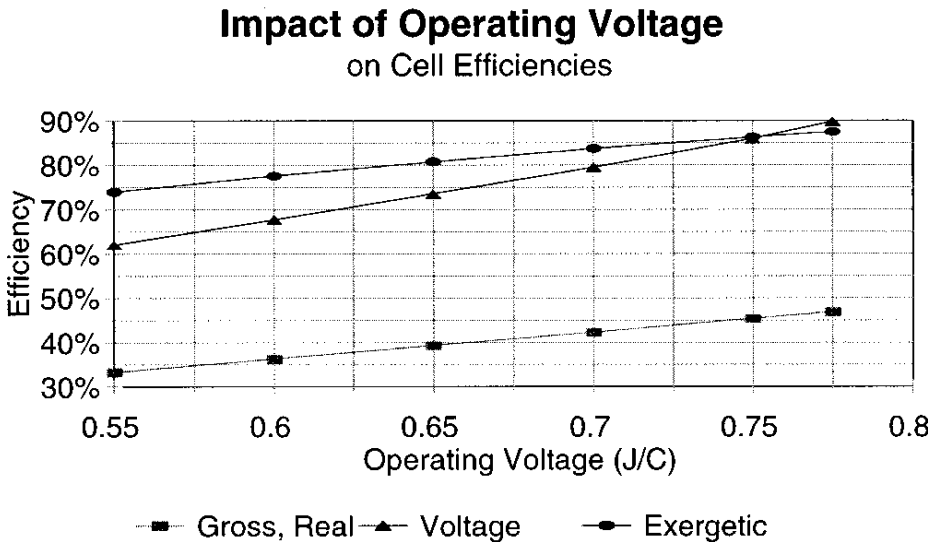

Figure 2.6. The impact of operating voltage on cell efficiencies. Haynes and Wepfer [43]

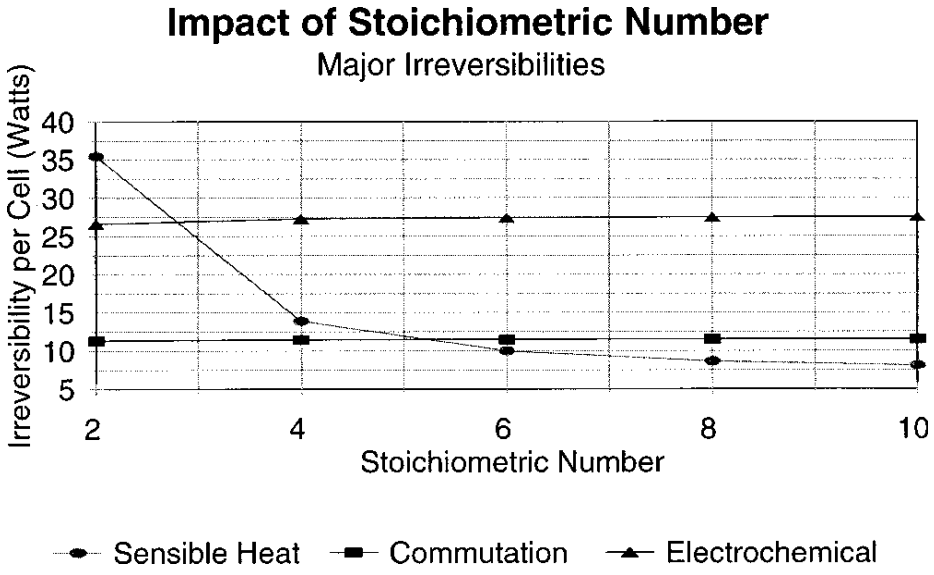

Figure 2.7. The impact of air stoichiometric number on irreversibilities. Haynes and Wepfer [43].

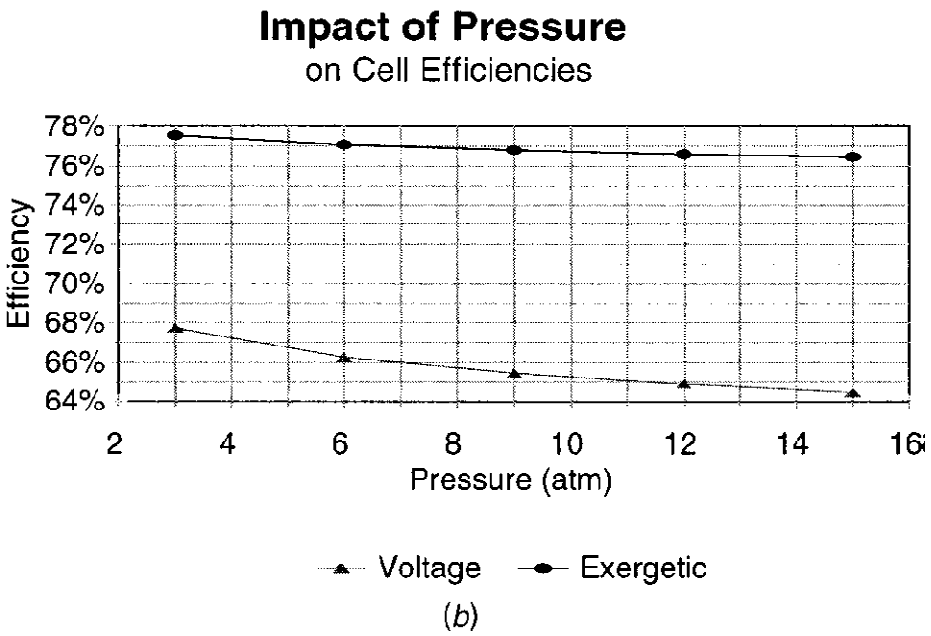

Figure 2.8. The influence of pressure on voltage and exergetic efficiencies shown by Haynes and Wepfer [43].

Calise *et al* [35]conducted an extensive geometric and exergy analysis of a tubular SOFC utilizing a 1D finite volume model. A sensitivity study of how cell diameter and cell length affect exergetic efficiency was conducted. As cell diameter increased exergetic efficiency increased as highlighted in Figure 2.9. Also shown in Figure 2.9 is the impact that cell diameter has on temperature profiles. As cell diameter increased, temperature increased. Electrical efficiency and fuel utilization also increased with cell diameter. In analyzing the impact of cell length, it was shown that as cell length increased exergetic efficiency increased as shown in Figure 2.10. Exergetic efficiency ranged from 77% to 93%. Also, fuel utilization and cell temperature increased with cell length. Also of note in both Figures 2.9 and 2.10 is the reporting of spatial distribution of exergetic efficiency. Lastly, cell voltage was analyzed. As cell voltage increased, exergetic efficiency increased. Though Calise *et al* examined geometric effects on second law

efficiency, there was no analysis of the sources of exergy destruction, nor was there analysis of P-E-N geometry.

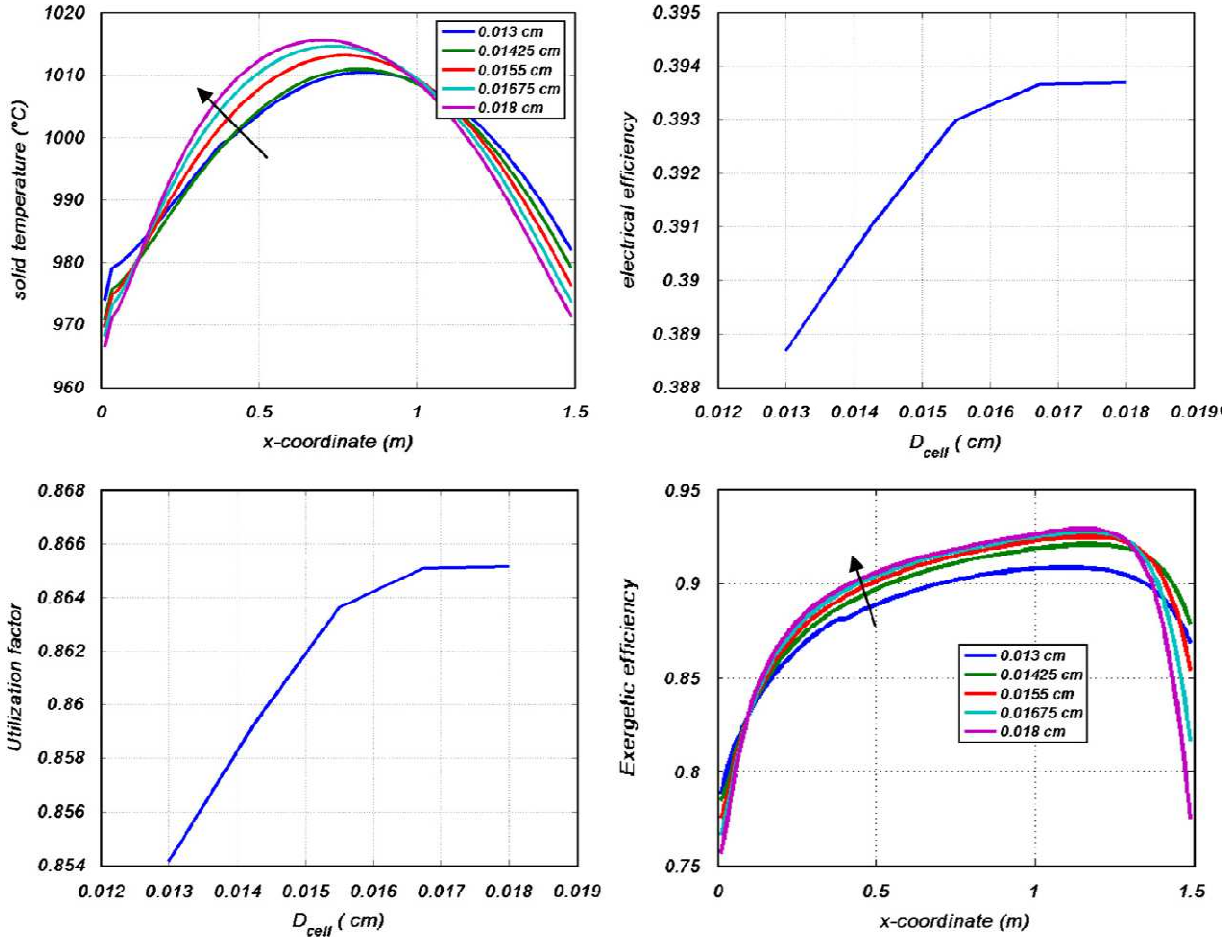

Figure 2.9. The impact of cell diameter on exergetic efficiency, exergy destruction, and performance shown by Calise *et al* [35].

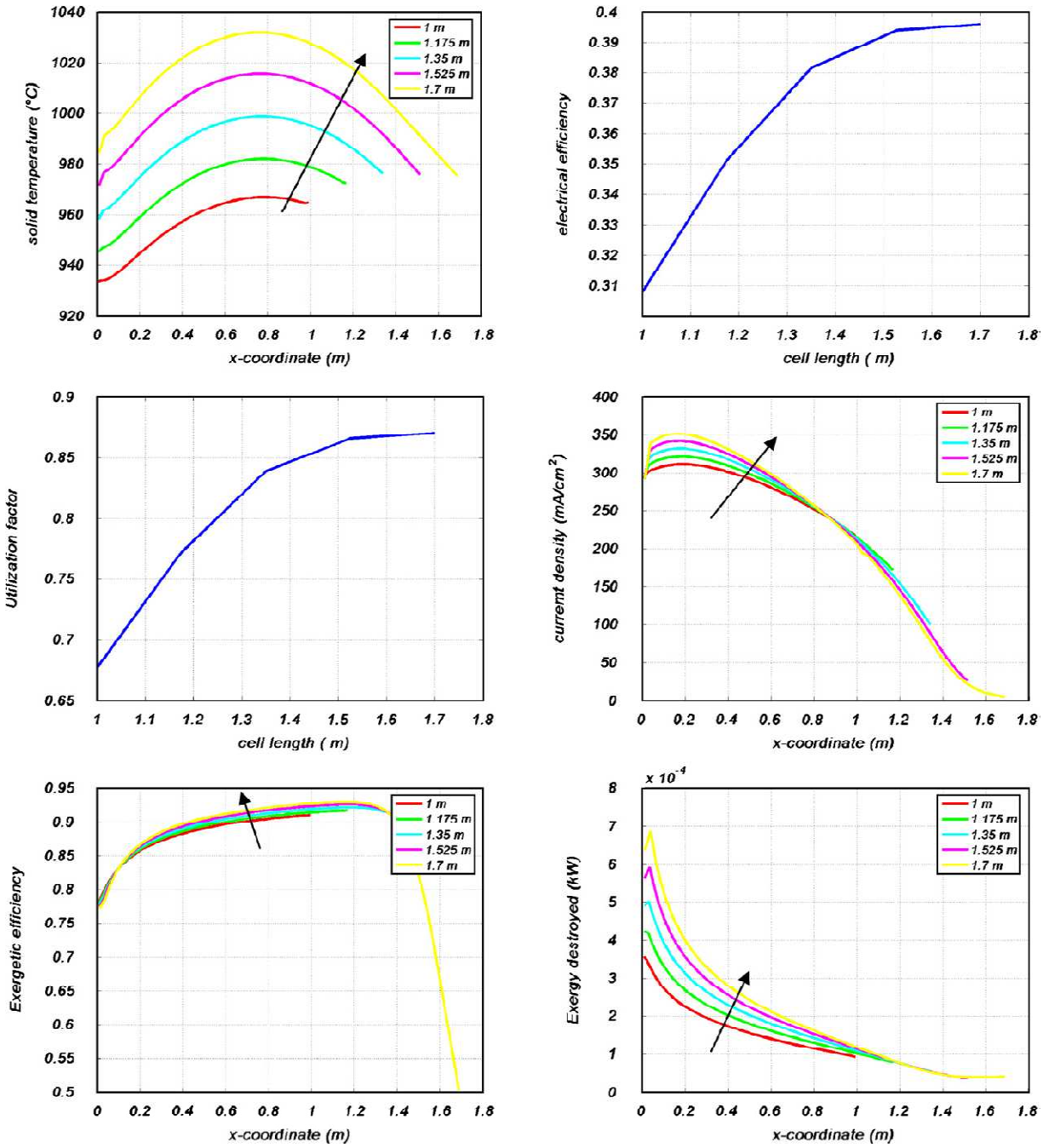

Figure 2.10. The influence of cell length on exergy efficiency, exergy destroyed, and performance shown by Calise et al [35].

Odukoya *et al* [46] analyzed a planar cationic SOFC-H^+ (ammonia fed). Of note in Odukoya's work was the connection between fuel utilization and current density on second law efficiencies. As fuel utilization and current density increased, exergetic efficiencies increased.

Fuel utilization was varied between 0.6 and 0.8. Current density was varied between 600 A/m^2 and 1500 A/m^2. These results differ from planar anionic SOFCs in which higher fuel utilization marginally decreases exergetic efficiency and lower current density (*i.e.,* higher operating voltage) causes significant increases in exergetic efficiency. The results of the exergy analysis aided the authors in improving the system design in which the fuel cell was used. The relevance of Odukoya's work to present dissertation is the importance of second law analysis in making design decisions. In this instance, exergy analysis was used to improve system performance. For the present dissertation, exergy analysis via thermodynamic optimization is used to improve the operation of SOFCs.

Most recently, Wongchanapai *et al* [50] conducted a second law analysis of a direct internal reforming planar SOFC utilizing a 1D model. Wongchanapai *et al* characterized effect of flow configuration (co-flow versus counter-flow), current density, and anode thickness on exergetic efficiency and thermal gradients. It was found that the counter-flow arrangement had higher exergetic efficiencies than the co-flow configuration. Despite this, counter-flow arrangement had significantly higher thermal gradients than the co-flow flow design. Further exacerbating the thermal gradients was the heat transfer effects due to direct internal reformation of the fuel. Thermal gradients as high as 5170 °C/m and 3240 °C/m, respectively, were reported for counter-flow and co-flow arrangements. It was found that thicker anodes significantly reduced thermal gradients to 3390 °C/m and 1990 °C/m, respectively, for counter-flow and co-flow arrangements. Note that the authors used ceramic interconnects in their work as opposed to metallic interconnects modeled in the present dissertation. Though the authors

noted the effect of anode thickness on thermal gradients, no other geometric parameters were analyzed nor was each source of exergy destruction characterized.

2.3 SOFC Architectural Design Studies

The SOFC design community has examined the various components of the SOFC architecture to improve performance. The following review is segmented into two categories: design studies of the interconnect component and the P-E-N structure. Recently, there have been studies by Liu *et al.* and Nelson *et al.* [51-53] to optimize the rib thickness of the interconnect component for maximum electrical performance, and other studies by Lin *et al* and Selimovic *et al.* [54, 55] which have demonstrated the importance of heat transfer to and from the P-E-N.

2.3.1 Interconnect Design Studies

To date, the modeling community has primarily focused upon fluid flow, electronic transport, and mechanical stability as it pertains to interconnect design. Various modeling techniques ranging from high fidelity finite element models to simpler finite volume approaches have been utilized in order to optimize the interconnect. Currently, the literature search has not discovered research efforts on the thermal effects of interconnect design in terms of minimizing temperature gradients.

Liu *et al*. [51, 53] parametrically determined that the optimal rib thickness is a linear function of pitch (*i.e.,* rib thickness plus gas channel width) via a finite element COMSOL model (two-dimensional and three-dimensional). Parallel and perpendicular flow arrangements were considered. Liu's work showed that the optimal rib thickness linear relationship was similar for both parallel and perpendicular flow configurations. While a sensitivity analysis showed that

optimal interconnect design is independent of electrode porosity, layer thickness, and conductivity, there was no thermal analysis conducted. Given the temperature dependence of conductivity and overpotentials, a heat transfer analysis must be conducted to verify those results. Furthermore, the optimization goal was to maximize power density without consideration of temperature gradients. Nonetheless, Liu et al demonstrated that manipulation of the interconnect architecture can improve the power density of a SOFC.

Nelson and Haynes [52] included the effects of interconnect constriction resistance on mass transport through the porous electrodes. As shown in Figure 2.11, both mass and electronic path lengths are impacted by the geometry of the interconnect. Nelson showed that smaller unit cell widths result in lower ohmic resistances and higher fuel depletion current densities. Though Nelson showed improved cell performance through modifying the interconnect geometry, thermal considerations were not accounted for.

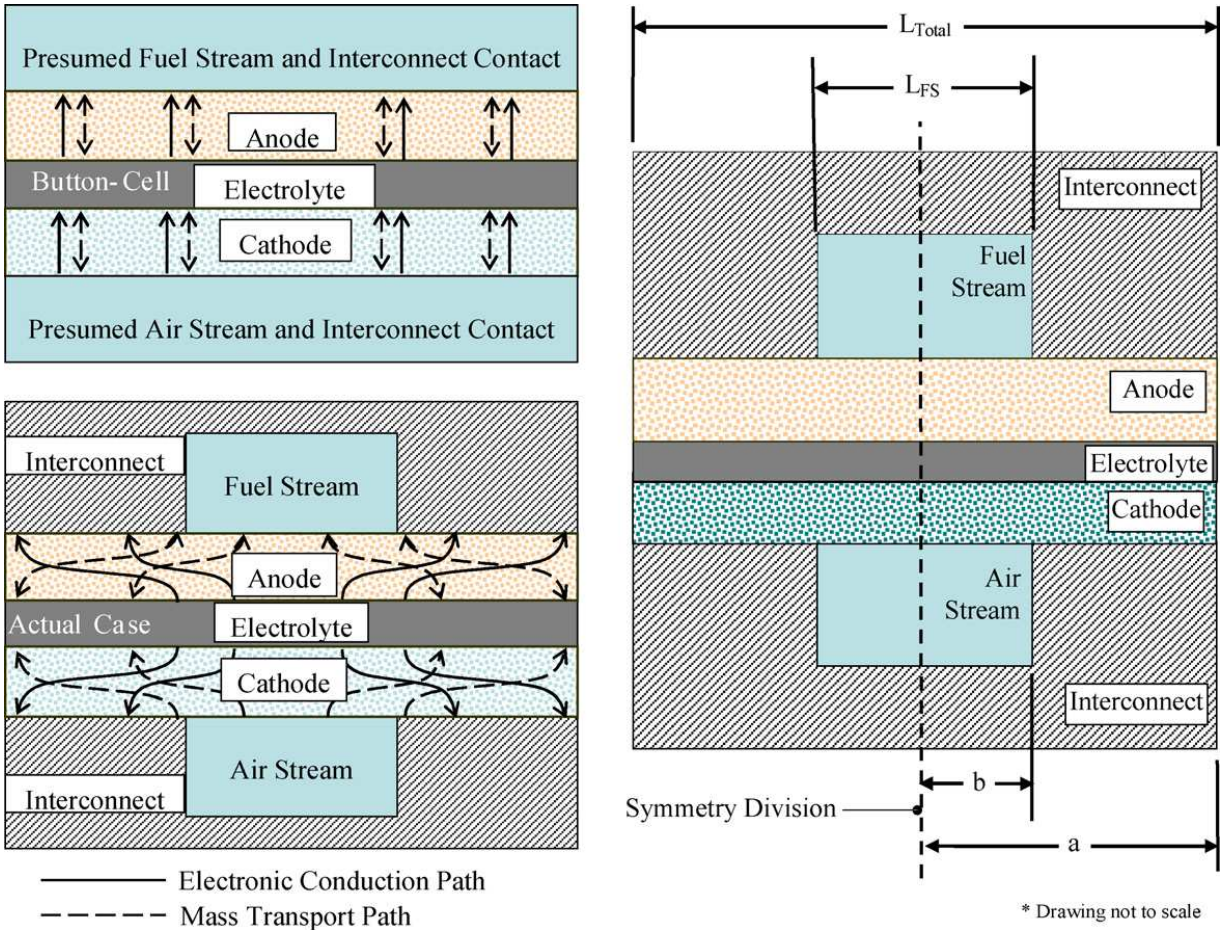

Figure 2.11. Diagram detailing impact of interconnect geometry on mass and electronic transport in comparison to traditional button cell presumptions.

Lin et al. [55] demonstrated via finite element analysis that the thermal expansion behavior of the interconnect plays a vital role in the thermal stress distribution in the P-E-N. It was determined that the interconnect alone is insufficient in providing mechanical support. The seals provide the remaining structural support. Traditionally, the interconnect component is designed to be the thickest component of a planar SOFC. This allows for good electrical conduction and provides (in theory) mechanical support to the brittle P-E-N materials. It can be inferred from Lin's group that the design of an interconnect should minimally consider

structural support if other performance parameters might be improved (e.g., minimal thermal gradients).

Selimoivic [54] compared cross flow, co-flow, and counter-flow configurations of metallic and ceramic interconnects. It was shown that a metallic interconnect would induce more uniform temperature fields through the P-E-N thereby reducing maximum principal thermal stresses by at least 50%. Selimoivic concluded that metallic interconnects can better accommodate different flow configurations due to their relatively high thermal conductivity. From this result, one can infer that a metallic interconnect may be optimally designed for minimal temperature gradients without sacrificing the structural integrity of the stack. Hence, the solutions from literature promote the possibility of optimal cell performance and thermal gradients via optimization of a cell architecture (e.g. the metallic interconnect).

2.3.2 P-E-N Design Studies

In designing the cathode (*positive* electrode)-electrolyte-anode (*negative* electrode) (P-E-N), there has been extensive work in studying the different materials, functionally graded layers within both electrodes, effect of electrode thickness, and overall design of the P-E-N as detailed in the literature [56-85]. While these areas are vital to designing better performing SOFCs, the primary concern relevant to the present dissertation is the relative thicknesses of the anode relative to the electrolyte and its impact on performance as highlighted in the literature [57, 67, 69, 82]. Given that the anode supported design is the current state-of-the-art in SOFC design and the chosen SOFC design of focus, there is a need to understand what previous researchers have done to note the performance ramifications of varying anode thickness.

Chan[57] conducted a sensitivity study by varying the thickness of all three P-E-N layers between 50 micrometers and 750 micrometers. It was shown that the anode is best suited as the structural support component relative to the electrolyte and cathode. Cell voltage is most sensitive to changes in the thicknesses of the electrolyte followed by the cathode. Wang *et al* [69] further showed the how concentration polarizations are impacted by varying anode thickness and porosity as shown in Figure 2.12. Anode thickness was varied between 0.25mm and 1.0mm. It was shown that smaller anode thicknesses and larger anode porosities will decrease concentration losses. Kuo *et al* [82] also showed the impact of anode thickness and porosity on cell performance as shown in Figure 2.13. Anode thickness caused slight changes to the polarization curve while anode porosity impacted performance by less than 25 mW/cm^2 or 10%. While the aforementioned authors focused on electrical performance based upon anode thickness, Magar *et al* [67] demonstrated the impact anode thickness has upon temperature profiles. Figure 2.14 shows that thicker anodes reduce temperature profiles.

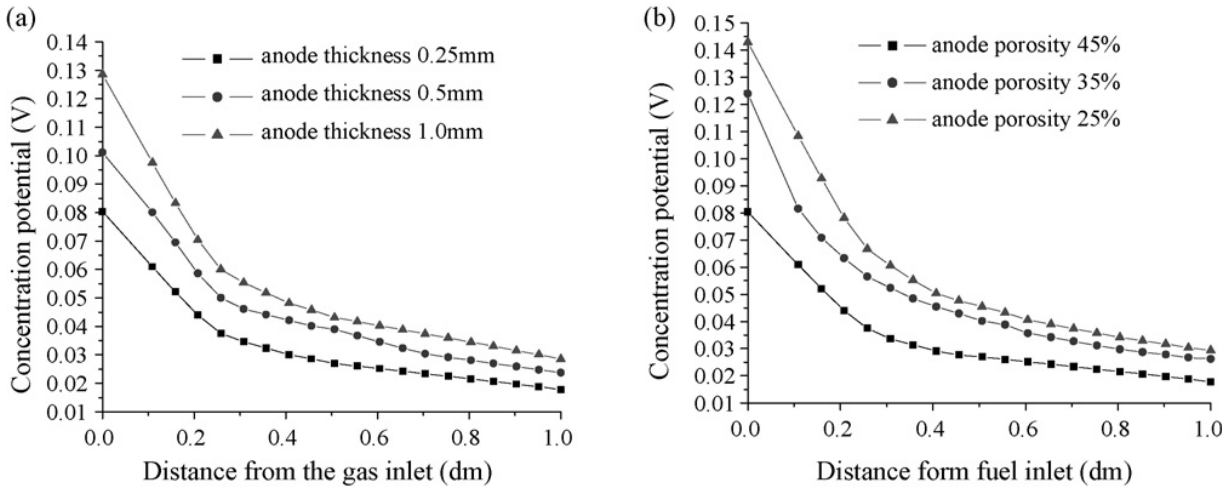

Figure 2.12. Wang et al [69] showing the effect of anode thickness and porosity on concentration losses.

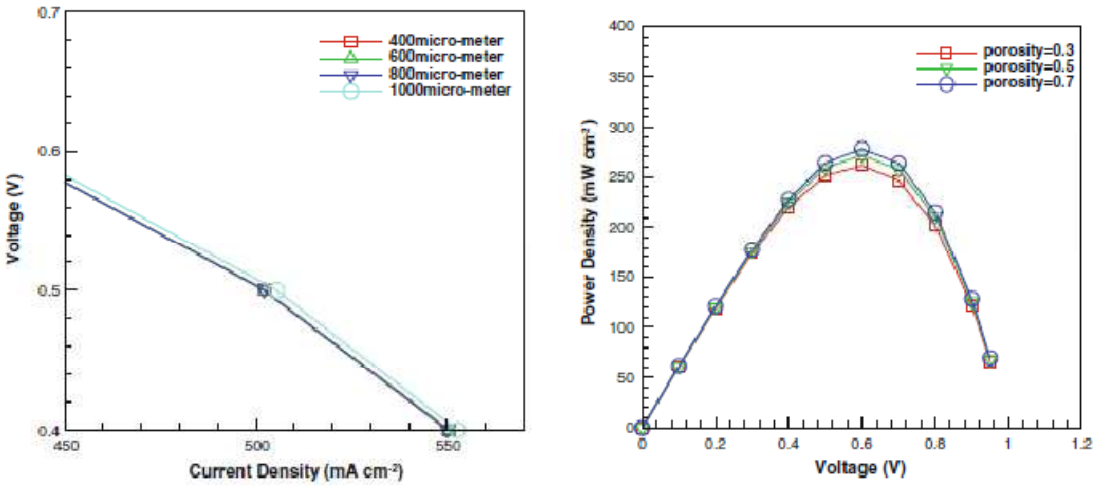

Figure 2.13. Kuo *et al* [82] showing the effect of anode thickness on cell polarization curve.

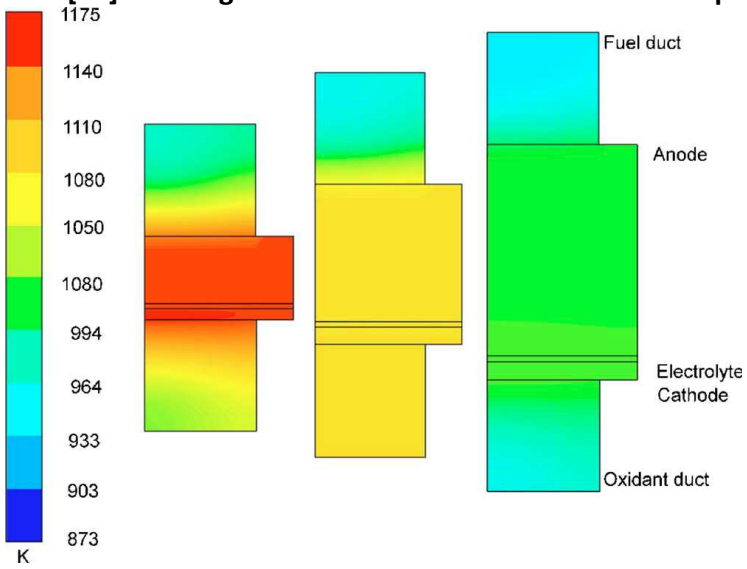

Figure 2.14. Magar *et al* [67] showing the impact of anode thickness on temperature profiles.

2.4 The Distinction of the Present Dissertation from the Literature

The present dissertation aims to fill in the gap in the body of knowledge pertaining to the design and thermodynamic optimization of SOFCs through offering dimensionless geometric design parameters, introducing a novel design approach through thermodynamic optimization, quantifying sources of exergy destruction, and noting the impact of geometry on sources of entropy generation. The literature does not consider thermal gradients in second law

analyses of SOFCs, nor identifies one. The present dissertation aims at connecting the issue of thermal gradients to second law analysis in such a way to optimize design without adverse thermal gradients. Though the present literature has conducted second law analysis of SOFCs and investigated geometric influences on performance, there has not been a comprehensive and specific second law analysis to optimize the architecture of a SOFC to optimally balance performance and reliability. The present dissertation does this through introducing dimensionless geometric parameters and a modified thermodynamic optimization approach.

3 THERMODYNAMIC OPTIMIZATION METHODOLOGY

The dissertation employs a thermodynamic optimization approach which uses a high fidelity 1D model of a SOFC. In order to perform a thermodynamic optimization, the thermodynamic equations must be derived and the optimization problem must be well posed. In conducting a thermodynamic analysis, it is necessary to define the control volume of the system. The control volume for the analysis of a planar SOFC is depicted in Figure 3.1. The control volume is the "unit cell" as defined as the P-E-N, half interconnects, and pair of gas channels. As discussed in the literature review chapter, Bejan developed the thermodynamic optimization methodology of entropy generation minimization (EGM) [23]. Per the equations for the thermodynamic analysis, the entropy generation equations for a solid oxide fuel cell are derived based upon Bejan's EGM work. These equations are recast in the following subsection. Per the optimization problem, the objective is to reduce total entropy generation through maximizing exergetic efficiency while constraining maximum thermal gradients. The purpose of this objective is to employ a better metric of performance than traditional metrics utilized. Exergetic efficiency captures available work done through electrical and thermal output. Given that SOFCs can be used to produce electricity and high quality heat, exergetic efficiency is a more accurate measure of performance. The optimization problem is explicitly detailed in the next subsection. Prior to conducting an optimization, a performance analysis of the dimensionless geometric parameters was conducted. The results of the performance analysis were used to bind the range and resolution of the dimensionless geometric parameters. Given the flexibility of the 1D fuel cell model to simulate a wide range of geometric parameters and speeds of computation, a parametric optimization was conducted to solve the optimization

problem. Further details are given in the subsequent subsection. Note that details of the 1D fuel cell model are given in Chapter 4.

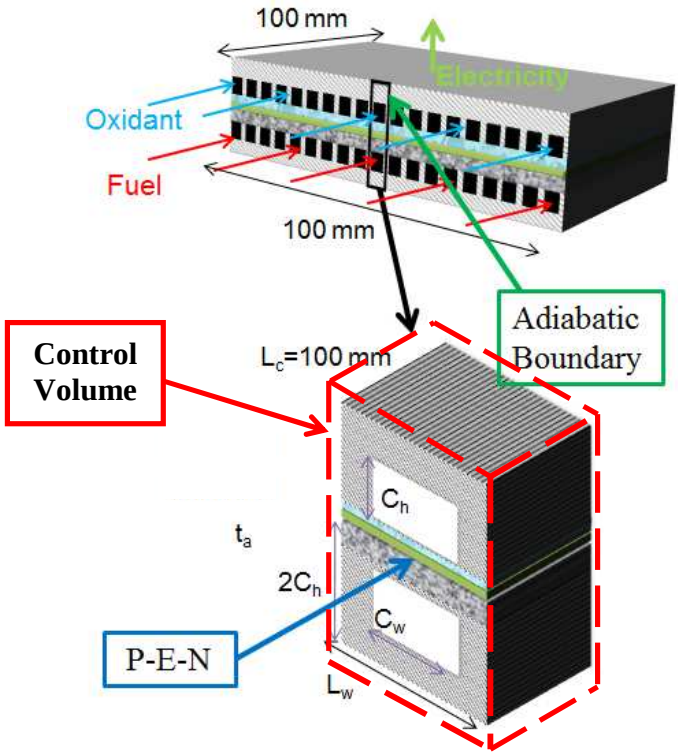

Figure 3.1. SOFC control volume for thermodynamic analysis. (not to scale)

3.1 Description of Optimization Problem

3.1.1 Modified Entropy Generation Equations

Sciacovelli [86] recently derived the entropy generation equations for a SOFC as guided by Bejan's EGM work. The entropy generation equations are recast and appropriately applied to the planar SOFC modeled in the dissertation. Equation 3.1 describes the entropy balance for an infinitesimal volume developed as a rate of change equation, where $\boldsymbol{\rho}$ is density (kg/m^3), s is specific entropy (W/(kg-K), $\boldsymbol{\sigma}$ is the entropy flux defined in Equation 3.2, and $g_{\boldsymbol{p}}$ is the rate of

total entropy generation per unit volume (W/(m^3-K)). The specific modes of entropy generation are presented in Equation 3.3 and are discussed after their presentation.

$$\rho \frac{ds}{dt} = -\nabla \cdot \sigma + g_p \tag{3.1}$$

$$\sigma = \frac{1}{\mathrm{T}}\left(\mathrm{J_q} + \sum_{\mathrm{i}} \mu_{\mathrm{i}} \mathrm{J_i}\right) \tag{3.2}$$

In Equation 3.2, T is temperature (K), $\boldsymbol{J_q}$ is heat flux (W/m^2), μ_i is chemical potential of species i, and $\boldsymbol{J_i}$ is diffusive flux of species i (kg/m^2/s).

$$g_p = g_{tf} + g_h + g_{ohm} + g_{act} + g_{conc} \tag{3.3(a.))}$$

$$g_{tf} = \frac{q_{conv} \cdot \Delta T_{sg}}{V_{slice} \cdot T_g^2 \left(1 + \Delta T_{sg}/T_g\right)} + \frac{\dot{m}}{\rho \cdot T_g} \frac{\Delta P}{V_{slice}} \tag{b.}$$

$$g_h = \frac{1}{T_s^2}\left(q_{cond} \cdot \frac{\Delta T_s}{\Delta x}\right) \frac{\mathbf{1}}{A_{,slice}} \tag{c.}$$

$$g_{ohm} = \frac{1}{T_s}\left(\eta_{ohm} \cdot i_{cv}\right) \frac{\mathbf{1}}{V_{slice}} \tag{d.}$$

$$g_{act} = \frac{1}{T_s}\left(\eta_{act} \cdot i_{cv}\right) \frac{\mathbf{1}}{V_{slice}} \tag{e.}$$

$$g_{conc} = \frac{1}{T_s}\left(\eta_{conc} \cdot i_{cv}\right) \frac{\mathbf{1}}{V_{slice}} \tag{f.}$$

In Equation 3.3, $\dot{m}$ is the mass flow rate of the oxidant, q_{conv} is the local convective heat transfer rate within a unit cell, ρ is density of the oxidant , c_p is the constant pressure specific heat of the oxidant,ΔT_{sg} is temperature difference between the solid and gas, V_{slice} is the volume of a section or "slice" of the descritized control volume, A_{slice} is the cross-sectional area of a section or "slice" of the descritized control volume, η_{ohm} is the ohmic overpotential, η_{act} is the activation overpotential, η_{conc} is the concentration overpotential, and i_{cv} is the current within the given volume (*i.e.,* A). As per the entropy generation terms, g_{tf} is the entropy generation due to thermal-fluidic losses in the gas channel, and g_h accounts for irreversibilities due to conduction heat transfer. Finally, g_{ohm} quantifies the ohmic

irreversibilities, g_{act} represents the activation irrversibilities, and g_{conc} represents the concentration losses.

Entropy is generated in a fuel cell through heat transfer across a finite temperature difference, fluid friction in the gas channel, charge and species transport resistance and through electrochemical reaction. Each mode of entropy generation detailed in Equation 3.3 is related to these fundamental modes of entropy generation. Derived by Bejan *et al* [87], Equation 3.3b is related to the entropy that is generated through convection heat transfer between the oxidant and solid volumes and through fluid friction induced by the oxidant passing through the gas channel. The control volume for thermal-fluidic entropy generation is shown in Figure 3.2.

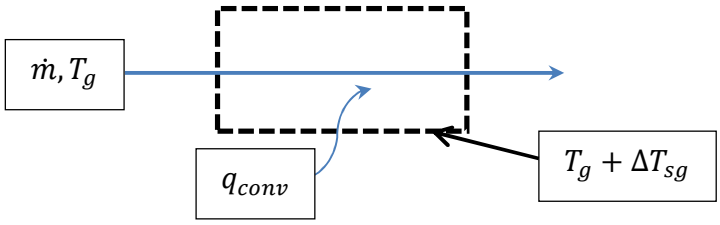

Figure 3.2. Control volume of the oxidant used to derive the entropy generation formulation.

For the control volume with a length of Δx shown in Figure 3.2, the steady state energy and entropy balances reduce to:

$$\dot{m}\Delta h = q_{conv} \text{ (Energy balance, } \Delta h = h_{out} - h_{in})$$

$$\dot{m}\Delta s = \frac{q_{conv}}{T_g + \Delta T_{sg}} + S_{gen} \text{(Entropy balance, } \Delta s = s_{out} - s_{in})$$

Rearranging the entropy balance: $S_{gen} = \dot{m}\Delta s - \frac{q_{conv}}{T_g + \Delta T_{sg}}$

Utilizing fundamental the property relationship:

$$ds = \frac{dh}{T} - \frac{v}{T}dP$$

Rewriting in finite difference form: $\Delta s = \frac{\Delta h}{T} - \frac{v}{T}\Delta P$

Substituting into entropy balance equation: $S_{gen} = \dot{m}\left(\frac{\Delta h}{T} - \frac{v}{T}\Delta P\right) - \frac{q_{conv}}{T_g + \Delta T_{sg}}$

Substituting into the energy balance equation: $S_{gen} = \left(\frac{q_{conv}}{T_g} - \dot{m}\frac{v}{T_g}\Delta P\right) - \frac{q_{conv}}{T_g + \Delta T_{sg}}$

Rearranging: $S_{gen} = \left(\frac{q_{conv}}{T_g} - \dot{m}\frac{v}{T_g}\Delta P\right) - \frac{q_{conv}}{T_g + \Delta T_{sg}} = \frac{q_{conv}\Delta T_{sg}}{T_g(T_g + \Delta T_{sg})} - \dot{m}\frac{v}{T_g}\Delta P$

$$S_{gen} = \frac{q_{conv}\Delta T_{sg}}{{T_g}^2\left(T_g + \frac{\Delta T_{sg}}{T_g}\right)} - \dot{m}\frac{v}{T_g}\Delta P$$

Normalizing the entropy generation equation by the volume of the control volume of a slice, and substituting the reciprocal of density for specific volume, yields Equation 3.3b.

$$g_{tf} = \frac{q_{conv}\cdot\Delta T_{sg}}{V_{slice}\cdot T_g^2\left(1+\Delta T_{sg}/T_g\right)} + \frac{\dot{m}}{\rho\cdot T_g}\frac{\Delta P}{V_{slice}} \qquad (3.3(b.))$$

Equation 3.3c was formulated by Bejan [23]. It details the entropy generation due to heat conduction in the solid volume. Bejan's control volume is shown in Figure 3.3 and derivation of the entropy generation follows.

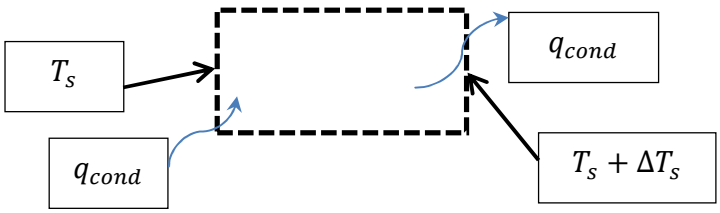

Figure 3.3. Control volume of the solid used to derive the entropy generation formulation.

The entropy balance for the control volume shown in Figure 3.3 is given below:

$$S_{gen} = \frac{q_{cond}}{T_s} - \frac{q_{cond}}{T_s + \Delta T_s}$$

Rearranging yields:

$$S_{gen} = \frac{(T_s + \Delta T_s)q_{cond} - T_s q_{cond}}{T_s(T_s + \Delta T_s)} = \frac{\Delta T_s q_{cond}}{T_s^2\left(1 + \frac{\Delta T_s}{T_s}\right)} \cong \frac{\Delta T_s q_{cond}}{T_s^2}$$

Normalizing by the slice volume ($\Delta x A_{slice}$):

$$g_h = \frac{1}{T_s^2}\left(q_{cond} \cdot \frac{\Delta T_s}{\Delta x}\right)\frac{\mathbf{1}}{A_{slice}} \qquad (3.3(c.))$$

Note that $A_{,slice}$ is the cross-sectional area of the control volume (*i.e.,* in the axial direction).

Equation 3.3d-f encompass the entropy generation due to the electrochemical processes. For a solid oxide fuel cell, there are three modes of irreversibilities in the conversion of chemical energy into electrical energy: ohmic, activation, and concentration. Chapter 4 shows the calculation of each mode of chemical irreversibility. Ohmic, concentration, and activation losses are measured in voltage. By multiplying associated voltage loss by the local current generated and normalizing by the local cell temperature and slice volume, the electrochemical entropy generation is then calculated.

$$g_{ohm} = \frac{1}{T_s}(\eta_{ohm} \cdot i_{cv})\frac{\mathbf{1}}{V_{slice}} \qquad (3.3\ (d.))$$

$$g_{act} = \frac{1}{T_s}(\eta_{act} \cdot i_{cv})\frac{\mathbf{1}}{V_{slice}} \qquad (e.)$$

$$g_{conc} = \frac{1}{T_s}(\eta_{conc} \cdot i_{cv})\frac{\mathbf{1}}{V_{slice}} \qquad (f.)$$

3.1.2 Description of Dimensionless Geometric Parameters

To facilitate geometric optimization searches for feasible solutions, and allow for a basis of comparison, four dimensionless parameters were developed based upon the geometry of Figure 3.4. In Figure 3.4, a center unit cell is highlighted. In the given dissertation, only central

until cells were considered. Four dimensionless geometric parameters are detailed in Table 3.1. These parameters were chosen due to their impact upon physical phenomena, thereby impacting performance and thermal gradients.

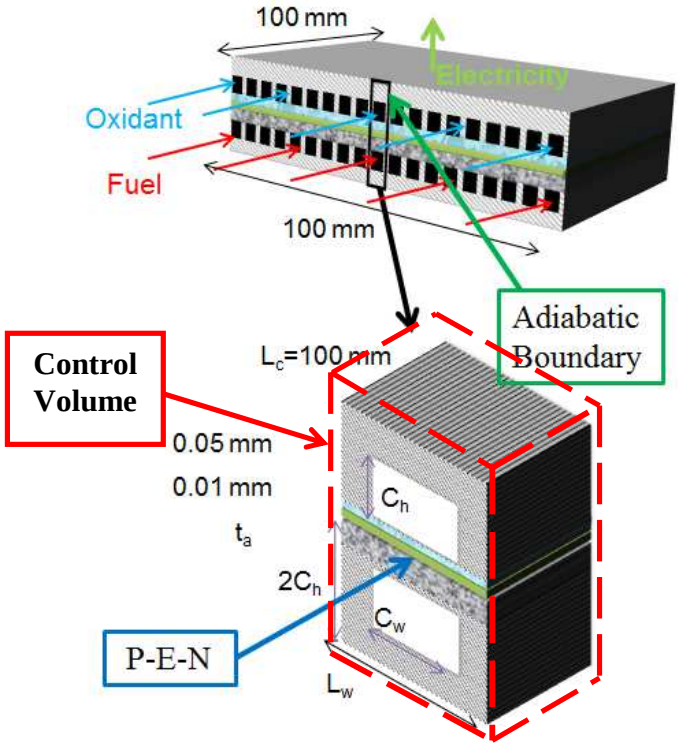

Figure 3.4. SOFC control volume for thermodynamic analysis. (not to scale)

Table 3.1. Dimensionless parameters and respective ranges.

Ratio	Range
Interconnect Aspect Ratio (IAR=C_w / C_h)	0.2 ≤ IAR≤5
Electrode/Electrolyte Ratio (EER=t_a / t_e)	10 ≤ EER≤100
Slenderness Ratio (SR =L_c /L_w)	5≤ SR≤100
Dimensionless Gas Channel Width (DGCW=C_w/L_w)	0.1≤ DGCW≤0.9

As previously stated, the optimization is facilitated through modification of dimensionless geometric parameters. The four dimensionless geometric parameters are as follows: Internal Aspect Ratio (IAR), Electrode-to-Electrolyte Ratio (EER), Slenderness Ratio (SR), and Dimensionless Gas Channel Width (DGCW) as summarized in Table 3.1 along with baseline values and feasible ranges.

Interconnect Aspect Ratio (IAR = C_w / C_h) is the ratio of gas channel width to gas channel height. IAR details how gas channel width and gas channel height relate to the available reactants for electrochemical reactions and convective cooling. IAR impacts total cell losses and heat transfer within the cell. Changes in IAR cause the hydraulic diameter to change and directly impact the convective heat transfer coefficients. Figure 3.5 shows how the cell geometry changes with IAR. It should be noted that the interconnect height is prescribed to be twice the height of the gas channel (*i.e.,* C_h). This fact will impact the calculation of cross-sectional area and thermal conductance. Thermal conductance is the product of thermal conductivity and the cross-sectional area of the solid. Notice in Figure 3.5, cross-sectional area of the solid decreases as IAR increases. This would imply that thermal conductance would also decreases as IAR increases.

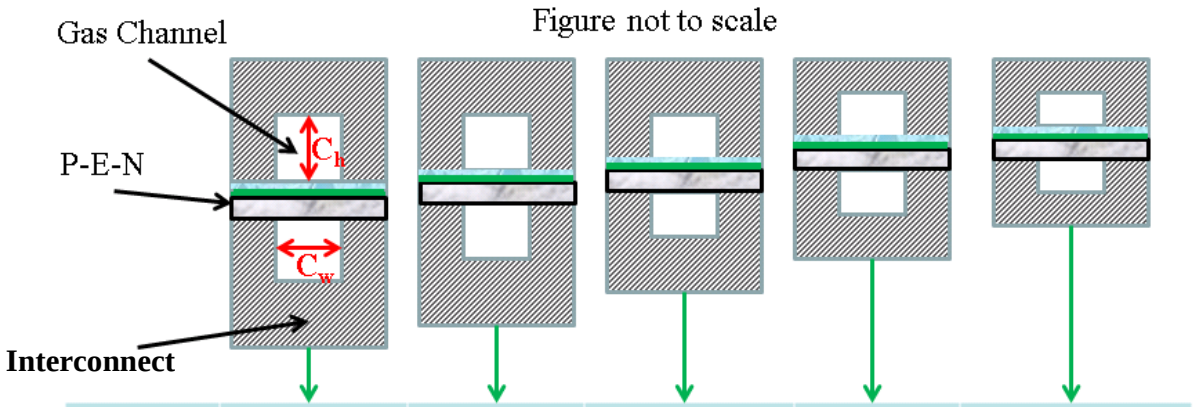

IAR	0.2	0.5	1	2	5
C_w (mm)	2	2	2	2	2
C_h (mm)	10	4	2	1	0.4

Figure.3.5. Schematic of changing geometry with IAR.

Dimensionless Gas Channel Width (DGCW=C_w/L_w) is the ratio of the gas channel width to the width of the cell. DGCW relates to the access to available sites for electrochemical reactions, which impacts ohmic and polarization losses. DGCW correlates both internal and external dimensions to performance and thermal gradients. The geometry configurations and dimensions used in the sensitivity study of DGCW are shown in Figure 3.6.

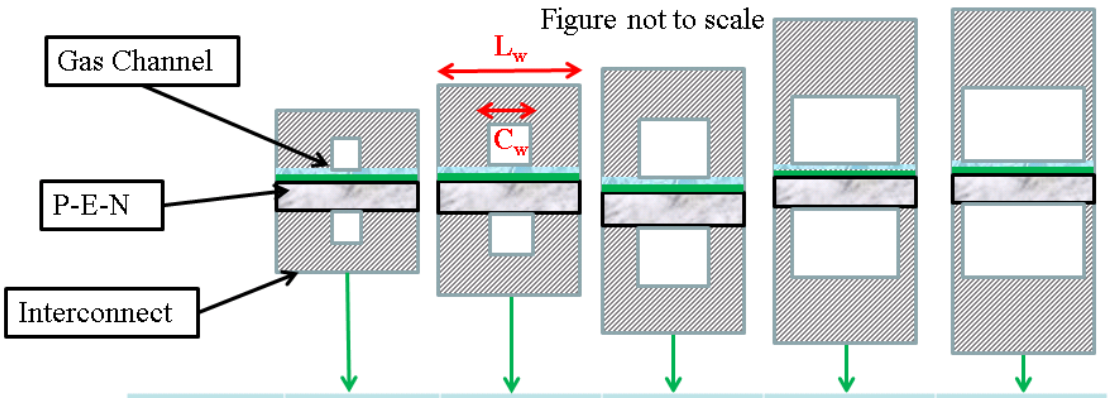

DGCW	0.10	0.25	0.50	0.75	0.90
C_w (mm)	0.4	1	2	3	3.6
L_w (mm)	4	4	4	4	4

Figure 3.6. Schematic of changing geometry with DGCW.

The third parameter is Slenderness Ratio (SR=L_c /L_w), which is the ratio of unit cell length to the unit cell width. SR is an excellent ratio to detail how external dimensions impact temperature profiles and gradients. Figure 3.7 shows how the geometry changes with SR.

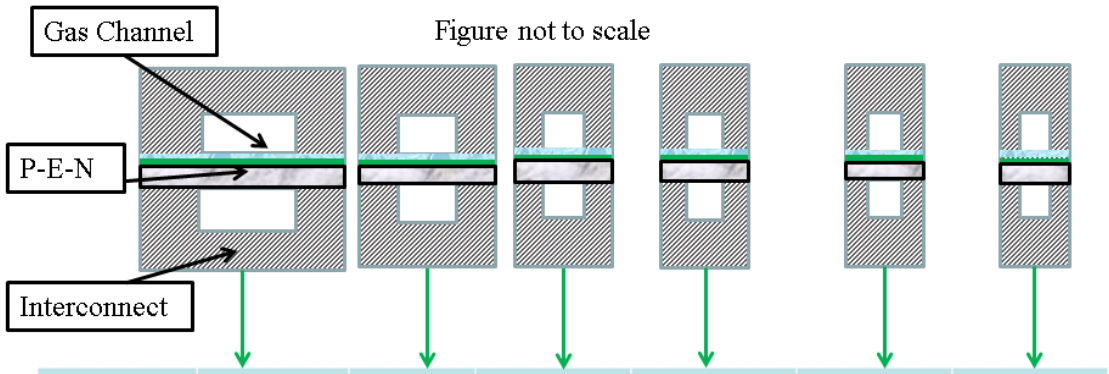

SR	5	10	25	50	75	100
L_c (mm)	100	100	100	100	100	100
L_w (mm)	20	10	4	2	1.33	1

Figure 3.7. Schematic of changing geometry with SR.

Electrode/Electrolyte Ratio (EER= t_a/ t_e) is the fourth selected parameter and is the ratio of the anode thickness to the electrolyte thickness. EER impacts ohmic and concentration losses. The thickness of each layer of the P-E-N is directly related to ohmic losses. EER was selected to correlate the P-E-N design to performance. Current planar architecture utilizes a thin electrolyte approach (*i.e.,* EER on the order of 50). As EER increases, the concentration losses will increase because of the greater distance that the electroactive constituents will have to diffuse. Figure 3.8 shows how the geometry changes with EER.

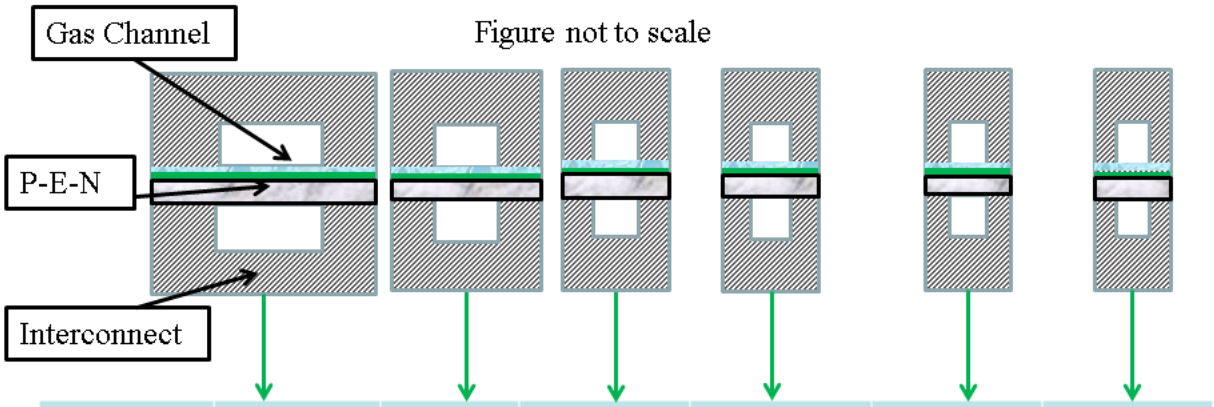

SR	5	10	25	50	75	100
L_c (mm)	100	100	100	100	100	100
L_w (mm)	20	10	4	2	1.33	1

Figure 3.8. Schematic of changing geometry with EER

The dimensionless geometric variables and constraints shown in Table 3.1 were first used to ascertain which geometric ratios have the greatest impact on performance and temperature gradient. From this analysis, the appropriate geometric ratios were used in the optimization study. The range of permissible thermal gradients are based upon the work of Nakajo [2]. Exergetic efficiency, power density, and fuel cell efficiency are the measures of performance with an emphasis on exergetic efficiency. 1st law metrics are still very important to

the analysis of fuel cell performance. However, for the sake of thermodynamic optimization, exergetic efficiency is the primary measure of performance. In order to conduct the performance analysis and optimization, conventional values of current density, fuel and oxidant utilization, and inlet species composition were selected. The selected operating conditions are discussed further in the next section. Exploration of the impact of those operating conditions are outside of the scope of the present dissertation, but may be considered a possibility for future work.

3.2 Optimization Approach

3.2.1 Overview of Optimization Problem

A single objective constrained optimization problem is solved in the present dissertation. In defining an optimization problem, the objective(s) and constraint(s) must be clearly stated. Keeney [88] has classified objectives as either fundamental or a means objectives. A fundamental objective is the essential reason for the design problem. A means objective is a reason or manner of achieving the fundamental objective(s). For the dissertation, the fundamental objective is to maximize exergetic efficiency while constraining thermal gradients. The related means objective is to minimize gross entropy generation. Table 3.2 describes and summarizes the optimization problem in terms of fundamental and means objectives and associated equations. In Table 3.2, $\varepsilon_{\mathrm{II}}$ is 2$^{\mathrm{nd}}$ law efficiency, and $\frac{\partial \mathrm{T}}{\partial \mathrm{z}}$ are thermal gradients down the axial length of the PEN quantified in °°C/m. By minimizing total entropy generation, maximum exergetic efficiency can be achieved. To ascertain the impact of constraints on cell design and the optimal solution, the constraints were varied as shown in

Table 3.2. Thermal gradients were varied between 250 °C/m to 2000 °C/m. Exergetic efficiency, $\varepsilon_{\mathrm{II}}$, and 1st law efficiency, ε_{I} , are defined in Equations 3.4 and 3.5, respectively.

Table 3.2. Description of optimization problem solved in dissertation.

Optimization Problem	
Fundamental objective	Maximize: $\varepsilon_{\mathrm{II}}$
Means objective	Minimize: $\mathrm{g_p} = \mathrm{g_{tf}} + \mathrm{g_h} + \mathrm{g_{ohm}} + \mathrm{g_{act}} + \mathrm{g_{conc}}$
Constraint	$\frac{\partial \mathrm{T}}{\partial \mathrm{z}} \leq \frac{\partial \mathrm{T}}{\partial \mathrm{z}_{\max}}$ (250 °C/m – 2000 °C/m)

$$\varepsilon_{II} = \frac{P_{cell}}{P_{cell}+E_{destruction}} \quad (3.4(a.))$$

$$P_{cell} = iV \quad (b.)$$

$$E_{destruction} = T_o\dot{S}_{gen} \quad (c.)$$

$$\varepsilon_I = \frac{P_{cell}}{\dot{n}_{fuel}LHV_{fuel}} \quad (3.5)$$

In Equation 3.4, P_{cell} is the power of produced by the entire unit cell, *i* is the current generated by the unit cell, V is the cell potential, and $\dot{S}_{gen}$ is the entropy generation for the entire fuel cell. In Equation 3.5, LHV_{fuel} is the lower heating value of the fuel.

3.3 Overview of Search Method

Search methods employed to arrive at the optimal solution for constrained single objective problems can be complex for engineering problems. A simple parametric search approach is suitable for engineering problems if the design space can be reasonably selected and the simulation time is tolerable. For the dissertation, the computational tools are sufficiently rapid and there is adequate knowledge of the design space to properly assign

parameter ranges. After conducting a performance analysis, the range and resolution of each dimensionless geometric parameter were refined. Table 3.3 shows the refined range and resolution. The refined ranged are explained in the next chapter. For the given range and resolution of values, there exist 392 cases. The 392 cases were calculated from the possible combinations of selected discrete values of each dimensionless geometric parameter. The number of possible values for IAR, EER, SR, and DGCW are 8, 1, 49, and 1, respectively. The product of these possible values yields 392. Table 3.4 shows the operating parameters. A current density of 0.4 A/cm^2 is used for the optimization, in order to realize higher efficiencies.

In summary, a selected optimization domain is solved. Then, based upon the range of thermal gradients considered, the solution space is searched to find the maximum 2nd law efficiency that is within the specified thermal gradient constraint.

Table 3.3. Refined dimensionless parameters, baseline values, and respective ranges.

Ratio	Range	Resolution
Interconnect Aspect Ratio (IAR=C_w / C_h)	0.25 ≤ IAR≤2	0.25
Electrode/Electrolyte Ratio (EER=t_a / t_e)	50	---
Slenderness Ratio (SR =L_c /L_w)	4≤ SR≤100	2
Dimensionless Gas Channel Width (DGCW=C_w/L_w)	0.25	---

Table 3.4. Operating parameters for performance analysis.

Operating Parameters	Value
NOS	7
Fuel Utilization	0.85
Current Density	0.6 A/cm^2
Inlet Oxidant Temp.	873K

4 1D SOLID OXIDE FUEL CELL MODEL

4.1 Model Description

A 1-D distributed, transient fuel cell model was developed in Matlab-Simulink™. The published model [89] simulates a co-flow, anode-supported SOFC. The SOFC model characterizes a representative cell on a spatially distributed basis in the direction of fuel and oxidant flow (*i.e.,* down the direction of the flow channel) and employs a coupled finite difference/ finite volume approach. The finite difference methodology is applied to the resolution of the solid and oxidant stream thermal profiles, and the finite volume approach is used for the electrochemical characterization. The level of discretization in the flow direction is variable but sensitivity studies supported employing 40 “nodes”/”volumes” (*i.e.,* points of calculation) along the length of the SOFC. The discretization scheme is illustrated in abbreviated fashion (only 7 “nodes”) in Figure 4.1.

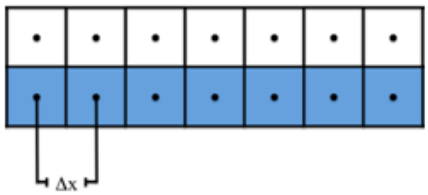

Figure 4.1. 1-D SOFC model discretization. The white and shaded regions are the gas and ”solid” volumes, respectively. Properties are locally uniform for each volume.

In the schematic presented in Figure 4.1, the two levels of nodes/volumes illustrated represent the oxidant stream and SOFC ”solid” (which is actually taken to be the integrated average of SOFC balance materials including the PEN, interconnects and fuel stream), respectively. The fuel stream is presumed to quickly come into thermal equilibrium with the

solid. As illustrated, the discretization scheme is the same for both regions. This allows the thermal communication between the two to be readily modeled. The model was developed to resolve temperature profiles of both the “solid” SOFC material as well as the oxidant stream. Note that, given the anticipation of lower mass flow rates and higher inlet temperatures, the fuel stream’s participation in heat transfer was approximated to be minor in comparison to the oxidant stream.

Given the hypothesis of the dissertation, the cell geometry of the simulated SOFC can be varied by the operator and is established in the model via user prescribed inputs. The required geometric parameters include:

- Total cell length, width and height
- Oxidant channel height and width
- Anode, cathode and electrolyte thicknesses
- Number of channels

The four dimensionless geometric parameters, IAR, DGCW, SR, and EER, describe the required geometric parameters. The three constraints on the cell geometry include:

1.) Total cell width is 100 mm

2.) Total cell length is 100 mm

3.) The fluid channels must be rectangular in cross-section

The imposed geometric constraints allow for a basis of comparison for the various geometric designs to be explored.

In addition to the geometric parameters, the necessary operational inputs are as follows:

- Cathode inlet parameters:

    - Temperature, pressure and mass flow rate
- Current demand
- Fuel flow
- Fuel composition

Given the 1-D distributed characterization, internal profiles of various SOFC operating results can be acquired on a spatial-temporal basis. A comprehensive list of those parameters is provided below.

- Solid temperature
- Oxidant temperature
- Local current density
- Nernst potential
- Electrochemical losses
    - Activation, Concentration, Ohmic
- Fuel species partial pressures
- By-product heat generation
- Entropy generation

4.1.1 Geometry

For the case studies presented in this dissertation, the operation of a co-flow SOFC with a 100 mm x 100 mm electroactive area is simulated. As shown previously, Figure 4.2 illustrates the geometry of a unit cell. In Figure 4.2, the anode thickness, t_a, channel width, C_w, channel height, C_h, and unit cell width, L_w, are prescribed by the dimensionless parameters IAR, DGCW, SR, and EER.

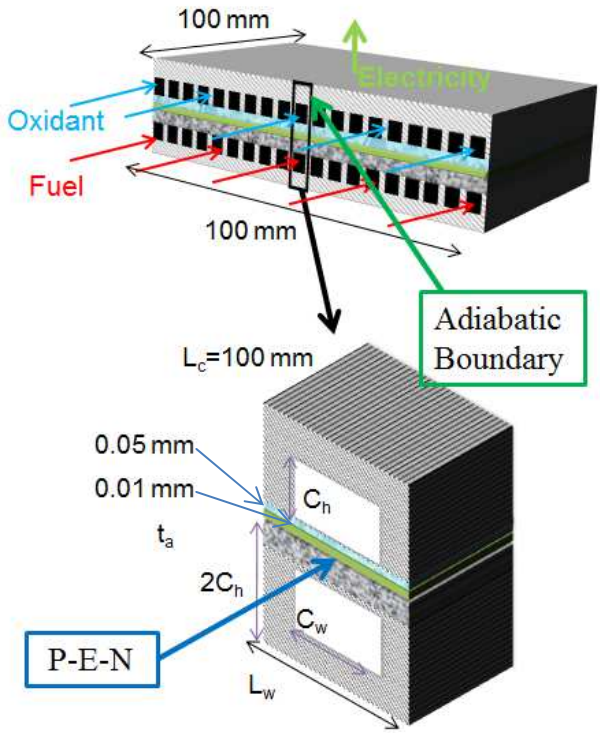

Figure 4.2. SOFC unit cell geometry (not to scale).

4.1.2 Assumptions

The following set of assumptions was employed when constructing the presented model.

- Fuel is comprised of humidified hydrogen with 90% H_2 and 10% H_2O. Syn gas mixtures are not considered.
- Air is presumed to be 79% N_2 and 21% O_2
- Each local control volume has unform properties (temperature, pressure, species concentration)
- Hydrogen is the only electrochemically active constituent in the fuel channel

- The fuel temperature quickly matches the temperature of the solid materials and thereby is apart of the solid composite for the thermal calculations. Verification of this assumption is given in the next subsection.
- In situ radiation heat transfer is considered negligible in the gas channels
- Boundary Conditions:
    - Inlet oxidant temperature is prescribed to be 600 C.
    - The exit of the oxidant stream is adiabatic.
    - The inlet and exit of the solid convects and radiates heat to a surrounding gray diffuse enclosure fixed at 600 C. The convective heat transfer is presumed to be via natural convection. However, it should be noted that the manifolding at the inlet and exit create impinging flow at the inlet and escaping effluent at the exit. The heat transfer coefficient in actuality is a mixture of forced convection and free convection. However, the analysis of the heat transfer in the manifolding is beyond the scope of the present dissertation. The free convection presumption is sufficient.

4.1.3 Verification of Fuel Stream Temperature Assumption

As was mentioned in the Assumptions subsection, the fuel stream temperature quickly approaches the temperature of the solid composite. For the control volume shown in Figure 4.3, a calculation of the distance at which the fuel stream temperature approaches the temperature of the surrounding solid materials is now given. The following assumptions are given for the calculation:

- Constant wall temperature analysis is used.
- Temperature of solid materials is fixed at 800°C.
- A mean temperature for the fuel in the cross-section of the control is presumed.
- Inlet temperature of the fuel is 600°C.
- All properties are constant in the control volume.
- Geometric parameter: Channel width and channel height are 2.08 mm. Fuel channel perimeter, P, is 8.32mm. Channel hydraulic diameter, D_{hyd}, is 1mm.
- For 0.4 A/m^2 current density, NOS of 7 and fuel utilization of 85% and 24 pairs of gas channels, the mass flow rates are: $\dot{m}_{ox}$= 4.18 x 10^{-7} kg/s, $\dot{m}_{fuel}$= 4.08 x 10^{-8} kg/s
- Fuel properties: k_{fuel} = 0.26 W/(m-K), $c_{p,fuel}$ = 8.67 kJ/kg, h_{fuel} = 774 W/m^2-K
- Fuel channel heat transfer coefficient: h_{fuel} = 774 W/(m^2-K)
- Oxidant specific heat: $c_{p,air}$ = 1.14 kJ/kg

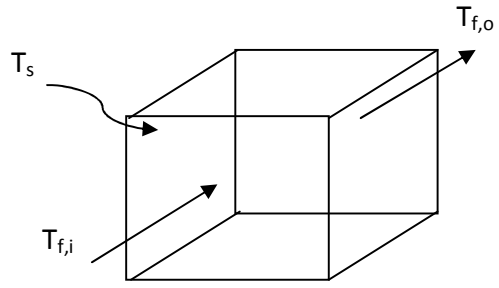

Figure 4.3. Diagram for the fuel stream temperature analysis.

The constant wall temperature internal convection problem has been previously solved by Incropera and Dewitt [90]. Equation 4.1 shows the solution. The goal is the find the distance, x, at which the fuel temperature approaches the temperature of the solid *(i.e.,* is 99% of the solid

temperature). A sufficiently short distance will indicate safe presumption of lumping the fuel stream and solid temperatures together.

$$\frac{T_s - T_f(x)}{T_s - T_{f,i}} = \exp\left(-\frac{P \cdot x}{\dot{m}_{fuel} c_{p,fuel}} h_{fuel}\right) \tag{4.1}$$

Rearranging Equation 4.1 and assigning the exit temperature of the fuel to be 99% of the solid temperature yields, an expression for x is yielded:

$$x = \frac{\dot{m}_{fuel} c_{p,fuel}}{P \cdot h_{fuel}} \cdot -1 \cdot \ln\left(\frac{0.01 T_s}{T_s - T_{f,i}}\right)$$

Substituting in the values and solving produces:

$$x = \frac{3.54x10^{-4} W/K}{0.00832m \cdot 774\ W/(m^2K)} \cdot -1 \cdot \ln\left(\frac{0.01 \cdot 1073K}{1073K - 873K}\right)$$

$$x = 0.160mm$$

Given that the discretized control volume has an axial length of 2.5mm, the fuel stream will approach the temperature of the solid within the first 6.4% (at 0.160mm) of the axial length of the discretized control volume. Since the fuel stream temperature approaches the solid temperature in a sufficiently short distance, it is safe to lump the fuel stream with the solid composite for the temperature calculations. This result is also supported by the work of Li *et al* [91] who analyzed the fuel stream, solid, and oxidant stream temperature for a co-flow planar SOFC. Figure 4.4 shows the temperature profiles obtained by the work. A fundamental reason for the fuel stream having temperatures that quickly approach the temperatures of the solid materials is due to the relatively low heat capacitance. The ratio of the oxidant stream heat capacitance to the fuel stream heat capacitance for the example above is 13.54. This is also why of the oxidant stream is used as a heat sink for the fuel cell.

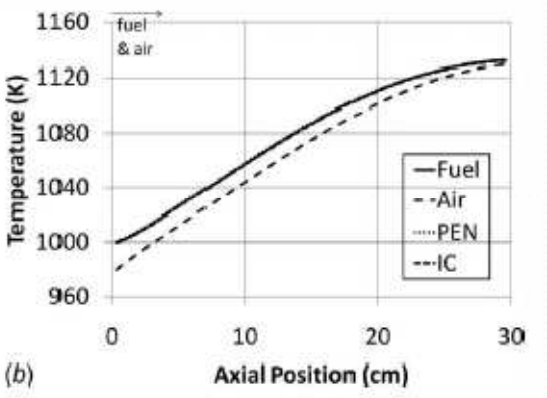

Figure 4.4. Temperature profile comparison done by Li *et al* [91]. The fuel stream, P-E-N, and interconnect (IC) have essentially identical profiles.

4.1.4 Biot Number Preliminary Analysis

It is presumed that thermal gradients in the axial direction are the dominant relative to those in the cross-section of the control volume. As heat conducts through the composite solid, there are two regions for potential adverse thermal gradients—in the P-E-N and solid composite. The relevant characteristic lengths are shown in the Figure 4.5. Equation 4.2 shows the Biot number formulation.

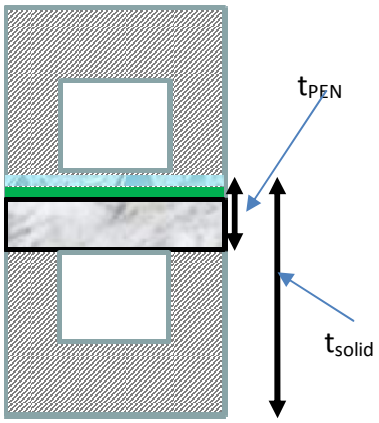

Figure 4.5. Cross-sectional view of the control volume displaying the characteristic lengths for Biot number calculations.

$$Bi = h_{avg} \sum_i \frac{t_i}{k_i} \tag{4.2}$$

In Equation 4.2, h_{avg} the average heat transfer coefficient, t_i is the conductive characteristic length, and k_i is the thermal conductivity of the solid material. For a baseline design with IAR of 1, DGCW of 0.25, and SR of 24 and standard operating conditions of 0.4 A/^{cm2}, NOS of 7, and fuel utilization of 85%, the Biot number in the P-E-N and solid thicknesses were calculated. The Biot number in the P-E-N was 0.0596 and 0.0196, respectively. These values are well below the critical Biot number of 0.1 thereby signifying cross-sectional thermal gradients are not significant. Due to the focus on axial thermal gradients (in the flow direction) in the present dissertation, the Biot number will be analyzed in the optimization study.

4.2 Electrochemical Model

4.2.1 Operating Voltage Calculation

The operating cell voltage is calculated by accounting for electrochemical losses and subtracting them from the local Nernst potentials. The relation used to determine operating cell voltage is presented in Equation 4.3, where V_{cell} represents the operating cell voltage, V_{Nernst} represents the Nernst potential, and η represents the electrochemical losses denoted by the respective subscripts. The methodology used to resolve the respective electrochemical terms are presented in subsequent subsections. The Nernst potential is the maximum possible voltage that can be obtained and is a function of temperature and partial pressures of the electrochemically active species. V_{Nernst} is derived from the Gibbs free energy of hydrogen oxidation and is calculated using Equation 4.3 [92].

$$V_{cell} = V_{Nernst} - \eta_{conc} - \eta_{act} - \eta_{ohm} \tag{4.3}$$

$$V_{Nernst} = \frac{-\Delta G^{o}_{H_2O}}{2F} + \frac{R_u T}{2F} \ln\left(\frac{p_{H_2} p_{O_2}^{\frac{1}{2}}}{p_{H_2O}} \right) \tag{4.4}$$

In the given equation used to calculate the Nernst potential, $-\Delta G°_{H2O}$ represents the Gibbs free energy decrease during the formation of water at STP, F represents Faraday's constant, R_u the universal gas constant and, p represents the magnitudes of the partial pressures of the respective electrochemically active species in atmospheres.

4.2.2 Concentration Polarization

The electrochemical reactions in operating fuel cells take place at the electrode-electrolyte-reactant stream interface, also known as the triple phase boundary (TPB). Due to diffusive effects through the anode and cathode, reactant concentrations at the reaction sites will differ from their bulk concentrations in the fuel and oxidant streams. The difference in concentration (or partial pressure) between the reactant stream and (TPBs) due to these diffusive effects manifests as a loss in voltage. This concentration polarization, referenced in Equation 4.3, is quantitatively presented in Equation 4.5 [93].

$$\eta_{conc} = \frac{R_u T}{2F} \left(\ln\left(\frac{x_{H_2,bulk}}{x_{H_2,TPB}} \frac{x_{H_2O,TPB}}{x_{H_2,Obulk}} \right) + \frac{1}{2} \ln\left(\frac{x_{O_2,bulk}}{x_{O_2,TPB}} \right) \right) \tag{4.5}$$

The reactant mole fractions at the TPB ($x_{i,TPB}$) are resolved using Equations 4.6-4.8 [92, 94].

$$x_{H_2,TPB} = x_{H_2,bulk} - \frac{R_u T}{2F} \frac{i\delta_{an}}{p_{an} D_{an,eff}} \tag{4.6}$$

$$x_{H_2O,TPB} = x_{H_2O,bulk} + \frac{R_u T}{2F} \frac{i\delta_{an}}{p_{an} D_{an,eff}} \tag{4.7}$$

$$x_{O_2,TPB} = 1 + \left(x_{O_2,bulk} - 1\right) \exp\left(\frac{R_u T}{4F} \frac{i\delta_{ca}}{p_{ca} D_{ca,eff}}\right) \tag{4.8}$$

For the sake of computational burden and as justified by applicable work in the SOFC field [5, 93, 95], the assumption of hydrogen as the only electrochemically active specie supports the assumption of equimolar counter diffusion of H_2O and H_2 on the anode side. In Equation 4.5, δ_{an} is the thickness of the anode. The anode thickness' impact on performance will be reflected in EER through concentration losses.

The model resolves ordinary binary diffusion coefficients using the Fuller-Schettler-Giddings method presented in Equation 4.9 [96].

$$D_{12} = \frac{0.00143 T^{1.75}}{p M_{12}^{1/2} \left[\left(\sum v\right)_1^{1/3} + \left(\sum v\right)_2^{1/3}\right]} \tag{4.9}$$

For Equation 4.9, *T* and p represent the temperature and pressure of the mixture, respectively. The effective molecular weight, M_{12}, that is used to resolve the ordinary diffusion coefficient, is presented in Equation 4.10.

$$M_{12} = 2\left[\left(\frac{1}{M_1}\right)+\left(\frac{1}{M_2}\right)\right]^{-1} \tag{4.10}$$

The effective diffusivity coefficient presented in Equation 4.9 accounts for only ordinary (binary) diffusion. The Knudsen diffusivity of each species is resolved using Equation 4.10; and the effective diffusion coefficient for each species, which accounts for both ordinary and Knudsen diffusion, is presented in Equation 4.11. The characteristic pore diameter used is presented in Table 4.1 [94, 97].

$$D_{K1} = 48.5 d_{pore}\left(\frac{T_{PEN}}{M_1}\right)^{1/2} \tag{4.11}$$

$$D_{1,eff} = \frac{\varepsilon}{\tau}\left(\frac{1}{D_{12}}+\frac{1}{D_{1K}}\right)^{-1} \tag{4.12}$$

The electrode-specific diffusivities for anode and cathode are presented in Equations 4.13 and 4.14, respectively [5, 94].

$$D_{an,eff} = \left(\frac{p_{H_2O}}{p_{an}}\right)D_{H_2,eff} + \left(\frac{p_{H_2}}{p_{an}}\right)D_{H_2O,eff} \tag{4.13}$$

$$D_{ca,eff} = D_{O_2,eff} \tag{4.14}$$

A correction factor which is used to account for the error associated with using Fick's law to characterize diffusion during SOFC operation is included in the resolution of the diffusion coefficient [97]. The empirically resolved correction factor accounts for the impact of current draw on diffusion through the porous electrodes and is presented in Equation 4.15.

$$D_i^{eff^*} = D_i^{eff}\left(1+sign\left(v_i\right)c\frac{i}{i_{ref}}\right)^n \tag{4.15}$$

The effective diffusivity is calculated in Equation 4.12. The v_i term is the stoichiometric coefficient of the species of interest and i is the total current density. The constants i_{ref}, c and n are empirically resolved and presented in Table 4.1.

Table 4.1. Parameters used in calculation of concentration losses.

Concentration Polarization [94, 97]	
Pore diameter, d_{pore} (anode and cathode)	$1x10^{-6}$ m
Porosity, ε (anode and cathode)	0.5
Tortuosity, τ (anode and cathode)	3
Diffusion Coefficient Correction [97]	
C	$4.88x10^{-4}$
N	2
i_{ref}	1 A/m^2
Diffusion Volumes [96]	
H_2	6.12
H_2O	13.1
O_2	16.3
N_2	18.5

4.2.3 Activation Polarization

The activation polarization represents the electrochemical loss associated with overcoming the activation energy for electrochemical activity at each electrode. The development of the activation polarization is derived from the Butler-Volmer expression, which is presented in Equation 4.16.

$$i = i_o \left(\exp\left(\frac{\alpha n F \eta_{act}}{R_u T_{PEN}} \right) - \exp\left(\frac{-(1-\alpha) n F \eta_{act}}{R_u T_{PEN}} \right) \right) \tag{4.16}$$

In Equation 4.16, i represents the current density, i_o represents the exchange current density, η_{act} represents the activation polarization, n represents the number of electrons transferred, which is taken to be 1 (in terms of individual electron transferred) rather than 2 (number of electrons transferred per oxygen ion) as clarified by Hernandez-Pacheco et al. [94, 98] and α represents the transfer coefficient or the symmetry factor which is commonly taken to be 0.5 [92, 99].

The governing Butler-Volmer expression is implicit with respect to activation polarization as illustrated in Equation 4.16. Given that current density is a fuel cell model input and activation polarization is explicitly required to resolve the SOFC operating voltage, implicitly resolving activation polarization using this equation poses a significant computational burden. Accordingly, an approach toward developing an explicitly defined mathematical approximation for the activation polarization is warranted. The approach developed by Noren and Hoffman is used in this model and presented in Equation 4.17 [94, 99].

$$\eta_{act} = \left(\frac{R_u T_{PEN}}{\alpha n F} \right) \sinh^{-1} \left(\frac{i}{2 i_o} \right) \tag{4.17}$$

Each electrode individually contributes to the activation polarization for the entire cell, thus, Equation 4.17 must be applied to both the anode and cathode. Expressions for the exchange current density of the anode and cathode, respectively, are required and adopted from Li [94, 98, 100] as presented in Equations 4.18 and 4.19.

$$i_{o,an} = \gamma_{an} \left(\frac{p_{H_2}}{p_{amb}} \right) \left(\frac{p_{H_2O}}{p_{amb}} \right) \exp \left(- \frac{E_{act,an}}{R_u T_{PEN}} \right) \tag{4.18}$$

$$i_{o,ca} = \gamma_{ca} \left(\frac{p_{O_2}}{p_{amb}} \right)^{0.25} \exp \left(- \frac{E_{act,ca}}{R_u T_{PEN}} \right) \tag{4.19}$$

Parameter values for the activation polarization are presented in Table 4.2 [92, 101].

Table 4.2. Parameter values for activation polarization.

Activation Polarization [94]	
Pre-exponential factors	Values
Anode, γ_{an}	5.5×10^8 A/m^2
Cathode, γ_{ca}	7×10^8 A/m^2
Activation Energies	
Anode, E_{an}	100 kJ/mol
Cathode, E_{ca}	120 kJ/mol
Transfer coefficient, α	0.5

4.2.4 Ohmic Losses

Ohmic loss accounts for the voltage loss due to the internal electrical resistance of the fuel cell. The model specifically accounts for electrical resistance due to the PEN and interconnect assembly as well as the oxide scale that forms during operation [93, 102]. The overall electrical resistance of the PEN and interconnect is a function of the temperature dependent resistivities as well as the geometry of the PEN and interconnect components (*i.e.,* thickness and cross-sectional area). Overall resistance of the PEN and interconnect is a summation of the resistances of each component and is presented in Equation 4.20. The interconnect resistance is calculated utilizing a circuit method to account for the current path as described by in Figure 4.6 and the work of Campanari [100].

$$R_{PEN} = \sum_{k=an,ca,ele} \left[\frac{\rho_k \delta_k}{A_k} \right] \tag{4.20 (a.)}$$

$$R_{IC} = \frac{1}{2}\left(\frac{R_{II} \cdot R_{III}}{R_{II} + R_{III}} + R_I \right) \tag{b.}$$

$$R_I = \frac{\rho_{IC} \cdot a}{z(c-b)} \tag{c.}$$

$$R_{II} = \frac{\rho_{IC} \cdot (d-a)}{z(c-b)} \tag{d.}$$

$$R_{III} = \frac{\rho_{IC}}{z} \cdot f\left(\frac{b}{d-a} \right) \tag{e.}$$

$$f\left(\frac{b}{d-a} \right) = \frac{1}{0.41 \cdot \left[1 - \exp\left(-1.2 \cdot \frac{b}{d-a} \right) \right]} \tag{f.}$$

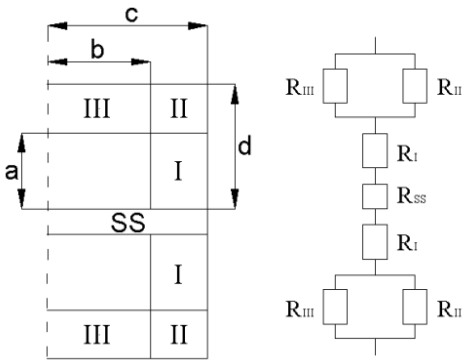

Figure 4.6. Schematic of network analysis to calculate the resistance of the interconnect accounting for the path of the current. Note that Rss is the resistance of the PEN.

Regarding equation nomenclature, δ_k represents the thickness of the PEN component, A_k represents the area normal to charge transport, ρ_k represents the temperature dependent resistivity of the respective PEN layer, and ρ_{IC} represents the temperature dependent resistivity of the interconnect for which equations are presented in Table 4.3. The calculation of the ohmic losses is based upon Ohm's Law as presented in Equation 4.21. Ohmic resistance is impacted by all four of the dimensionless geometric parameters.

Table 4.3. Parameters for calculating ohmic polarization .

Ohmic Polarization [94, 103]	
Temperature dependent resistivities, ρ	
Anode	$\left[\frac{95\times10^6}{T_{PEN}}\exp\left(-\frac{1150}{T_{PEN}}\right)\right]^{-1}\ \Omega-m$
Cathode	$\left[\frac{42\times10^6}{T_{PEN}}\exp\left(-\frac{1200}{T_{PEN}}\right)\right]^{-1}\ \Omega-m$
Electrolyte	$\left[3.34\times10^4\exp\left(-\frac{10.300}{T_{PEN}}\right)\right]^{-1}\ \Omega-m$
Interconnect	$\left[\frac{9.3\times10^6}{T_{PEN}}\exp\left(-\frac{1100}{T_{PEN}}\right)\right]^{-1}\ \Omega-m$

$$\eta_{ohm} = iA_{electroactive}\left[R_{PEN} + R_{oxide} + R_{IC}\right] \tag{4.21}$$

The R_{oxide} value was determined empirically by ThyssenKrupp and is provided by Material Data Sheet No. 4060 [102].[1]

4.3 Thermal Model

The thermal component of the model employed the work of Damm and Fedorov [10]. The thermal component of the model resolves the temperature profile for both the oxidant stream and the balance of the fuel cell assembly inclusive of both solid material and the fuel stream via an implicit/explicit finite difference methodology, which employs the use of a tri-diagonal matrix algorithm. As designed, the model accounts for conductive heat in the solid material, convective heat transfer between the oxidant and the SOFC; and heat generated due to chemical kinetics as well as cell operation. Encapsulated in the thermal model is also a temperature-dependent, thermophysical properties sub-routine which includes the empirically resolved thermophysical properties of SS441 which were resolved at NETL-Albany [104-106]. The model includes correlations that characterize the thermal behavior of SS441 over an exhaustive range of temperatures which transcend standard SOFC operation (300K-1800K).

The wide range of temperatures included in the model affords the capability to characterize a broad range of operating conditions including inert heating, electrochemical start-up or "light off", standard on-design operation, and off-design operation.

[1] The value was resolved using a contact (area-specific) resistance of 8 mΩ-cm^2 for the sake of this investigation based upon inspection of empirically resolved profiles as presented by ThyssenKrupp in Material Data Sheet No. 4060.

4.3.1 Heat Transfer Equations

The temperature profiles of the cathode airflow stream and the solid oxide fuel cell assembly are governed by Equations 4.23 and 4.24, respectively. Equations 4.23 and 4.24 are simplified into a two-equation model by considering all solid materials and the fuel channel as the "solid" node. Equation 4.23 shows the gas equation. Advection in the gas channel is considered on the left hand side of the equation. On the right hand side of the equation, convection between the gas and solid nodes is considered. The heat transfer coefficient, h, includes entrance length effects and the aspect ratio of the rectangular channels. The Nusselt number correlation is taken from Kakac *et al* [107]. In the entrance length, the Nusselt number is calculated by the tabular function shown in Table 4.5. The entrance length and spatial term, d, are described in Equation 4.22. The entrance length is 5 percent of the hydraulic diameter normalized by the Peclet number. Beyond the entrance length, the Nusselt number is calculated using the correlation shown in Table 4.5.

$$L_{entrance} = 0.05\, D_h /(Re \cdot Pr) \qquad (4.22\ (a.))$$

$$d = x/((Re \cdot Pr) \cdot D_h) \qquad (b.)$$

Table 4.4. Parameters for Nusselt number calculation taken from Kakac *et al* [107].

Nusselt Number Correlation[108]		
Aspect Ratio (IAR)	Nu entrance	Nu
1	$1.4141d^{-0.2468}$	$7.541(1-2.61IAR+4.97IAR^2-5.119IAR^3+2.702IAR^4)$
1/2 or 2	$1.7766d^{-0.2154}$	
1/3 or 3	$2.345d^{-0.1767}$	
1/4 or 4	$2.8075d^{-0.1534}$	$0.05L_{entrance} \leq d \leq L_{entrance}$ If Re>2300, $5 + 0.015(Re^a)(Pr^b)$, where $a=0.88-0.24/(4+Pr)$ $b=0.333 + 0.5e^{(-0.6Pr)}$
1/5 or 5	$3.3233d^{-0.1282}$	
1/6 or 6	$3.54d^{-0.1225}$	

$$\left(\rho c_p A\right)_g \left[\frac{\partial T_g}{\partial t} + u\frac{\partial T_g}{\partial z}\right] = \left(kA\right)_g \frac{\partial^2 T_g}{\partial z^2} + hP_{g-s}\left(T_s - T_g\right) \tag{4.23}$$

$$\sum_i \left(\rho c_p A\right)_i \frac{\partial T_s}{\partial t} = \sum_i \left(kA\right)_i \frac{\partial^2 T_s}{\partial z^2} + hP_{g-s}\left(T_g - T_s\right) + A_s q_{gen} \tag{4.24}$$

In Equations 4.23 and 4.24, $\left(\rho c_p A\right)$ is the heat capacitance of the gas or solid, u is the oxidant velocity, $\left(kA\right)$ is the thermal conductance (*i.e.,* the product of thermal conductivity and cross sectional area) of the gas or solid, P_{g-s}, is the perimeter of the gas channel, q_{gen} is the heat generation (W/m^3) in the solid due to electrochemical reactions after "light-off" and A_s is cross sectional area of the solid. The subscript, *i*, indicates to sum over every solid component (2 interconnects, anode, cathode, electrolyte, and fuel channel). The boundary and initial conditions are,

gas boundary conditions:

$$T_g(0,t) = T_{g,inlet};\ \frac{\partial T_g}{\partial z}(L,t) = 0 \tag{4.25 (a.)}$$

gas initial condition:

$$T_g(z,0) = T_o \tag{b.}$$

solid boundary conditions:

$$(kA)_s \frac{\partial T_s}{\partial z}(0,t) = \left(h_{surf} + h_{rad}\right)A_{surf}(T_s - T_{amb}) \tag{c.}$$

$$-(kA)_s \frac{\partial T_s}{\partial z}(L,t) = \left(h_{surf} + h_{rad}\right)A_{surf}(T_s - T_{amb}) \tag{d.}$$

solid initial condition:

$$T_s(z,0) = T_o \tag{e.}$$

where h_{surf} is the free convective heat transfer coefficient of the inlet and exit surfaces of the control volume, h_{rad} is the linearized radiation heat transfer coefficient of the inlet and exit surfaces of the control volume, T_{amb} is the ambient temperature, ε is the emissivity of the inlet and exit surfaces of the control volume, A_{surf}, is the surface area of inlet and exit surfaces of the control volume, and T_o is the initial temperature (e.g. 25C). The Nusselt number correlation for free convection is given in Table 4.6, as well as, other key parameters for the boundary and inlet conditions.

Table 4.5. Parameters for boundary and initial conditions.

Parameter	Value or Correlation
Nu_{surf}	$Nu_{surf} = \left\{0.825 + \frac{0.387 Ra_L^{1/6}}{\left[1+(0.492/Pr)^{9/16}\right]^{8/27}}\right\}^2$ $Ra_L = gB_f L_h^3 (T_s - T_{amb})/(v\alpha)$ $B_f = 1/(T_s + T_{amb})$
T_{amb}	$T_{g,inlet}$
Emissivity	0.2(stainless steel) , 0.6 (ceramic)
h_{rad}	$\varepsilon\sigma(T_s + T_{amb})(T_s^2 + T_{amb}^2)$
$T_{g,inlet}$	600C
T_o	25C

In Table 4.6, the emissivity value was chosen to be a weighted average of the stainless steel and ceramic cell materials. The emissivity of stainless steel and ceramic cell materials were 0.2 and 0.6, respectively. These values were obtained from Modest [109]. The ambient temperature was prescribed to be that of the oxidant. This presumption is because of the metallic manifold used to transport reactants to and from the fuel cell. The metallic manifold is presumed to quickly approach the temperature of oxidant supply temperature. In Table 4.6, g is

gravitational acceleration (m/s^2), B_f is thermal expansion coefficient (K^{-1}), υ is kinematic viscosity of air (m^2/s), and α is thermal diffusivity of air (m^2/s).

4.3.2 Temperature Profile Resolution

The temperature profiles of the cathode airflow stream, as well as the solid oxide fuel cell assembly, are discretized using the finite difference approach presented in Figure 4.7. The finite difference approach utilizes a fractional implicit approach (with $0 \le \beta \le 1$ as a weighting factor). For the sake of computational stability and accuracy a β value of 0.74 (*i.e.,* fractional weighting of implicit formulation) was employed.

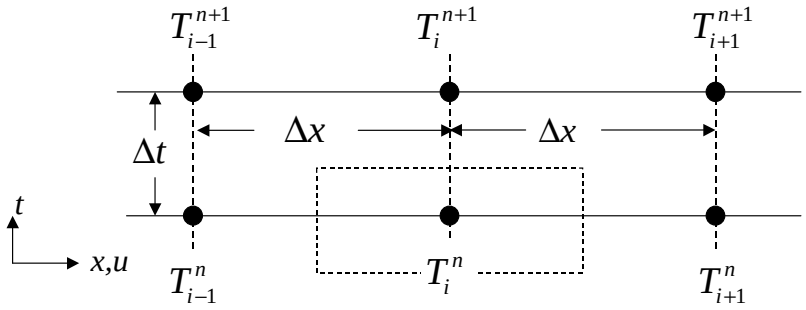

Figure 4.7. Scheme for discretizing the gas or solid phase of the channel with uniform grid spacing.

Equations 4.26 through 4.28 are discretized into sets of linear algebraic equations following the notation as in Figure 4.7. The discretized gas equation is,

$$
\begin{aligned}
&C_g A_c \frac{T_i^{n+1}-T_i^n}{\Delta t}\Delta x = \beta\left[k_g A_c \frac{T_{i+1}-2T_i+T_{i-1}}{\Delta x}+C_g A_c u\frac{T_{i-1}-T_i}{\Delta x}\Delta x - hP_{g-s}\left(T_i-T_{i,s}\right)\Delta x\right]^{n+1}\\
&\qquad +(1-\beta)\left[k_g A_c \frac{T_{i+1}-2T_i+T_{i-1}}{\Delta x}+C_g A_c u\frac{T_{i-1}-T_i}{\Delta x}\Delta x - hP_{g-s}\left(T_i-T_{i,s}\right)\Delta x\right]^{n}\\
&\qquad\qquad \downarrow\\
&C_g A_c T_i^{n+1} = C_g A_c T_i^n + \beta\Delta t\left[k_g A_c \frac{T_{i+1}-2T_i+T_{i-1}}{\Delta x^2}+C_g A_c u\frac{T_{i-1}-T_i}{\Delta x} - hP_{g-s}\left(T_i-T_{i,s}\right)\right]^{n+1}\\
&\qquad +(1-\beta)\Delta t\left[k_g A_c \frac{T_{i+1}-2T_i+T_{i-1}}{\Delta x^2}+C_g A_c u\frac{T_{i-1}-T_i}{\Delta x} - hP_{g-s}\left(T_i-T_{i,s}\right)\right]^{n}\\
&\qquad\qquad \downarrow\\
&-\frac{\beta\Delta t k_g A_c}{\Delta x^2}T_{i+1}^{n+1}-\frac{\beta\Delta t\left(k_g A_c + C_g A_c u\Delta x\right)}{\Delta x^2}T_{i-1}^{n+1}+\left[C_g A_c+\beta\Delta t\left(\frac{2k_g A_c + C_g A_c u\Delta x}{\Delta x^2}+hP_{g-s}\right)\right]T_i^{n+1}\\
&\qquad = \beta\Delta t hP_{g-s}T_{i,s}^{n+1}+C_g A_c T_i^n+(1-\beta)\Delta t\left[k_g A_c \frac{T_{i+1}-2T_i+T_{i-1}}{\Delta x^2}+C_g A_c u\frac{T_{i-1}-T_i}{\Delta x} - hP_{g-s}\left(T_i-T_{i,s}\right)\right]^{n}
\end{aligned}
\tag{4.26}
$$

and the solid equation is,

$$
\begin{aligned}
&C_s A_c \frac{T_i^{n+1}-T_i^n}{\Delta t}\Delta x = \beta\left[k_s A_c \frac{T_{i+1}-2T_i+T_{i-1}}{\Delta x}+hP_{g-s}\left(T_{i,g}-T_i\right)\Delta x + A_s q_{gen}\Delta x\right]^{n+1}\\
&\qquad +(1-\beta)\left[k_s A_c \frac{T_{i+1}-2T_i+T_{i-1}}{\Delta x}+hP_{g-s}\left(T_{i,g}-T_i\right)\Delta x + A_s q_{gen}\Delta x\right]^{n}\\
&\qquad\qquad \downarrow\\
&C_s A_c T_i^{n+1} = C_s A_c T_i^n + \beta\Delta t\left[k_s A_c \frac{T_{i+1}-2T_i+T_{i-1}}{\Delta x^2}+hP_{g-s}\left(T_{i,g}-T_i\right)+A_s q_{gen}\right]^{n+1}\\
&\qquad +(1-\beta)\Delta t\left[k_s A_c \frac{T_{i+1}-2T_i+T_{i-1}}{\Delta x^2}+hP_{g-s}\left(T_{i,g}-T_i\right)+A_s q_{gen}\right]^{n}\\
&\qquad\qquad \downarrow\\
&-\frac{\beta\Delta t k_s A_c}{\Delta x^2}\left(T_{i-1}^{n+1}+T_{i+1}^{n+1}\right)+\left[C_s A_c+\beta\Delta t\left(\frac{2k_s A_c}{\Delta x^2}+hP_{g-s}\right)\right]T_i^{n+1}\\
&\qquad = \beta\Delta t\left(hP_{g-s}T_{i,g}^{n+1}+A_s q_{gen}^{n+1}\right)+C_s A_c T_i^n+(1-\beta)\Delta t\left[k_s A_c \frac{T_{i+1}-2T_i+T_{i-1}}{\Delta x^2}+hP_{g-s}\left(T_{i,g}-T_i\right)+A_s q_{gen}\right]^{n}
\end{aligned}
\tag{4.27}
$$

The color coding in the discretized equations are as follows: red for unknown oxidant temperature, green for unknown solid temperature, and blue for known temperature. The boundary equations for the gas are, at the inlet,

$$C_g A_c \frac{T_1^{n+1}-T_1^n}{\Delta t}\Delta x = \beta\left[k_g A_c \frac{T_2-3T_1+2T_{g,inlet}}{\Delta x}+C_g A_c u\frac{T_{g,inlet}-T_1}{\Delta x}\Delta x - hP_{g-s}\left(T_1-T_{1,s}\right)\Delta x\right]^{n+1}$$
$$+(1-\beta)\left[k_g A_c \frac{T_2-3T_1+T_{g,inlet}}{\Delta x}+C_g A_c u\frac{T_{g,inlet}-T_1}{\Delta x}\Delta x - hP_{g-s}\left(T_1-T_{1,s}\right)\Delta x\right]^{n}$$
$$\downarrow$$
$$C_g A_c T_1^{n+1} = C_g A_c T_1^n + \beta\Delta t\left[k_g A_c \frac{T_2-3T_1+2T_{g,inlet}}{\Delta x^2}+C_g A_c u\frac{T_{g,inlet}-T_1}{\Delta x} - hP_{g-s}\left(T_1-T_{1,s}\right)\right]^{n+1} \qquad (4.28(a.))$$
$$+(1-\beta)\Delta t\left[k_g A_c \frac{T_2-3T_1+T_{g,inlet}}{\Delta x^2}+C_g A_c u\frac{T_{g,inlet}-T_1}{\Delta x} - hP_{g-s}\left(T_1-T_{1,s}\right)\right]^{n}$$
$$\downarrow$$
$$-\frac{\beta\Delta t k_g A_c}{\Delta x^2}T_2^{n+1}+\left[C_g A_c+\beta\Delta t\left(\frac{3k_g A_c+C_g A_c u\Delta x}{\Delta x^2}+hP_{g-s}\right)\right]T_1^{n+1} = \frac{\beta\Delta t\left(2k_g A_c+C_g A_c u\Delta x\right)}{\Delta x^2}T_{g,inlet}$$
$$+\beta\Delta t hP_{g-s}T_{1,s}^{n+1}+C_g A_c T_1^n+(1-\beta)\Delta t\left[k_g A_c \frac{T_2-3T_1+2T_{g,inlet}}{\Delta x^2}+C_g A_c u\frac{T_{g,inlet}-T_1}{\Delta x}-hP_{g-s}\left(T_1-T_{1,s}\right)\right]^{n}$$

and at the exit (assuming *M* nodes in space),

$$C_g A_c \frac{T_M^{n+1}-T_M^n}{\Delta t}\Delta x = \beta\left[k_g A_c \frac{-T_M+T_{M-1}}{\Delta x}+C_g A_c u\frac{T_{M-1}-T_M}{\Delta x} - hP_{g-s}\left(T_M-T_{M,s}\right)\Delta x\right]^{n+1}$$
$$+(1-\beta)\left[k_g A_c \frac{-T_M+T_{M-1}}{\Delta x}+C_g A_c u\frac{T_{M-1}-T_M}{\Delta x} - hP_{g-s}\left(T_M-T_{M,s}\right)\Delta x\right]^{n}$$
$$\downarrow$$
$$C_g A_c T_M^{n+1} = C_g A_c T_M^n + \beta\Delta t\left[k_g A_c \frac{-T_M+T_{M-1}}{\Delta x^2}+C_g A_c u\frac{T_{M-1}-T_M}{\Delta x^2} - hP_{g-s}\left(T_M-T_{M,s}\right)\right]^{n+1} \qquad (b.)$$
$$+(1-\beta)\Delta t\left[k_g A_c \frac{-T_M+T_{M-1}}{\Delta x^2}+C_g A_c u\frac{T_{M-1}-T_M}{\Delta x^2} - hP_{g-s}\left(T_M-T_{M,s}\right)\right]^{n}$$
$$\downarrow$$
$$-\frac{\beta\Delta t\left(k_g A_c+C_g A_c u\right)}{\Delta x^2}T_{M-1}^{n+1}+\left[C_g A_c+\beta\Delta t\left(\frac{k_g A_c+C_g A_c u}{\Delta x^2}+hP_{g-s}\right)\right]T_M^{n+1}$$
$$=\beta\Delta t hP_{g-s}T_{M,s}^{n+1}+C_g A_c T_M^n+(1-\beta)\Delta t\left[k_g A_c \frac{-T_M+T_{M-1}}{\Delta x^2}+uC_g A_c \frac{T_{M-1}-T_M}{\Delta x^2}-hP_{g-s}\left(T_M-T_{M,s}\right)\right]^{n}$$

The solid boundary condition, at the inlet is,

$$C_s A_c \frac{T_1^{n+1}-T_1^n}{\Delta t}\Delta x = \beta\left[k_s A_c \frac{T_2-T_1}{\Delta x} + h_r A_c\left(T_{amb}-T_1\right) + hP_{g-s}\left(T_{1,g}-T_1\right)\Delta x + A_s q_{gen}\Delta x\right]^{n+1}$$
$$+(1-\beta)\left[k_s A_c \frac{T_2-T_1}{\Delta x} + h_r A_c\left(T_{amb}-T_1\right) + hP_{g-s}\left(T_{1,g}-T_1\right)\Delta x + A_s q_{gen}\Delta x\right]^{n}$$

$$\downarrow$$

$$C_s A_c T_1^{n+1} = C_s A_c T_1^n + \beta\Delta t\left[k_s A_c \frac{T_2-T_1}{\Delta x^2} + h_r A_c\left(T_{amb}-T_1\right) + hP_{g-s}\left(T_{1,g}-T_1\right) + A_s q_{gen}\right]^{n+1}$$
$$+(1-\beta)\Delta t\left[k_s A_c \frac{T_2-T_1}{\Delta x^2} + h_r A_c\left(T_{amb}-T_1\right) + hP_{g-s}\left(T_{1,g}-T_1\right) + A_s q_{gen}\right]^{n} \qquad \text{(c.)}$$

$$\downarrow$$

$$-\frac{\beta\Delta t k_s A_c}{\Delta x^2}T_2^{n+1} + \left[C_s A_c + \beta\Delta t\left(\frac{k_s A_c}{\Delta x^2} + \frac{h_r A_c}{\Delta x} + hP_{g-s}\right)\right]T_1^{n+1}$$
$$= \beta\Delta t\left(hP_{g-s}T_{1,g}^{n+1} + A_s q_{gen}^{n+1}\right) + C_s A_c T_1^n +$$
$$(1-\beta)\Delta t\left[k_s A_c \frac{T_2-T_1}{\Delta x^2} + h_r \frac{A_c}{\Delta x}\left(T_{1,g}-T_1\right) + hP_{g-s}\left(T_{1,g}-T_1\right) + A_s q_{gen}\right]^{n}$$

and at the exit,

$$C_s A_c \frac{T_M^{n+1}-T_M^n}{\Delta t}\Delta x = \beta\left[k_s A_c \frac{T_{M-1}-T_M}{\Delta x} + h_r A_c\left(T_{amb}-T_M\right) + hP_{g-s}\left(T_{M,g}-T_M\right)\Delta x + A_s q_{gen}\Delta x\right]^{n+1}$$
$$+(1-\beta)\left[k_s A_c \frac{T_{M-1}-T_M}{\Delta x} + h_r A_c\left(T_{amb}-T_M\right) + hP_{g-s}\left(T_{M,g}-T_M\right)\Delta x + A_s q_{gen}\Delta x\right]^{n}$$

$$\downarrow$$

$$C_s A_c T_M^{n+1} = C_s A_c T_M^n + \beta\Delta t\left[k_s A_c \frac{T_{M-1}-T_M}{\Delta x^2} + \frac{h_r A_c}{\Delta x}\left(T_{amb}-T_M\right) + hP_{g-s}\left(T_{M,g}-T_M\right) + A_s q_{gen}\right]^{n+1}$$
$$+(1-\beta)\Delta t\left[k_s A_c \frac{T_{M-1}-T_M}{\Delta x^2} + \frac{h_r A_c}{\Delta x}\left(T_{amb}-T_M\right) + hP_{g-s}\left(T_{M,g}-T_M\right) + A_s q_{gen}\right]^{n} \qquad \text{(d.)}$$

$$\downarrow$$

$$-\frac{\beta\Delta t k_s A_c}{\Delta x^2}T_{M-1}^{n+1} + \left[C_s A_c + \beta\Delta t\left(\frac{k_s A_c}{\Delta x^2} + h_r \frac{A_c}{\Delta x} + hP_{g-s}\right)\right]T_M^{n+1}$$
$$= \beta\Delta t\left(h_r \frac{A_c}{\Delta x}T_{amb} + hP_{g-s}T_{M,g}^{n+1} + A_s q_{gen}^{n+1}\right) + C_s A_c T_M^n +$$
$$(1-\beta)\Delta t\left[k_s A_c \frac{T_{M-1}-T_M}{\Delta x^2} + h_r \frac{A_c}{\Delta x}\left(T_{amb}-T_M\right) + hP_{g-s}\left(T_{M,g}-T_M\right) + A_s q_{gen}\right]^{n}$$

In matrix form, the equations 4.26 through 4.28 can be rewritten as:

$$gas: \quad [\mathbf{C}_1]\mathbf{T}_g^{n+1} = \mathbf{r}_g \qquad solid: \quad [\mathbf{C}_2]\mathbf{T}_s^{n+1} = \mathbf{r}_s$$

where $\mathbf{C}_1$ and $\mathbf{C}_2$ are the *M x M* coefficient matrices, $\mathbf{T}_g$ and $\mathbf{T}_s$, are the unknown *M x 1* temperature vectors and $\mathbf{r}_g$ and $\mathbf{r}_s$ are the right hand side vectors. The coefficient matrices are tri-diagonal and following the technique prescribed by Press [110]. The matrix can be described by three *M x 1* vectors, **a**, **b**, and **c**. The below-diagonal terms are read into a vector, **a**, the diagonal is **b**, and the above-diagonal is **c**. For $\mathbf{C}_1$ these three vectors are defined as,

$$\begin{aligned}
&a_1 = empty; \qquad b_1 = C_g A_c + \beta\Delta t\left(\frac{3k_g A_c + C_g A_c u\Delta x}{\Delta x^2} + hP_{g-s}\right); \quad c_1 = -\frac{\beta\Delta t k_g A_c}{\Delta x^2};\\
&a_2 = -\frac{\beta\Delta t\left(k_g A_c + C_g A_c u\Delta x\right)}{\Delta x^2}; \quad b_2 = C_g A_c + \beta\Delta t\left(\frac{2k_g A_c + C_g A_c u\Delta x}{\Delta x^2} + hP_{g-s}\right); \quad c_2 = -\frac{\beta\Delta t k_g A_c}{\Delta x^2};\\
&\ldots\\
&a_M = -\frac{\beta\Delta t\left(k_g A_c + C_g A_c u\Delta x\right)}{\Delta x^2}; \quad b_M = C_g A_c + \beta\Delta t\left(\frac{k_g A_c + C_g A_c u\Delta x}{\Delta x^2} + hP_{g-s}\right); \quad c_M = empty;
\end{aligned} \tag{4.29}$$

and the entire right hand side of the gas equation is expressed as the vector, $\mathbf{r}_g$,

$$
\begin{aligned}
r_1 &= \frac{\beta\Delta t\left(2k_g A_c + C_g A_c u\Delta x\right)}{\Delta x^2} T_{g,inlet} + \beta\Delta t h P_{g-s} T_{1,s}^{n+1} + C_g A_c T_1^n \\
&\quad + (1-\beta)\Delta t\left[k_g A_c \frac{T_2 - 3T_1 + 2T_{g,inlet}}{\Delta x^2} + C_g A_c u \frac{T_{g,inlet} - T_1}{\Delta x} - hP_{g-s}\left(T_1 - T_{1,s}\right)\right]^n \\
r_2 &= \beta\Delta t h P_{g-s} T_{i,s}^{n+1} + C_g A_c T_i^n + (1-\beta)\Delta t\left[k_g A_c \frac{T_{i+1} - 2T_i + T_{i-1}}{\Delta x^2} + C_g A_c u \frac{T_{i-1} - T_i}{\Delta x} - hP_{g-s}\left(T_i - T_{i,s}\right)\right]^n \\
&\ldots \\
r_M &= \beta\Delta t h P_{g-s} T_{M,s}^{n+1} + C_g A_c T_M^n + (1-\beta)\Delta t\left[k_g A_c \frac{-T_M + T_{M-1}}{\Delta x^2} + uC_g A_c \frac{T_{M-1} - T_M}{\Delta x} - hP_{g-s}\left(T_M - T_{M,s}\right)\right]^n
\end{aligned}
\tag{4.30}
$$

For the solid equation, $\mathbf{C}_2$ is composed of,

$$
\begin{aligned}
&a_1 = empty; \qquad b_1 = C_s A_c + \beta\Delta t\left(\frac{k_s A_c}{\Delta x^2} + h_r \frac{A_c}{\Delta x} + hP_{g-s}\right); \quad c_1 = -\frac{\beta\Delta t k_s A_c}{\Delta x^2}; \\
&a_2 = -\frac{\beta\Delta t k_s A_c}{\Delta x^2}; \quad b_2 = C_s A_c + \beta\Delta t\left(\frac{2k_s A_c}{\Delta x^2} + hP_{g-s}\right); \quad c_2 = -\frac{\beta\Delta t k_s A_c}{\Delta x^2}; \\
&\ldots \\
&a_M = -\frac{\beta\Delta t k_s A_c}{\Delta x^2}; \quad b_M = C_s A_c + \beta\Delta t\left(\frac{k_s A_c}{\Delta x^2} + h_r \frac{A_c}{\Delta x} + hP_{g-s}\right); \quad c_M = empty;
\end{aligned}
\tag{4.31}
$$

and the entire right hand side of the solid equation is expressed as the vector, $\mathbf{r}_s$,

$$
\begin{aligned}
r_1 &= \beta\Delta t\left(hP_{g-s} T_{1,g}^{n+1} + A_s q_{gen}^{n+1}\right) + C_s A_c T_1^n + \\
&(1-\beta)\Delta t\left[k_s A_c \frac{T_2 - T_1}{\Delta x^2} + h_r \frac{A_c}{\Delta x}\left(T_{amb} - T_1\right) + hP_{g-s}\left(T_{1,g} - T_1\right) + A_s q_{gen}\right]^n \\
r_2 &= \beta\Delta t\left(hP_{g-s} T_{i,g}^{n+1} + A_s q_{gen}^{n+1}\right) + C_s A_c T_i^n + \\
&(1-\beta)\Delta t\left[k_s A_c \frac{T_{i+1} - 2T_i + T_{i-1}}{\Delta x^2} + hP_{g-s}\left(T_{i,g} - T_i\right) + A_s q_{gen}\right]^n \\
&\ldots \\
r_M &= \beta\Delta t\left(hP_{g-s} T_{M,g}^{n+1} + A_s q_{gen}^{n+1}\right) + C_s A_c T_M^n + \\
&(1-\beta)\Delta t\left[k_s A_c \frac{T_{M-1} - T_M}{\Delta x^2} + h_r \frac{A_c}{\Delta x}\left(T_{amb} - T_M\right) + hP_{g-s}\left(T_{M,g} - T_M\right) + A_s q_{gen}\right]^n
\end{aligned}
\tag{4.32}
$$

The discretized equations use the following definitions for effective volumetric heat capacity and effective thermal conductivity:

$$C_g = \frac{\left(\rho c_p A\right)_g}{A_c}; \qquad C_s = \frac{\sum_i \left(\rho c_p A\right)_i}{A_c}; \qquad k_s = \frac{\sum_i \left(kA\right)_i}{A_c}; \qquad k_g = \frac{\left(kA\right)_g}{A_c}$$

The temperature-dependent thermophysical properties for heat capacity, C_g, was developed using NASA/Chemkin Polynomials [111]. The thermal response in the stack is dominated by interconnect material properties. Expressions for the temperature dependent thermophysical properties of SS441 were provided by a SigmaPlot™ curve fit of empirically resolved data at NETL-Albany [104-106]. The thermophysical properties of the P-E-N material were taken from Aguiar [5]. The heat generation (q_{gen}) term from the operating fuel cell is provided in Equation 4.33.

$$q_{gen} = HG_{cell} \tag{4.33(a.)}$$

$$HG_{cell} = i\left(\frac{-\Delta H_{H_2OFormation}}{2F} - V\right) \tag{b.}$$

The heat generation term, q_{gen}, is heat generated from cell operation, HG_{cell}.

4.4 Model Verification

Since SOFC technology is still in a developmental phase, there exists minimal empirical data for validation studies, yet a means to verify the results obtained by the model had to be resolved to substantiate utilization for this investigative study. To that end, comparisons with

the IEA benchmark [103] is presented. The conditions for the IEA benchmark comparisons are presented below in Table 4.7.

Table 4.6. IEA benchmark parameters.

Geometry	
Anode Thickness	0.05 mm
Cathode Thickness	0.05 mm
Electrolyte Thickness	0.15 mm
Interconnect Thickness	2.50 mm
Rib Width	2.42 mm
Cell Length	100 mm
Cell Width	100 mm
Operating Conditions	
System Pressure	1 bar
Inlet Temperature	1173 K
Air Ratio	7
Fuel Utilization	85%
Mean Current Density	3000 A/m^2

The IEA provides benchmarking data for a humidified hydrogen mixture (90% H_2, 10% H_2O). The comparison results from the humidified hydrogen simulation are presented in Table 4.8. The results compare reasonably well with the IEA benchmarking data. The cell potential is within range of the IEA benchmark data. The maximum current density and maximum temperature results are within 6% of the IEA bench mark data. The conservative temperature results are due to the radiation heat transfer. When radiation to the surrounding is not considered, the temperature results are within IEA benchmark data as shown in Table 4.8. The maximum current results are still within 6% of the IEA data. The discrepancy in the maximum current

density data is probably due to the higher fidelity polarization relationships employed by the model.

Table 4.7. IEA benchmark comparison - humidified hydrogen.

Parameter	Benchmark Data	1-D Model Results	1-D Model Results No Rad.
Voltage (V)	0.702-0.722	0.692	0.702
Max Current Density	0.373-0.396	0.409	0.444
Max PEN Temp (°C)	1049-1098	1024	1061
Outlet Air Temp (°C)	1048-1067	1023	1060

4.5 Sample Results

To ascertain a basis for comparison for the optimization study and to offer a view of sample results of the model, the baseline geometry of IAR of 1, DGCW of 0.25, and SR of 24 was simulated. Due to thermal considerations of operation, SOFCs do not operate at their maximum power density. Typically, SOFCs are operated at intermediate values to prevent inducing large thermal stresses on the materials, as well as to pursue larger operational efficiencies. In view of this, the performance at 0.4 A/cm^{2}was characterized. Other operating parameters include a NOS of 7, inlet oxidant temperature of 600C, and fuel utilization of 85%. Table 4.9 shows key performance values for the baseline design. For the optimization study, 2nd law efficiency is a key parameter, the baseline design had a 2nd law efficiency of 91.5%. For a SOFC, 2nd law efficiencies are typically in this range (*i.e.,* 60-93%) as was reported in the Literature Review chapter. The other key parameter that is tracked is maximum thermal gradients. The baseline design had a maximum thermal gradient of 750 °C/m. According to Nakajo's work [2], a thermal gradient below 1000 °C/m results in a SOFC with a sufficiently low probability of thermo-

mechanical failure (*i.e.,* 10^{-4}). The baseline design is below this threshold; which is not taken to be universal, but is used as a point of comparison. In addition to performance parameters, Reynolds number and Nusselt number are reported in Table 4.10.

Table 4.8. Key performance parameters of baseline design.

Current Density (A/cm^2)	Maximum Thermal Gradient (°C/m)	2nd Law Efficiency (%)	1st Law Efficiency (%)	Power Density (mW/cm^2)
0.4	750.2	91.5	51.2	299.0

Table 4.9. Dimensionless parameters of baseline design.

Current Density (A/cm^2)	Reynolds Number	Avg. Nusselt Number
0.4	104.7	3.11

A key point of inspection is to examine the temperature and thermal gradient profiles of the solid domain. Selection of the thermal boundary conditions has a great impact on such profiles. Figures 4.6 and 4.7 show the temperature profile and absolute thermal gradients, respectively. Due to the heat generated by the electrochemical reactions and the convective and radiation boundary conditions, the temperature reaches an intermediate maximum. The location of the maximum is impacted by the thermal conductance, flow condition, and Nusselt number. The thermal conductance, which is the product of the solid thermal conductivity and cross-sectional area, offers a measure of rate of thermal energy conduction. Smaller thermal conductance will cause the location of the maximum to be further downstream as long as the flow remains laminar. Given the flow condition is laminar, the associated fully developed Nusselt number is relatively small (3.11). Smaller Nusselt numbers allow for less heat to be convected. This in turn causes more heat to escape via the boundary conditions. Given ambient

temperature for the inlet and exit are the same, then the location of the maximum temperature will be driven by the thermal conductance. The location of the maximum temperature also marks the point at which the thermal gradient is zero which is shown in Figure 4.6. The location of the maximum thermal gradient occurs within the first 20% of the axial length. Based upon the boundary conditions, co-flow arrangement, and laminar flow condition, the maximum thermal gradient will occur near the inlet. Given the co-flow arrangement, the maximum amount of heat convection will occur in the inlet region because of the fixed oxidant temperature boundary condition. Heat convection will decrease as the oxidant temperature approaches the solid temperature. Given the laminar condition and thermally developing flow, the changes in the solid temperature will change most rapidly in the inlet region. Therefore, the maximum thermal gradient is expected to be in the inlet region. While location of the maximum thermal gradient is important, the present dissertation is concerned with the magnitude of the thermal gradient. As dimensionless geometric parameters change over the optimization, the heat generated and thermal conductance changes. This will impact maximum thermal gradients. The optimization study, discussed in the next chapter, will show how maximum thermal gradients impact design of planar SOFC.

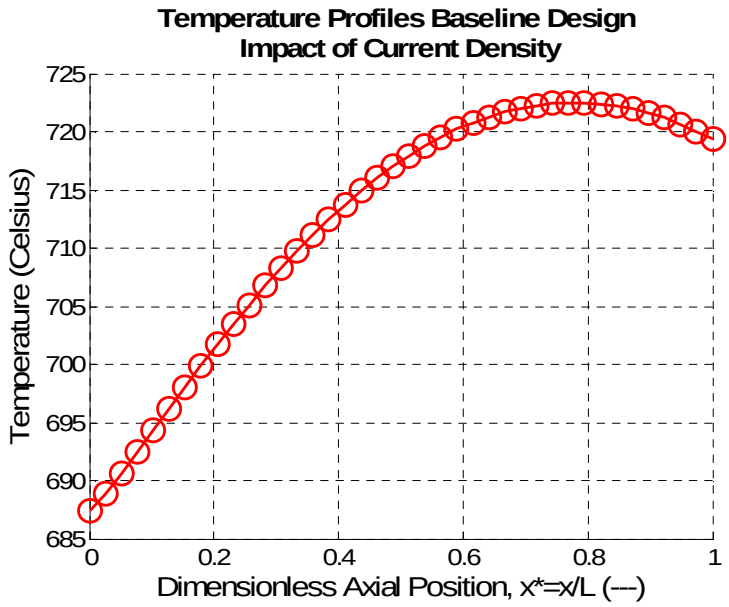

Figure 4.8. Temperature profile of baseline design.

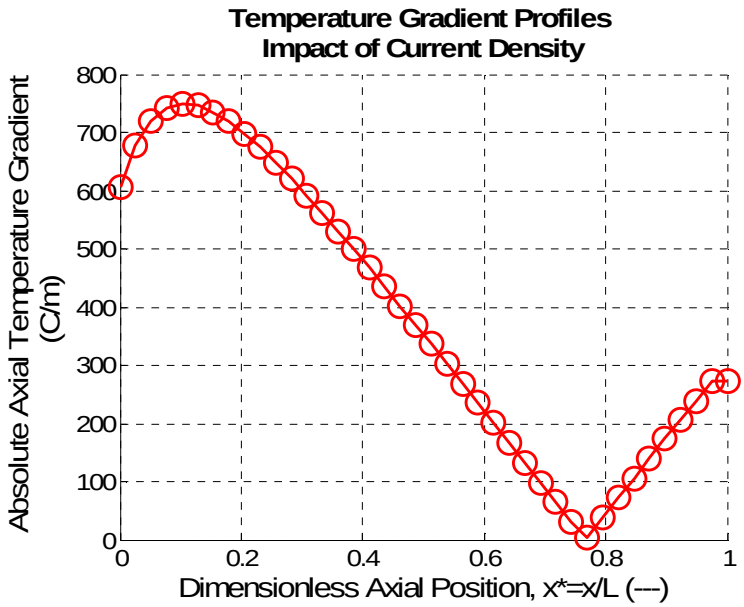

Figure 4.9. Temperature gradient profiles for baseline design.

4.6 Dimensionless Parameter Performance Analysis

Before proceeding to the optimization study, a performance analysis of the dimensionless parameters must be conducted. This allows for down selection of the ranges of

the dimensionless geometric terms. For the performance study, conventional operating conditions were chosen. Table 4.10 details the operating conditions. The inlet fuel stream composition to the anode was humidified hydrogen (*i.e.,* 90% H2 and 10% H2O). The inlet oxidant stream composition to the cathode was air (*i.e.,* 79% N2 and 21% O2). The fuel utilization, which is the percentage of fuel consumed during the electrochemical reactions, was 85%. The inverse oxidant utilization or NOS (Number-of-Stoichs) was 7. A NOS value of 7 means that 7 times the needed amount of oxidant was supplied to the cell. The extra oxidant is used to provide cooling to the cell. The impact of each dimensionless parameter on cell performance and thermal gradients is reported in Tables 4.11-4.14. A brief discussion of how IAR, DGCW, SR, and EER impact the performance of a SOFC and the refinement of the bounds of the dimensionless parameters for the optimization follows.

Table 4.10. Operating parameters for performance analysis.

Operating Parameters	Value
NOS	7
Fuel Utilization	0.85
Current Density	0.6 A/cm^2
Inlet Oxidant Temp.	873K

Table 4.11 notes the impact of IAR on performance and maximum thermal gradients in the cell. As IAR increases, cell performance and maximum thermal gradient increases. There is 284% increase in power density between IAR of 0.2 and 2, whereas, there is only a 1.0% increase between IAR of 2 and 5. The reason for the increasing power density with IAR is due to the effect of decreasing ohmic losses. The decrease in ohmic losses is due to the decrease in the height of the interconnect. Thermal gradients increased by 355% from IAR of 0.2 and 5. Based

upon cell performance, the IAR range used for the optimization will be reduced to between 0.2 and 2.

Table 4.11. The impact of IAR on performance and maximum thermal gradients with DGCW of 0.5, SR of 25, EER of 50.

IAR	2nd Law Efficiency	Power Density (mW/cm^2)	1st Law Efficiency	Maximum Thermal Gradient (°C/m)
0.2	42.9%	110.6	12.6%	410
0.5	80.4%	330.7	37.7%	595
1	86.8%	396.9	45.2%	800
2	89.1%	423.5	48.2%	1252
5	89.5%	427.9	48.7%	1862

Table 4.12 notes the impact of DGCW on performance and maximum thermal gradients in the cell. As DGCW increases, cell performance decreases and maximum thermal gradient decreases. Power density decreased by 35% between DGCW of 0.1 and 0.75. Thermal gradients decreased by 50.2%. The decrease in power density as DGCW decreases is due to the increase in ohmic losses. Ohmic losses increase with DGCW due to increased resistance in the interconnect. Note, the interconnect resistance is calculated utilizing an equivalent circuit model. Increase in DGCW causes an increase in constriction resistance. Above DGCW of 0.85, the cell cannot produce power. Based upon cell performance and consideration for pressure drop effects, the DGCW range used for the optimization will be reduced to 0.25.

Table 4.12. The impact of DGCW on performance and maximum thermal gradients with IAR of 1, SR of 25, and EER of 50.

DGCW	2nd law Efficiency	Power Density mW/cm^2	1st Law Efficiency	Max. Thermal Gradient (°C/m)
0.1	91.2%	442.7	50.4%	1610
0.25	90.6%	436.0	49.7%	1188
0.5	86.8%	396.9	45.2%	804
0.75	74.3%	286.1	32.6%	801

Table 4.13 notes the impact of EER on performance and maximum thermal gradients in the cell. EER marginally impacts performance and thermal gradients. Power density only changes by 1% as EER varies. This change is from the concentration losses changing. Despite concentration losses differing by as much as 400%, concentration losses are an order of magnitude smaller than activation and ohmic losses. The concentration loss of EER of 100 is as much as 5 times as large as that of EER of 10. This increase is due to the thicker anode. Concentration losses are directly proportional to thickness of the electrodes. However, the lower limit thickness of the anode is limited by mechanical reliability. Based upon cell performance, the EER range used for the optimization will be reduced to 0.5.

Table 4.13. The impact of EER on performance and maximum thermal gradients with DGCW of 0.50, IAR of 1, and SR of 25.

EER	2nd Law Efficiency	Power Density (mW/cm^2)	1st Law Efficiency	Max. Thermal Gradient (°C/m)
10	86.9%	399.2	45.5%	742
30	86.9%	398.0	45.3%	742
50	86.8%	396.9	45.2%	742
75	86.7%	395.5	45.1%	742
100	86.6%	394.1	44.9%	742

Table 4.14 notes the impact of SR on performance and maximum thermal gradients in the cell. The 2nd law efficiency, power density, fuel cell efficiency, and maximum thermal gradient increase as SR increases. Power density increased by 192%. The fundamental reason behind the performance enhancements is due to the reduction in ohmic resistance. Thermal gradients increased by 11 fold. Thermal gradients increase because the cross-sectional area decreases as SR increases which allows for less area for the heat to conduct through the solid. Based upon cell performance and the significant impact on thermal gradients, the range of SR values will encompass 5 to 100.

Table 4.14. The impact of SR on performance and maximum thermal gradients.

SR	Efficiency 2nd Law	Power Density (mW/cm^2)	Efficiency 1st Law	Max. Thermal Gradient (°C/m)
5	40.0%	104.0	11.5%	120
10	66.1%	212.1	36.2%	210
25	80.1%	272.9	46.6%	514
50	85.2%	294.5	50.3%	953
75	89.9%	301.3	51.5%	1301
100	94.6%	304.2	52.0%	1488

5 OPTIMIZATION RESULTS AND DISCUSSION

The optimization results chapter will first discuss the baseline design. Second, the optimization study will be presented and analyzed. Lastly, conclusions are drawn inclusive of design recommendations inferred by the optimization.

5.1 Baseline Design Characterization

The optimization problem seeks to maximize 2nd law efficiency by minimizing total entropy generation. By minimizing total entropy generation, exergy destruction is minimized. The exergy destruction term in the denominator is the key term in Equation 5.1. 1st and 2nd law performance parameters are tracked in the optimization. Equation 5.2 describes 1st law efficiency for a fuel cell. As was detailed in the Literature Review chapter, exergetic efficiency is the preferred metric of performance. Table 5.1 shows key performance parameters for the baseline design. The baseline design has 1st law and 2nd law efficiencies of 52.6% and 91.5%, respectively. The 2nd law efficiency of the baseline design is comparable to the range of values observed by authors in the literature. As an example, Calise [36] reported 2nd law efficiencies in the range of 77%-93%.

$$\varepsilon_{II} = \frac{P_{cell}}{P_{cell}+E_{destruction}} \tag{5.1}$$

$$P_{cell} = iV \tag{b.}$$

$$E_{destruction} = T_o \dot{S}_{gen} \tag{c.}$$

$$\varepsilon_I = \frac{P_{cell}}{\dot{n}_{fuel} LHV_{fuel}} \tag{5.2}$$

In Equation 5.1, P_{cell} is the power produced by the entire cell, *i* is the current generated by the fuel cell, V is the cell potential, and $\dot{S}_{gen}$ is the entropy generation. In Equation 5.2, LHV_{fuel} is the lower heating value of the fuel, and $\dot{n}_{fuel}$ is the molar flow rate of the fuel.

In order to understand the results of the thermodynamic optimization, analysis of the sources of entropy generation and their relationships to the dimensionless geometric parameters is necessary. Equation 3.3 from Chapter 3 is shown below which describes the sources of entropy generation.

$$g_p = g_{tf} + g_h + g_{ohm} + g_{act} + g_{conc} \quad \text{(3.3(a.))}$$

$$g_{tf} = \frac{q_{conv} \cdot \Delta T_{sg}}{V_{slice} \cdot T_g^2 (1 + \Delta T_{sg}/T_g)} + \frac{\dot{m}}{\rho \cdot T_g} \frac{\Delta P}{V_{slice}} \quad \text{(b.)}$$

$$g_h = \frac{1}{T_s^2} \left(q_{cond} \cdot \frac{\Delta T_s}{\Delta x} \right) \frac{\mathbf{1}}{A_{,slice}} \quad \text{(c.)}$$

$$g_{ohm} = \frac{1}{T_s} (\eta_{ohm} \cdot i_{cv}) \frac{\mathbf{1}}{V_{slice}} \quad \text{(d.)}$$

$$g_{act} = \frac{1}{T_s} (\eta_{act} \cdot i_{cv}) \frac{\mathbf{1}}{V_{slice}} \quad \text{(e.)}$$

$$g_{conc} = \frac{1}{T_s} (\eta_{conc} \cdot i_{cv}) \frac{\mathbf{1}}{V_{slice}} \quad \text{(f.)}$$

In Equation 3.3, $\dot{m}$ is the mass flow rate of the oxidant, q_{conv} is the local convective heat transfer rate within a unit cell, ρ is density of the oxidant , c_p is the constant pressure specific heat of the oxidant,ΔT_{sg} is temperature difference between the solid and gas, V_{slice} is the volume of a section or "slice" of the descritized control volume, A_{slice} is the cross-sectional area of a section or "slice" of the descritized control volume, η_{ohm} is the ohmic overpotential, η_{act} is the activation overpotential, η_{conc} is the concentration overpotential, and i_{cv} is the current within the given volume (*i.e.,* A). As per the entropy generation terms, g_{tf} is the

entropy generation due to thermal-fluidic losses in the gas channel, and g_h accounts for irreversibilities due to conduction heat transfer. Finally, g_{ohm} quantifies the ohmic irreversibilities, g_{act} represents the activation irrversibilities, and g_{conc} represents the concentration losses. Note, g_p is related to total entropy generated as defined in Equation 5.3.

$$\dot{S}_{gen} = \int g_p \, dV \tag{5.3}$$

To ascertain a basis for comparison for the optimization study, the baseline geometry of IAR of 1, DGCW of 0.25, and SR of 24 was simulated and previously reported in Chapter 4. The results are only shown. Further explanation was given in Chapter 4. The performance at 0.4 A/cm^2 was characterized and used throughout the optimization Table 5.1 shows key performance values for the baseline design. In addition to performance parameters, dimensionless parameters of Biot number, Reynolds number, and Nusselt number are reported in Table 5.2. The Biot number is especially important given the assumption of cross-sectional thermal gradients being negligible. The baseline design has a Biot number 0.0596 and 0.0196, in the P-E-N and solid length, respectively. This is well below 0.1 indicating cross-sectional thermal gradients are not significant. The Reynolds number is 104.7 indicating laminar flow.

Table 5.1. Key performance parameters of baseline design.

Current Density (A/cm^2)	Maximum Thermal Gradient (°C/m)	2nd Law Efficiency (%)	1st Law Efficiency (%)	Power Density (mW/cm^2)
0.4	750.2	91.5	52.6	299.0

Table 5.2. Dimensionless parameters of baseline design.

Current Density (A/cm^2)	Biot Number (PEN, Solid)		Reynolds Number	Avg. Nusselt Number
0.4	0.0596	0.0196	104.7	3.11

Figures 5.1 and 5.2 show the temperature and absolute thermal gradient profiles, respectively. Again, explanations of trends are reported in Chapter 4. Figures are shown for the benefit of the reader and for comparison to the optimized results.

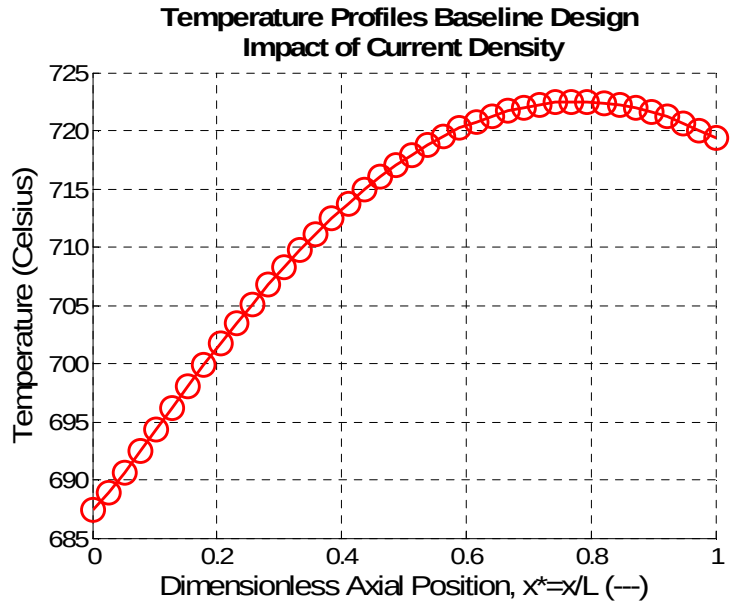

Figure 5.1. Temperature profile of baseline design.

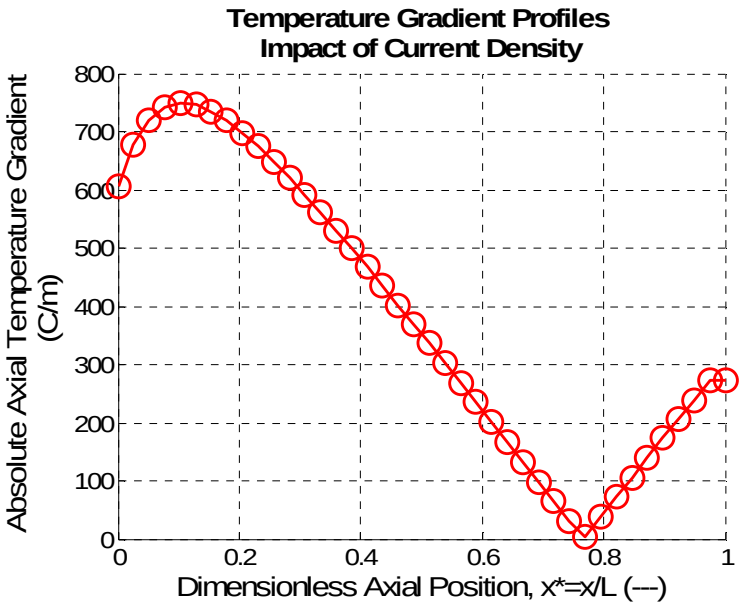

Figure 5.2. Temperature gradient profiles for baseline design.

5.2 Surface Response of Optimization

For the entire optimization domain (*i.e.,* span of dimensionless geometric parameters), the metrics of performance and thermal gradients are reported. IAR, internal aspect ratio, was varied from 0.25 to 2 in increments of 0.25. SR, slenderness ratio, was varied from 4 to 100 in increments of 2. DGCW, dimensionless gas channel width, was fixed at 0.25. And, EER, electrode to electrolyte ratio, was fixed at 0.50. There were 392 designs investigated.

Traditional design methodologies of SOFCs call for maximizing 1st law metrics of fuel cell efficiency and power density without consideration of thermal gradients. The key distinguishing characteristic of the present dissertation is the consideration of thermal gradients in maximizing performance metrics. Figures 5.3-5.5 shows entire solution space for exergetic efficiency, power density, and fuel cell efficiency, respectively. In only considering performance metrics, the design choice would be to find the design that produced the highest performance metric without considering the maximum thermal gradients. Based upon Figures 5.3-5.5, designs with high IAR values of 1.25 or larger and intermediate or larger SR values (e.g., 36 or greater) are where high performance metrics occur. However, as shown in Figure 5.6, maximum thermal gradients increase with IAR and SR. Therefore, in considering maximum allowable thermal gradient for a particular design, the selection of IAR and SR is critical. The optimal design is then determined by the maximum tolerable thermal gradient. Secondarily, given the small hydraulic diameters, the amount of pressure drop across the oxidant channel must be considered. Given SOFCs are part of a system, noting the pressure drop across the cell

is important from a systems point of view. Figure 5.7 shows how pressure drop increases as IAR and SR increase. Pressure drop is calculated using the expression given in Equation 5.4. Note that the friction factor is calculated using a spline interpolation of the values shown in Table 5.4. The values in Table 5.4 are for rectangular passageways and are taken from Kays' [112] work. In investigating Equation 5.4, the smaller hydraulic diameters lead to larger pressure drops. As IAR and SR increase, hydraulic diameter decreases. A fuel cell designer may limit pressure drop to 5% of total pressure, as an example, thereby eliminating high IAR and SR values. Next, insights and descriptive statistics are given to explain the shapes of the solution surfaces.

$$P_{drop} = \frac{c_f \rho_g u^2 L_c}{2D_h} \tag{5.4(a.)}$$

$$c_f = \frac{f(IAR)}{Re} \tag{b.}$$

Table 5.3. Values used to compute spline interpolation of friction factor.

IAR or 1/IAR	0.1	0.2	0.3	0.4	0.5	0.6	0.7	0.8	0.9	1
c_f	21.2	19	17.6	16.5	15.7	15	14.7	14.4	14.3	14.2

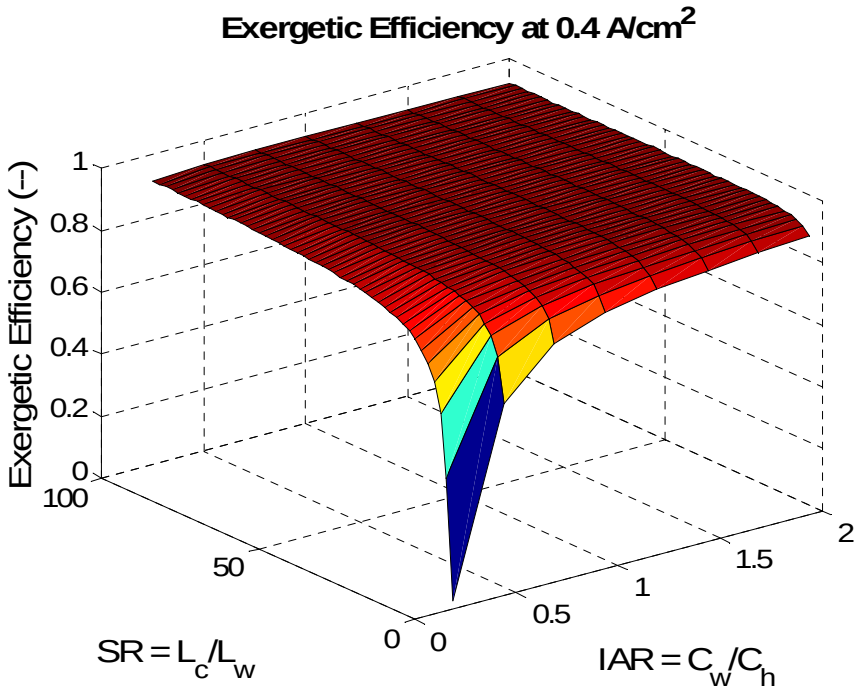

Figure 5.3. Exergetic efficiency for the entire optimization space at 0.4 A/cm^2.

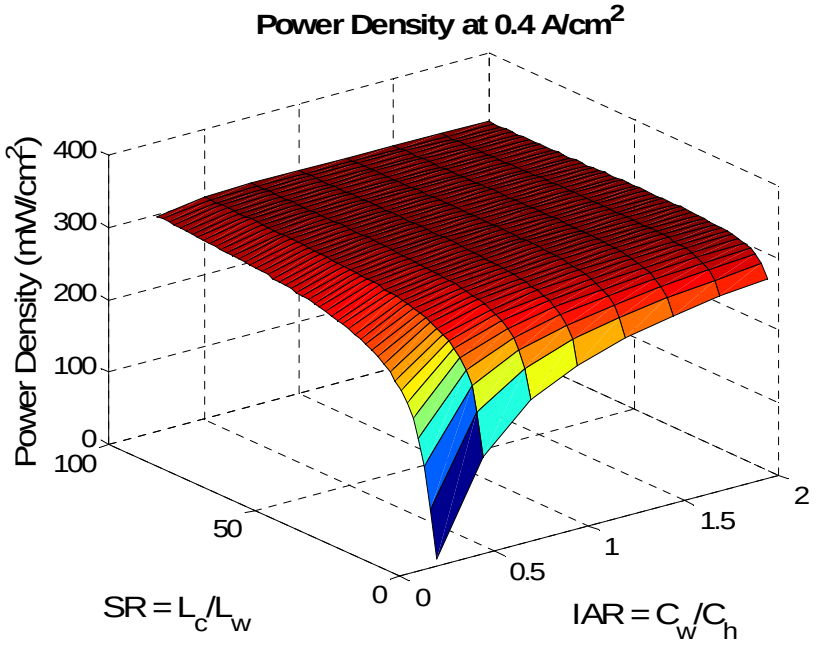

Figure 5.4. Power density for the entire optimization space at 0.4 A/cm^2.

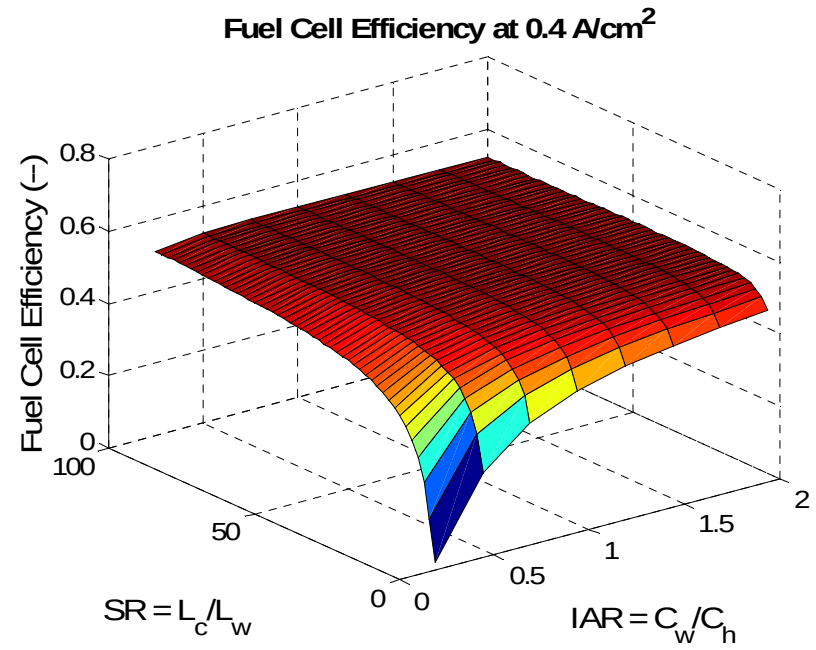

Figure 5.5. Fuel cell efficiency for the entire optimization space at 0.4 A/cm^2.

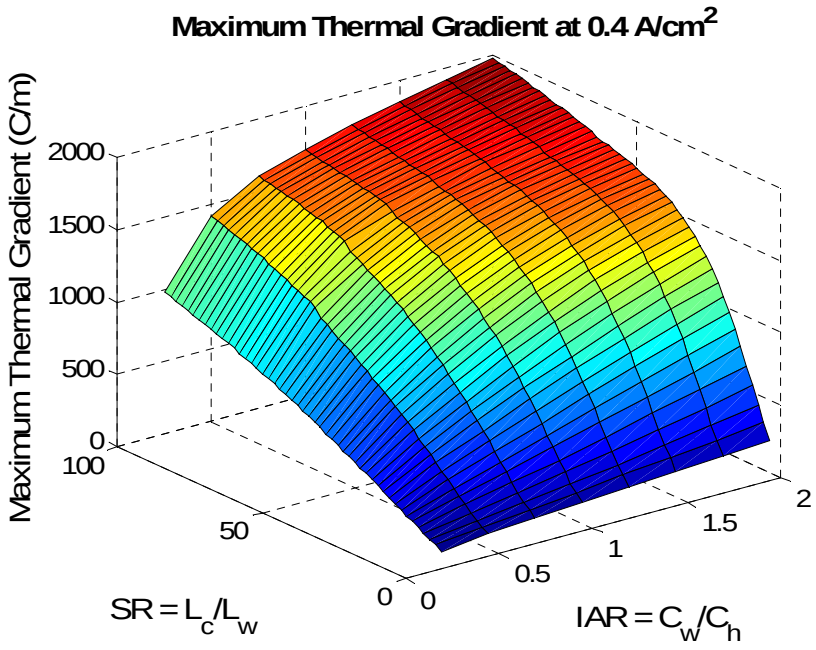

Figure 5.6. Maximum temperature gradient for the entire optimization space at 0.4 A/cm^2.

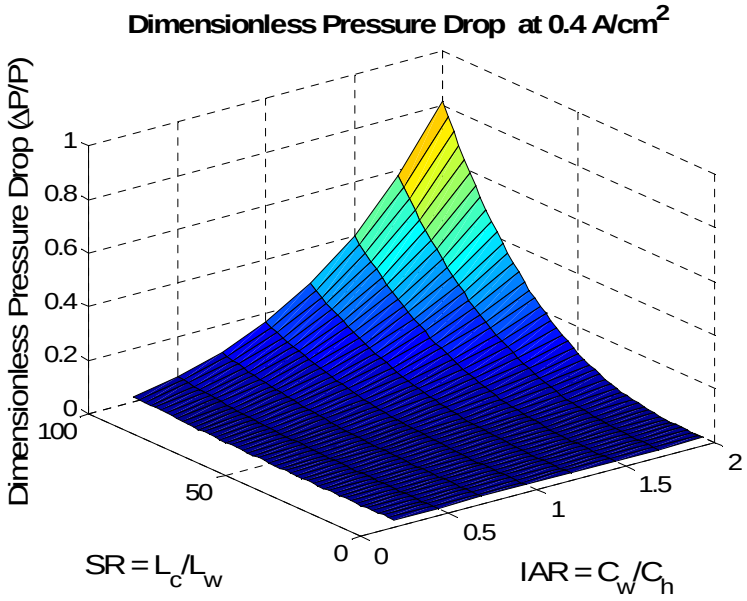

Figure 5.7. Dimensionless pressure drop for entire optimization space at 0.4 A/cm^2.

Common to all surface plots shown in Figures 5.3-5.5, performance asymptotically improves as IAR and SR increase. The surface plots of exergetic efficiency, power density, and fuel cell efficiency sharply increase between SR of 4 to 20 and IAR 0.25 to 1. The performance values are closely coupled as indicated by the standard deviation of the performance metrics which are reported in Table 5.4. 2nd law efficiency had a mean of 90.6% with a standard deviation of 6.58%. 1st law efficiency had a mean of 50.3% and standard deviation of 5.41%. Power density had a mean value of 294.6 mW/cm^2 with a standard deviation of 31.6 mW/cm^2. Further indication of the relative "flatness" of the surface plots of the performance parameters is the close proximity of the median and maximum values. 2nd law efficiency has a maximum of 92.8% and a median value of 92.5%. Maximum fuel cell efficiency is 52.9% with the median being 52.4%. The maximum power density value is 309.3 mW/cm^2 with a median value of 306.6

mW/cm^2. Given the proximity of median and maximum values for each performance parameter, greater emphasis on maximum allowable thermal gradients can be placed.

Table 5.4. Statistics of optimization at 0.4 A/cm^2.

Statistic	2^{nd} Law Efficiency (%)	1^{st} Law Efficiency (%)	Power Density (mW/cm^2)
Mean	90.6	50.3	294.6
Median	92.5	52.4	306.6
Max	92.8	52.9	309.3
Min	0.095	0.0180	0.105
Standard Deviation	6.58	5.41	31.6

Insights on the performance metrics surfaces plots are now presented. Figure 5.5 shows surface plot of 2^{nd} law efficiency against the span of IAR and SR values. As IAR and SR increase, 2^{nd} law efficiency increases to an intermediate maximum, then marginally declines (*i.e.,* fractions of percentage points). This is due to the total entropy generation shown in Figure 5.8 reaching a minimum at SR of 40, and then marginally increasing beyond SR of 40 for all values of IAR. This trend is due to competing effects of geometric changes and heat transfer effects on each mode of entropy generation. Each mode of entropy generation varies in its dependence on geometry effects and heat transfer effects. Ohmic losses, shown in Figure 5.9, are dominated by geometric effects and therefore decrease as cross-sectional area decreases (*i.e.*, increases in IAR and SR). As cross-sectional area decreases, the effective path length for the current to flow decreases thereby causing a decrease in the resistance. Because current density and electroactive area are fixed, the distribution of current is reallocated to accommodate the geometric changes. This in turn causes the heat generation and temperature profiles to change. Subsequently, the remaining modes of entropy generation, which are more sensitive to thermal effects, experience intermediate maxima and minima. Activation losses, which is a strong

function of temperature, is the dominant mode of entropy generation above SR of 30. Near a SR of 30, ohmic losses are small enough to allow for thermal effects to dominate. Beyond SR of 30, average temperatures are higher and the change in average temperature is significantly smaller as will be shown. In sum, electrochemical losses account for more than 94% of total losses for the entire design space considered. Of the total electrochemical losses, 97% or more is due to activation and ohmic losses (*i.e.,* concentration losses are relatively insignificant). As a result, the small variations is 2nd law efficiency beyond SR of 30 is primarily due to the thermal effects on activation losses. Changes in electrochemical losses also impact cell potential for the current modeling assumptions. Since cell potential is dependent upon electrochemical losses, then changes in cell potential will be reflected in both fuel cell efficiency and power density surface plots as shown in Figures 5.4 and 5.5, respectively.

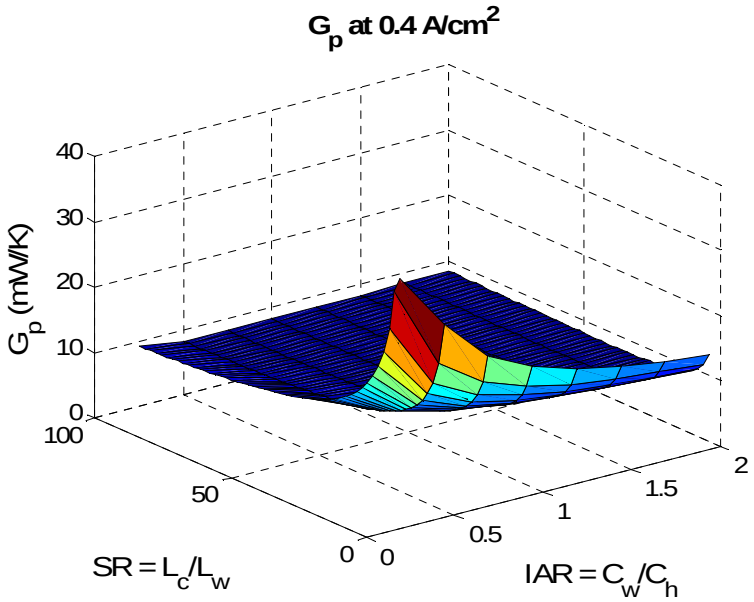

Figure 5.8. Surface plot of total entropy generation.

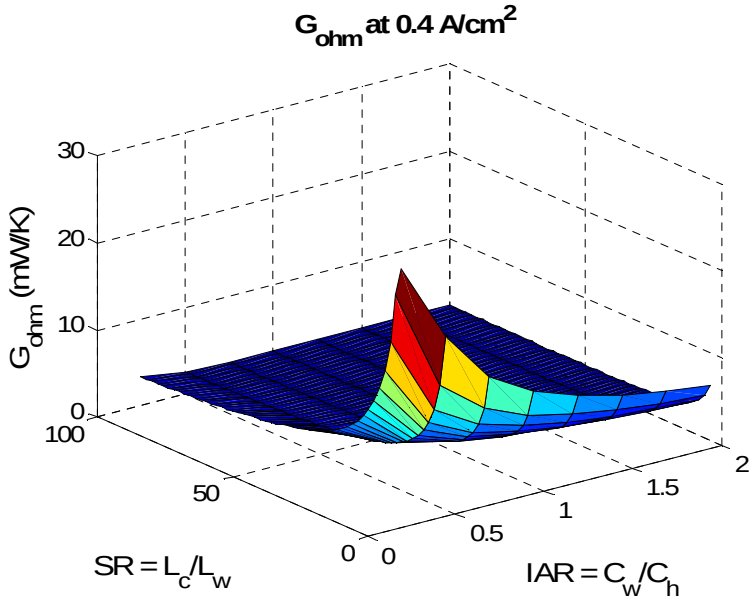

Figure 5.9. Surface plot of ohmic entropy generation at 0.4 A/cm^2.

The interplay of geometric and thermal effects on electrochemical losses is central to performance changes observed. As detailed in the Fuel Cell Modeling Chapter, there are three modes of electrochemical losses in a SOFC: ohmic, activation, and concentration. Ohmic losses are losses that are proportional to the current demanded and resistance of the materials. Ohmic resistance is dependent upon the temperature, resistivity, and geometry of the P-E-N and interconnect materials. Activation losses are related to the electrode kinetics. The electrode kinetics are a function of the temperature and the local current demanded. Therefore, activation losses are indirectly impacted by geometric changes. Concentration or diffusion overpotentials are losses due to the diffusion of reactants through the porous electrodes. Concentration losses are impacted by electrode thickness, temperature, and local current density. Current density impacts concentration losses because it is proportional to the consumption rate of the local reactants via Faraday's law. The present optimization does not

vary electrode thickness as a degree-of-freedom. So, only current density and temperature impact diffusion losses. As previously mentioned, activation losses exceed ohmic losses near a SR of 30, and this is regardless of the domain of IAR values. Increases in IAR lead to a decrease in interconnect height (*i.e.,* interconnect height equals twice the gas channel height). While increases in SR lead to smaller cell width given the fixed cell length of 100 mm. Above SR of 30, the reductions in interconnect width are sufficient enough to cause a direct decrease in ohmic losses with respect to activation losses. The varied geometry of the interconnect changes the path of the flow of electricity thereby impacting resistance. The changes in ohmic losses drive current density and local temperature distributions. Local changes in current and temperature directly impact activation losses. Given the dominance of the interconnect ohmic losses, changes in the internal shape of the interconnect (i.e., gas channel dimensions through the parameter IAR) and the total width of the interconnect through the parameter SR dictate performance metrics. As electricity is being generated by the cell, the resistance of the interconnect and P-E-N must be overcome. The axial distribution of the current being drawn is a function of P-E-N thicknesses and interconnect geometry. Given the current density distribution changes based upon geometry of the interconnect and P-E-N, the local potential consumed to *activate* the electrochemical reactions will change accordingly and will be symbiotically impacted by local changes in temperature. Higher cell temperatures reduce activation losses while lower cell temperatures increase activation losses. Hence, the thermal effects drive the performance metrics beyond SR of 30. Figure 5.10 shows the average solid temperature surface plot. After first observing the maxima for each value of IAR, notice the activation losses surface plot shown in Figure 5.11. The minima of activation losses follow closely with the maxima of

average temperature for each value of IAR. Around SR of 30, entropy generation due to ohmic losses become less than activation losses. As previously mentioned, ohmic losses are dominant below SR of 30 while activation losses dominate above SR of 30. For example, ohmic losses range from 11.08 mW/K to 2.92 mW/K at SR of 16, while activation losses have values between 7.52 mW/K and 5.36 mW/K at SR of 16. While at SR of 44, ohmic losses range from 5.35 to 2.32 mW/K and activation losses range from 6.36 to 5.40 mW/K. Concerning concentration losses, the changes in such are due primarily to changes in local current density. Figure 5.12 shows the concentration losses surface profile. Notice the maxima for each IAR value. The trend of the surface is due to changes in the inlet current density. Concentration losses are sensitive to local current density values. Local current density values determine the rate of diffusion of the constituents. At the inlet, the highest concentration gradient exists. Therefore, the inlet current density offers a good indication of the associate trends of concentration profiles. As result, the inlet current density surface, shown in Figure 5.13, offers insight to the trends observed with the concentration loss profiles. The concentration loss maxima observed for each value of IAR correlates to the maxima observed with the inlet current density profile. The increasing and decreasing trend before and beyond the maxima is also preserved.

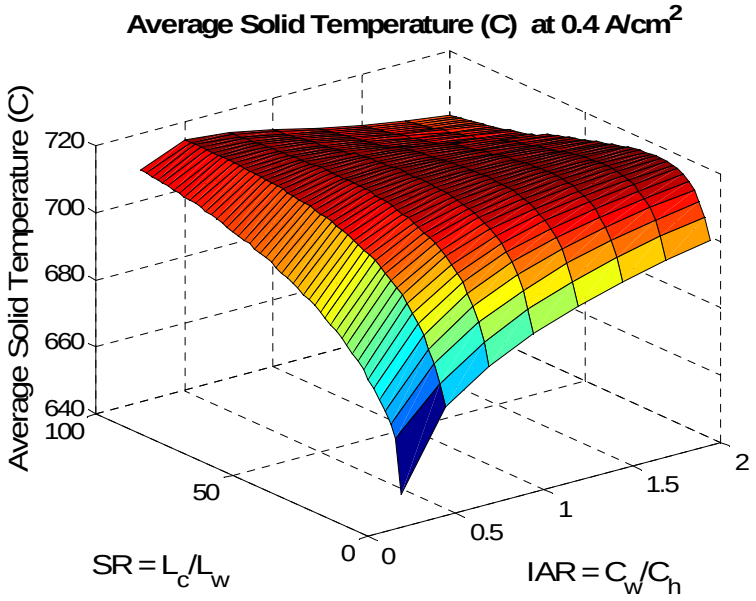

Figure 5.10. Surface plot of average solid temperature at 0.4 A/cm^2.

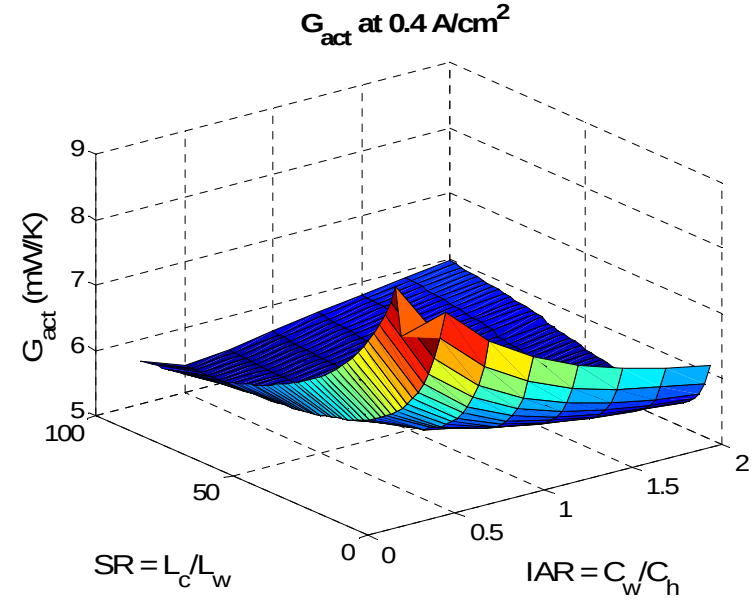

Figure 5.11. Surface plot of activation losses entropy generation at 0.4 A/cm^2.

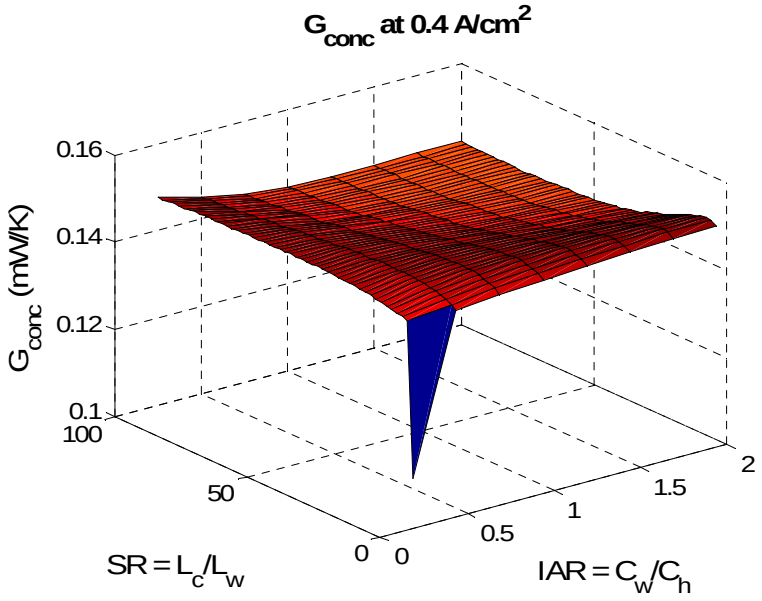

Figure 5.12. Surface plot of concentration losses entropy generation at 0.4 A/cm^2.

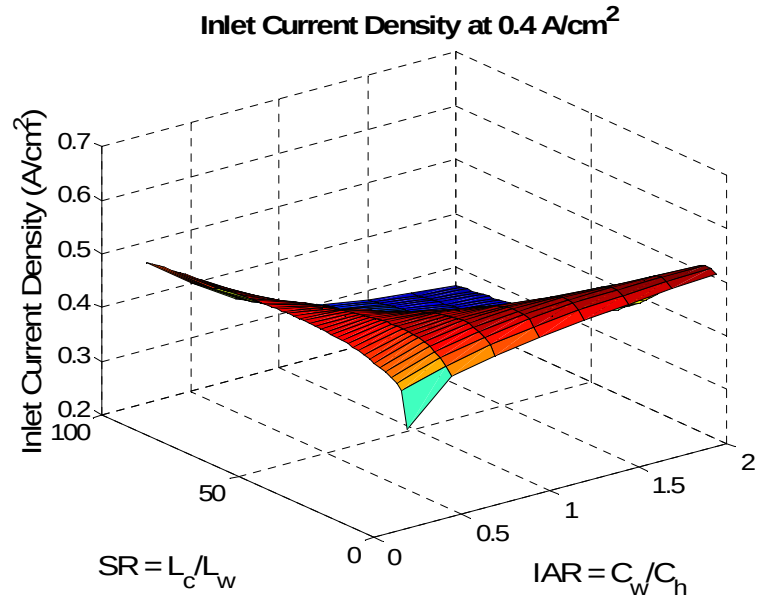

Figure 5.13. Surface plot of inlet current density at 0.4 A/cm^2.

There is an additional effect of the changes observed in electrochemical losses profiles as IAR and SR increase. Changes in electrochemical losses cause changes in by-product heat that is generated. The amount of heat generated dictates the amount of heat that is available

to be conducted by the cell. Since cell efficiency increases with SR and IAR (there is a plateau effect with marginal decreases beyond SR of 40 and IAR of 2), then heat generated is a maximum at SR of 4 and IAR of 0.25 and decreases as SR and IAR increase. Since thermal conductance decreases as SR and IAR increase and less heat generated, then heat conduction decreases as IAR and SR increase. Furthermore, decreasing thermal conductance causes temperature gradients to increase as SR and IAR increase as was shown in Figure 5.6. As a result, the surface plot of entropy generation due to heat conduction has a minimal value as shown in Figure 5.14. At SR of 10 and IAR of 2, heat conduction entropy generation is a minimum. Recall, entropy generation due to heat conduction is results from heat conduction through thermal gradients. Below SR of 10, heat conduction dominates the term. Above SR of 10, thermal gradients dominate the term. Furthermore, lower thermal conductance values will cause the cell to experience lower minimum temperatures and higher maximum temperature values. This trend allows for the gas temperature to approach the solid temperature more rapidly via heat convection thereby decreasing thermal-fluidic losses as SR increase as shown in Figure 5.15. Below SR of 10, more heat is available to be convected since less heat is conducted as IAR increases. Therefore, thermal-fluidic losses increase with IAR below SR of 10. Above SR of 10, thermal-fluidic losses decrease with IAR because less heat is available to be convected. Despite pressure drop increasing significantly with SR and IAR, pressure drop losses are relatively small compared to heat convection losses.

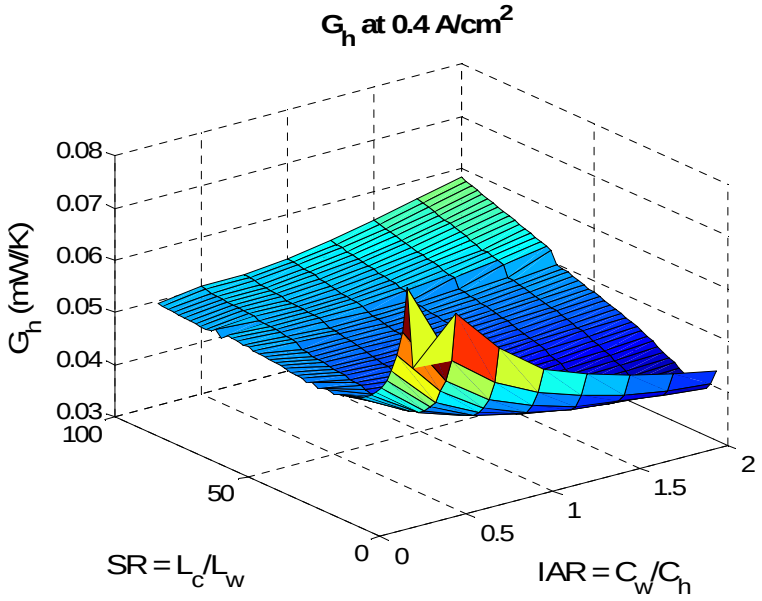

Figure 5.14. Surface plot of heat conduction entropy generation at 0.4 A/cm^2.

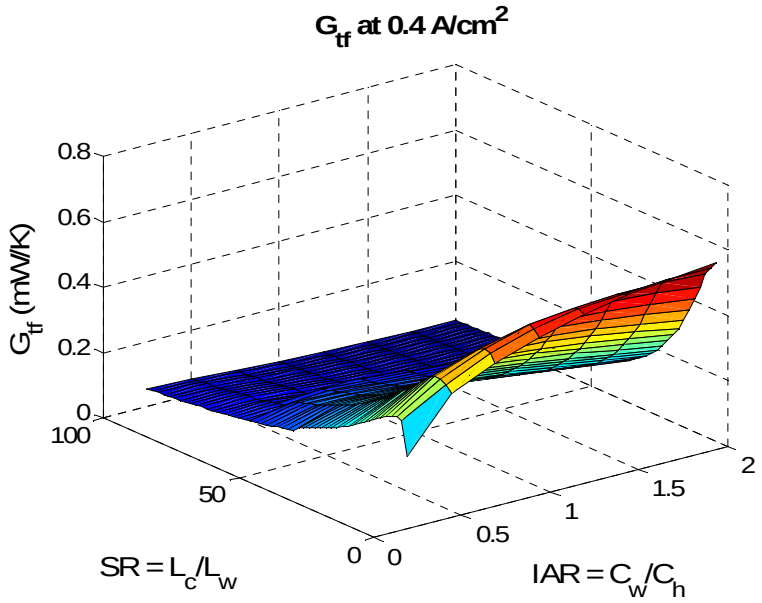

Figure 5.15. Surface plot of thermal-fluidic entropy generation at 0.4 A/cm^2.

Before presenting optimization results with specific thermal gradients, the thermal gradient surface plot needs to be further analyzed. As previously mentioned and shown in

Figure 5.6, thermal gradients substantially change with IAR and SR values. This change is due primarily to changes in thermal conductance. Thermal gradients are inversely related to thermal conductance values. The maximum thermal gradient for the design space was 1985 °C/m at SR of 100 and IAR of 2. This design had a thermal conductance of 0.0148 mW-m/K. The minimum thermal gradient for the design space was 62.9 °C/m with a thermal conductance value of 69.1 mW-m/K given a SR of 4 and IAR of 0.25. To further emphasize the inverse correlation between thermal gradients and thermal conductance, the inverse of thermal conductance surface plot is shown in Figure 5.16 along with the thermal gradients surface plot. The inverse correlation between thermal gradients and thermal conductance is clearly seen in Figure 5.16. The strong correlation between maximum thermal gradient and thermal conductance is further emphasized in Figure 5.17. A curve fit of the data yields a reasonable R^2 value of 0.944. Given this, careful selection of IAR and SR values is required in order to meet a particular design threshold of maximum allowable thermal gradients. Next, design recommendations are given based upon maximum allowable thermal gradients.

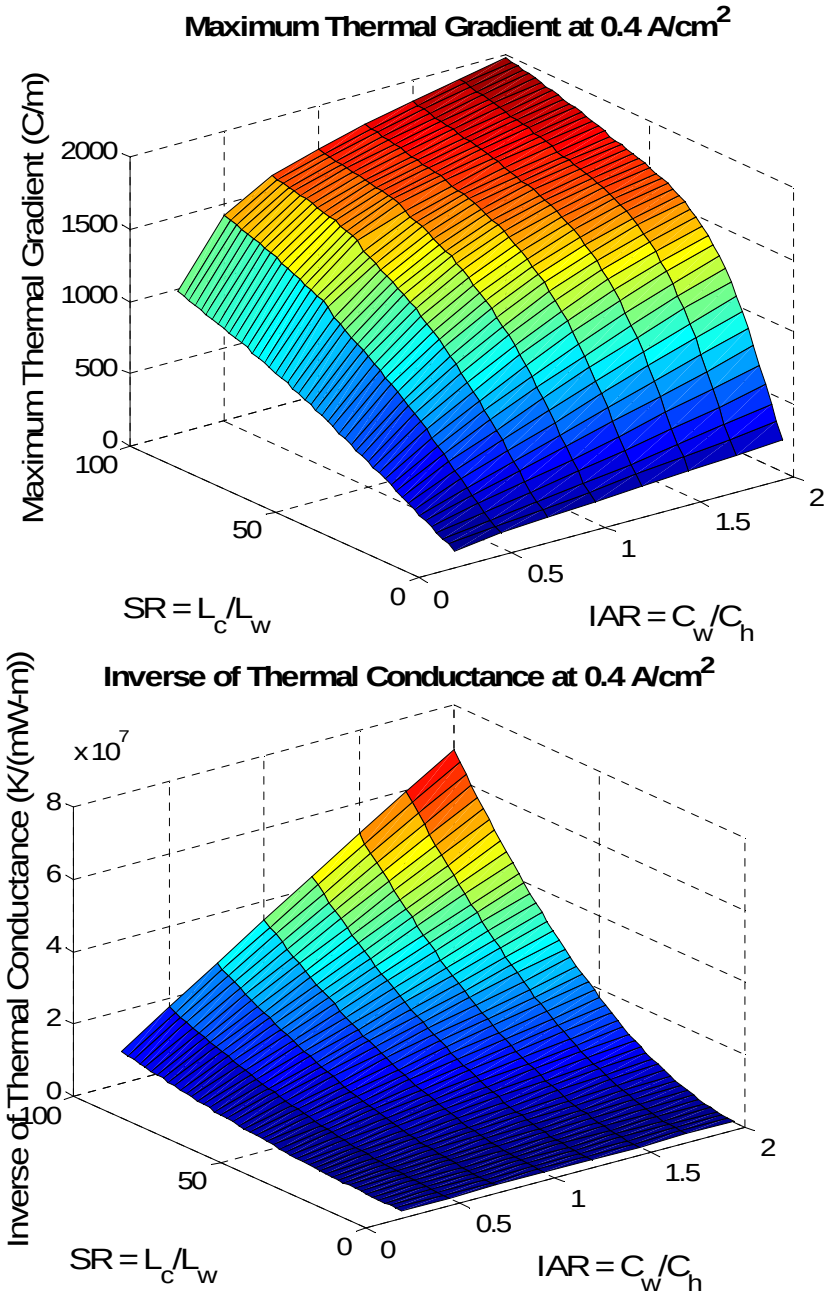

Figure 5.16. Inverse of thermal conductance and thermal gradients surface plot at current density of 0.4 A/cm^2.

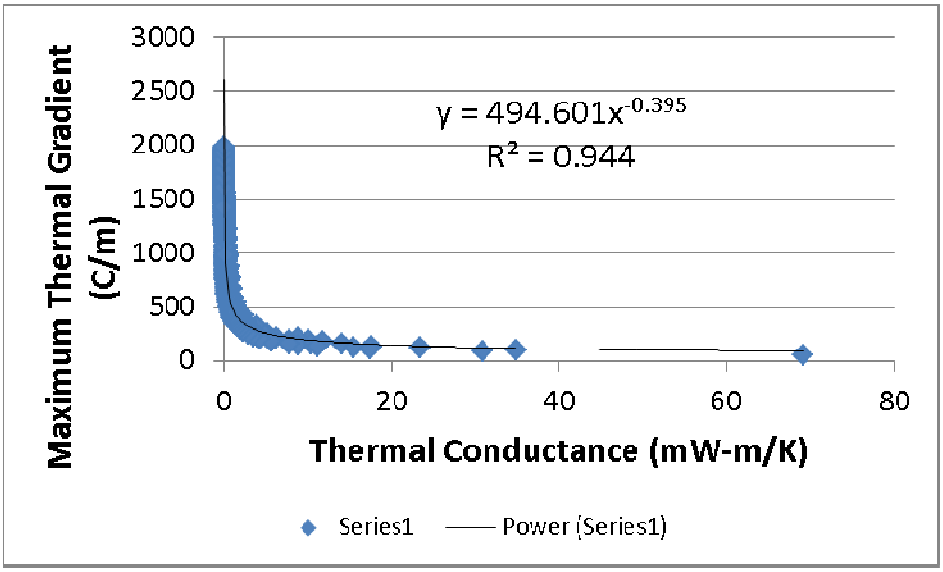

Figure 5.17. Plot of maximum thermal gradient versus thermal conductance with a power series curve fit of the data.

5.3 Optimization Study

As mentioned in the methodology chapter, a constrained single objective optimization problem was solved as described in Table 5.5. The fundamental objective is to maximize exergetic efficiency via the means objective of minimizing total entropy generation. Utilizing 2nd law efficiency is a better measure of performance than traditional measures such as power density or fuel cell efficiency [13]. However, 1st law metrics of efficiency and power density are key metrics of performance and are presented to describe performance in a manner which is translatable to traditional design methodologies. The optimization proceeds by noting the impact of maximum allowable thermal gradients and is varied from 250 °C/m to 2000 °C/m. Next, the surface response of the entire optimization space is presented.

Table 5.5. Description of optimization problem of minimizing gross entropy production.

Optimization Problem	
Fundamental objective	Maximize: $\varepsilon_{\mathrm{II}}$
Means objective	Minimize: $g_p = g_{tf} + g_h + g_{ohm} + g_{act} + g_{conc}$
Constraint	$\frac{\partial T}{\partial z} \leq \frac{\partial T}{\partial z}_{max}$ (250 °C/m – 2000 °C/m)

5.3.1 Optimization Results for Specific Thermal Gradients

The key distinction of the present dissertation is the consideration of maximum allowable thermal gradients in optimizing a planar SOFC design. By employing entropy generation minimization, the optimal design can be constructed with thermal gradients considered. As Nakajo [2] broached, the probability of failure is directly linked to maximum thermal gradient. For different design applications, a fuel cell designer may require different thermal gradient requirements. For the optimization, the range of thermal gradients considered were from 250 °C/m to 2000 °C/m and were varied in increments of 250 °C/m. For each maximum thermal gradient, the maximum 2nd law efficiency was found by minimizing total entropy generation for the range of IAR and SR values. Table 5.6 shows how the optimal design changes as maximum allowable thermal gradient changes. As an example, if the design required thermal gradients to be less than 250 °C/m, then IAR of 2 and SR of 4 would be selected. This design would have a 2nd law efficiency of 87.0% at 0.4 A/cm^2. While a design with a higher maximum thermal gradient tolerance of 2000 °C/m would have an IAR of 2 and a SR of 62. Before definitive design recommendations are given, explanation of the optimization results and considerations of pressure drop and manufacturability must be given.

Table 5.6. Optimization results with thermal conductance values at 0.4 A/cm^2 with baseline results shaded.

Maximum Thermal Gradient (°C/m)	IAR	SR	2nd Law Efficiency (%)	Thermal Conductance (mW/(m-K))
219	2	4	87.0	8.84
479	1.75	10	90.7	1.62
746	1.25	20	91.6	0.569
979	2	18	92.2	0.440
1249	1.75	28	92.6	0.208
1486	2	34	92.7	0.124
1583	2	40	92.8	0.0894
1758	2	62	92.7	0.0376
750.2	1	24	91.5	0.495

Table 5.6 shows how IAR and SR values change in order to satisfy the maximum allowable thermal gradient requirement and resulting maximum 2nd law efficiency. IAR ranges from 1.25 to 2 and SR ranges from 4 to 62. As previously mentioned, the general trend is that as thermal conductance decreases, maximum thermal gradient increases,. As thermal conductance is a function of thermal conductivity and cross-sectional area, IAR and SR values change accordingly to satisfy the thermal gradient constraint. For each thermal gradient constraint, there may be other designs which satisfy the required maximum thermal gradient, but it did not produce the maximum 2nd law efficiency (*i.e.,* minimum entropy generation). As was discussed in the surface plots section, entropy generation generally decreases as IAR and SR increase (i.e., there is some intermediate minimum, but the difference is miniscule beyond the associated IAR and SR values). The optimization simply selects the largest possible SR and IAR combination that will generate the smallest entropy production while satisfying the thermal gradient requirement. Each change in IAR and SR causes a change in the ohmic resistance due

to the direct dependence of ohmic losses on geometry. The ohmic resistance causes a change in the distribution of current which in turn affects the required potential to activate the electrochemical reactions. This thus affects the activation losses. Larger IAR and SR values reduce ohmic losses due to smaller interconnect geometry. The constriction resistance effect is the same for all designs because DGCW is fixed. Overall, reduction in electrochemical losses lead to less by-product heat generation. However, thermal conductance decreases as IAR and SR increase, and the temperature and thermal gradients profiles experience more significant extremes which will be discussed in the next section.

Given the optimization produced the maximum 2^{nd} law efficiency for a given thermal gradient tolerance, power density and fuel cell efficiency were tracked. As expected, power density and 1^{st} law efficiency mirrored the changes in 2^{nd} law efficiency as shown in Table 5.7. Again, when total entropy generation is minimized, electrochemical losses are minimized. Electrochemical losses account for more than 94% of total losses as inferred in Table 5.8.This causes the cell potential to increase thereby increasing power density and 1^{st} law efficiency. The implications are that higher allowable thermal gradients (i.e., above 1000 °C/m) produce better performing designs. Given the significance of electrochemical losses, further insights are given next.

Table 5.7. Results of optimization at 0.4 A/cm^2 with the baseline results shaded.

Maximum Thermal Gradient (°C/m)	2nd Law Efficiency (%)	1st Law Efficiency (%)	Power Density (mW/cm^2)
219	87.0	45.2	264.7
479	90.7	50.0	292.8
746	91.6	51.2	299.9
979	92.2	52.1	305.1
1249	92.6	52.6	307.7
1486	92.7	52.8	309.1
1583	92.8	52.8	309.3
1758	92.7	52.7	308.6
750.2	91.5	51.2	299.0

Table 5.8. Entropy generation results of the optimization at 0.4 A/cm^2 per entire full cell (*i.e.,* 10cm x10 cm footprint) with baseline results shaded.

Maximum Thermal Gradient (°C/m)	G_{tf+h} (mW/K)	G_{ec} (mW/K)	G_p (mW/K)
219	0.589	12.64	13.23
479	0.505	9.59	10.10
746	0.372	8.85	9.22
979	0.336	8.29	8.61
1249	0.246	8.03	8.28
1486	0.1875	7.92	8.11
1583	0.1611	7.92	8.08
1758	0.1153	8.07	8.18
750.2	0.345	8.95	9.30

As the optimized designs changed the geometry in order to meet the thermal gradient requirement, interesting changes occurred in current density profiles. Despite all designs having the same average current density value of 0.4 A/cm^2, each design produced different current density distributions as shown in Figure 5.18. This is important to note as local activation losses and concentration losses are functions of local current. With thermal conductance decreasing as maximum thermal gradients increases, cross-sectional area decreases. This causes the cell is

to generate 0.4 A/cm^2 of current in a smaller volume through a smaller cross-sectional area. Therefore, as thermal conductance decreases, the location of the maximum current density shifts further downstream and lower current densities further upstream. Such changes in local internal maxima and minima are caused by changes in local chemical potential, compounded by thermal effects, which must redistribute *local* current to match the set point *average* current density. Thermal effects are further explained in the next section. These changes are central to the electrochemical entropy generation. Next, a discussion of consideration of pressure drop and manufacturability of the design is given next.

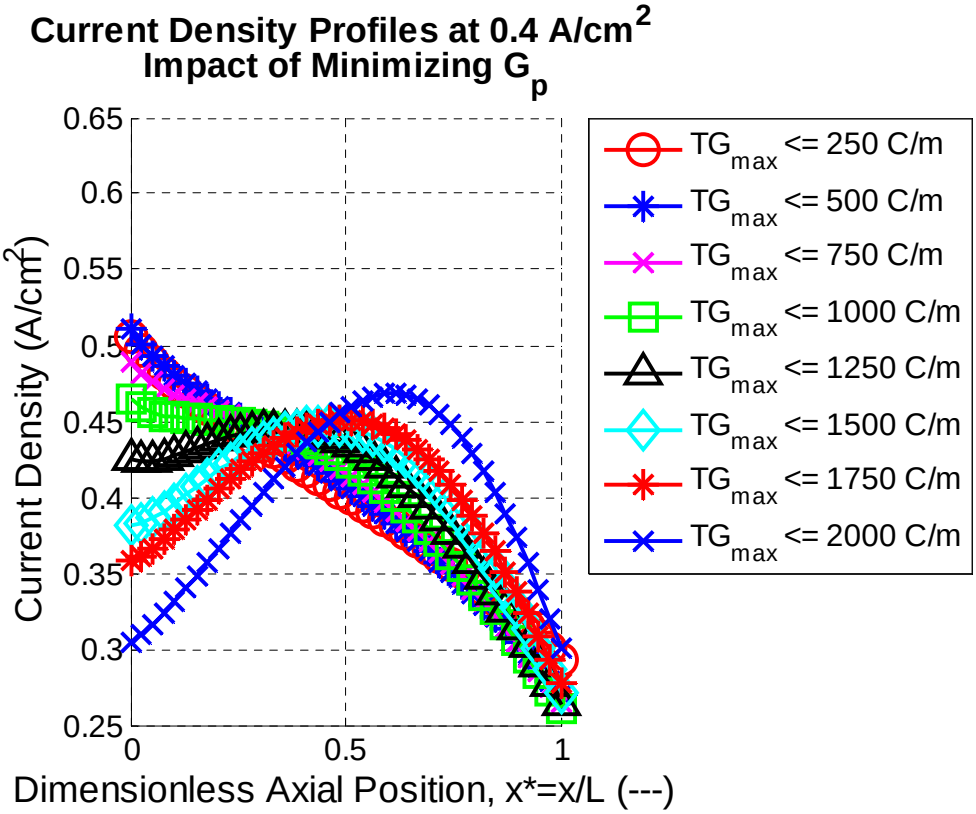

Figure 5.18. Current density profiles for the optimized designs.

In using thermodynamic optimization with constraints on thermal gradients, pressure drop and manufacturability of the design must be considered as well. The pressure drop across the cell impacts the balance of plant of a fuel cell system. Adverse pressure gradients can cause effects throughout the rest of the system which may contain vital components that are sensitive to pressure changes (*e.g.,* heat exchangers, turbines, compressors, *etc*). Additionally, there may be design tolerances that allow for larger thermal gradients. However, consideration of manufacturability must be taken into account. Table 5.9 offers insight into both pressure drop considerations and manufacturability. Clearly, as the gas channel dimensions and unit cell width get smaller, the pressure drop increases. Above a maximum thermal gradient of 1500 °C/m, the pressure drop exceeds 5%. More severe is above 1750 °C/m where the pressure drop is nearly 20%. The fuel cell system designer would have to strongly consider the implications of a system with such a large pressure drop in instances with maximum thermal gradient tolerances above 1500 °C/m. In terms of manufacturability, to produce the designs above 1000 °C/m, the manufacturer would have to be able to manufacture to at least $1/100^{th}$ of a millimeter. Obviously, the lower thermal gradient designs have the benefit of a higher manufacturing tolerances of $1/10^{th}$ of a millimeter. Before final design recommendations are broached, there is a need to perform a heat transfer analysis that examines the temperature profiles, thermal gradient profiles, and the Biot number of the associated designs.

Table 5.9. Optimization results with thermal conductance values at 0.4 A/cm^2 with baseline results shaded.

Maximum Thermal Gradient (°C/m)	Pressure Drop (%)	C_w (mm)	C_h (mm)	L_w (mm)
219	0.005	6.25	3.125	25
479	0.058	2.50	1.429	10
746	0.214	1.25	1	5
979	0.483	1.389	0.694	5.56
1249	1.29	0.83	0.510	3.57
1486	3.25	0.735	0.368	2.94
1583	5.29	0.625	0.313	2.50
1758	19.56	0.403	0.202	1.613
750.2	0.234	1.042	1.042	4.17

5.3.2 Heat Transfer Analysis

The heat transfer nuances of the optimization required more analysis to aid design recommendations. As previously mentioned, the thermodynamic optimization selects the design with the largest 2nd law efficiency within each thermal gradient constraint. The thermal gradients are strongly coupled to the thermal conductance. Thermal conductance is the product of thermal conductivity and the cross-sectional area of the control volume. As maximum allowable thermal gradient increased, thermal conductance values decreased. Smaller thermal conductance values caused the cell temperature profiles to experience more significant extremes as shown in Figure 5.19. Smaller thermal conductance values means that the heat cannot be as readily conducted. Therefore, the parabolic temperature profiles of the solid reach higher temperatures further downstream. This also causes the inlet solid temperature to decrease with thermal conductance.

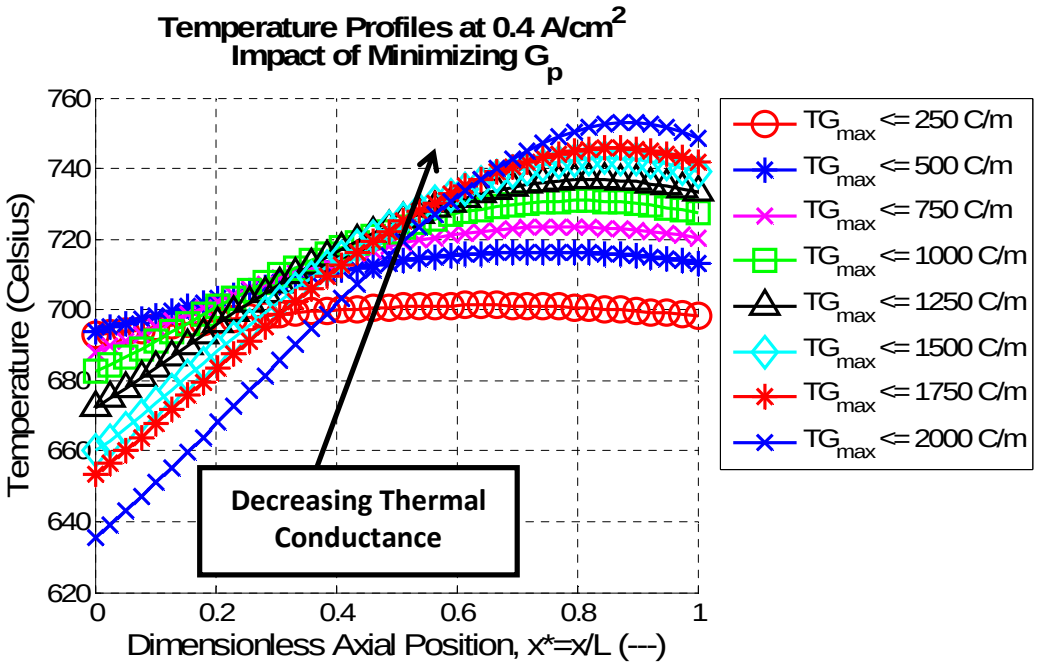

Figure 5.19. Temperature profiles for each optimized design at 0.4 A/cm^2.

Such temperature extremes induced by lower thermal conductance lead to the thermal gradient profiles exhibiting noticeable trends as shown in Figure 5.20. First, larger magnitude thermal gradients offset the reduction in conductance given the boundary heat transfer phenomena. Second, smaller conductance values result in larger magnitude gradients at the exit edges of the unit cell; hence, interior maxima are more gradual in nature and occur further upstream from the exit. Another contributing factor is the geometric changes to the interconnect which cause changes in the current density distribution. This causes the heat generation profile to change (*i.e.,* joule heating effects) as shown in Figure 5.20. Larger SR and IAR values cause the location of the maximum heat generation to shift to further downstream. Therefore, the temperature reaches a maximum further downstream. Third, the cell reaches a maximum thermal gradient within the first 30% of the axial length. This is primarily a byproduct

of the boundary conditions, and the influence of thermal conductance values. At the inlet boundary, a large amount of heat escapes to the ambient through radiation and free convection. Within the first 30% of the axial length, heat convection and conduction will be a maximum. The heat generated by the cell can only escape the solid via convection to the oxidant, conduction downstream, or at the boundaries. This thermal energy originates from the heat generated by the electrochemical reactions. Since lower thermal conductance values reduces the rate at which the generated heat can conduct, then the position at which the maximum thermal gradient occurs changes. Lower thermal conductance values cause the maximum thermal gradient to occur further downstream.

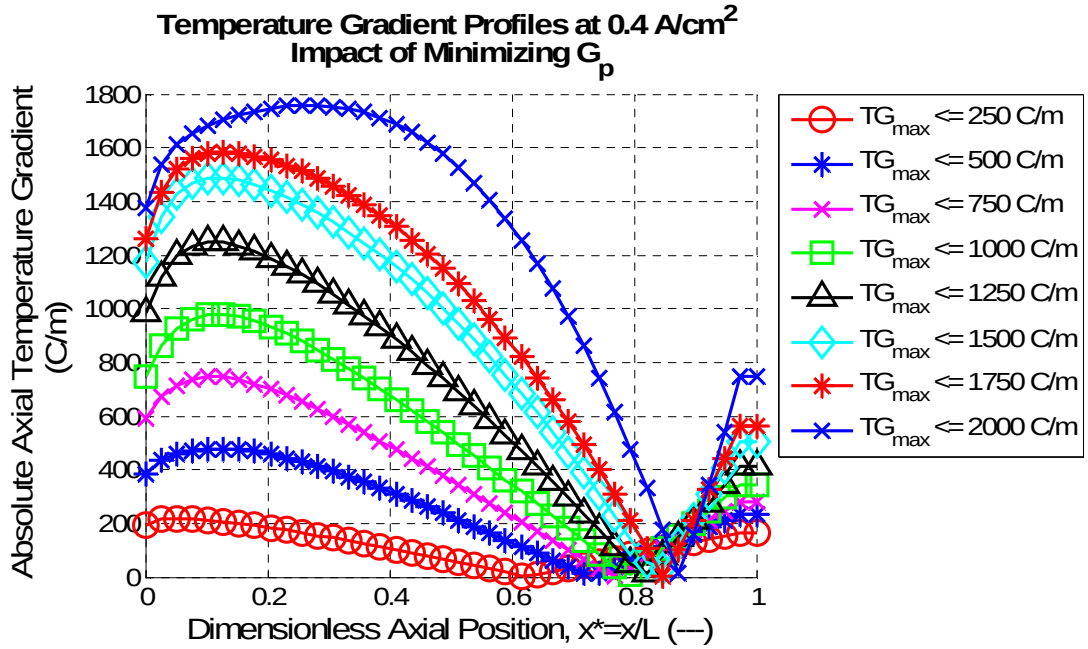

Figure 5.20. Temperature gradient profiles for each optimized design at 0.4 A/cm^2.

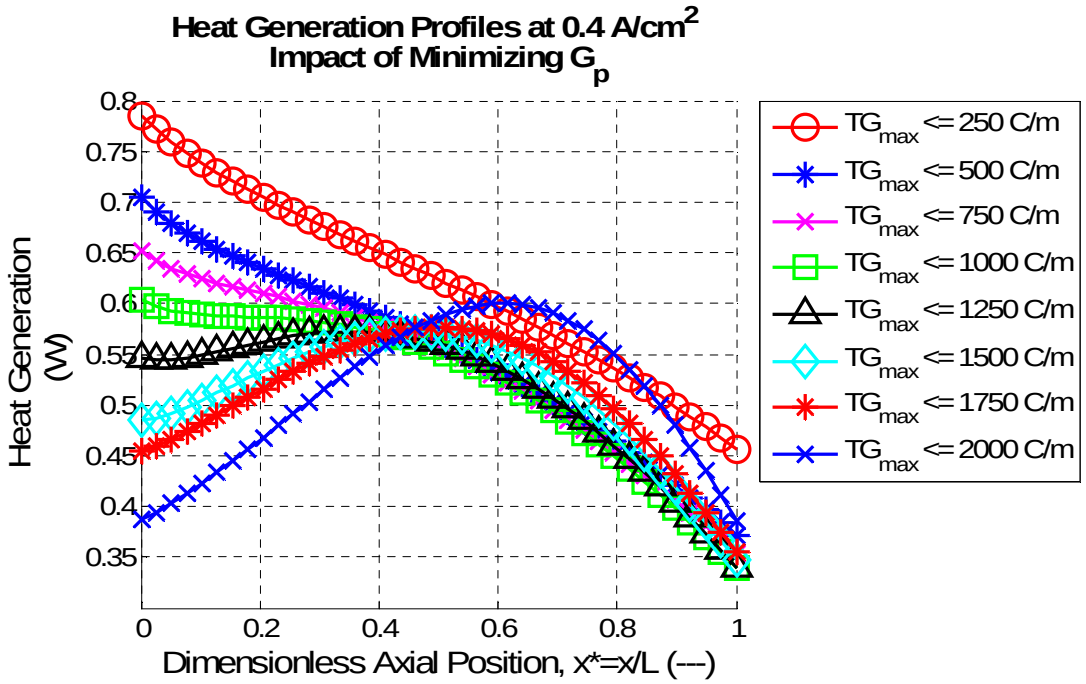

Figure 5.21. Heat generation profiles for each optimized design at 0.4 A/cm^2.

In order to assess the appropriateness of considering only axial thermal gradients and to make well informed design recommendations, a Biot number analysis was conducted. In assessing thermal gradients in the cross section of the control volume, the Biot number was calculated. If the Biot number is less than 0.1, then thermal gradients in the cross-section of the control volume were deemed negligible. For the cross-section shown in Figure 5.22 and the assumption of including the fuel stream in the solid domain, the Biot number was calculated using Equation 5.5 below.

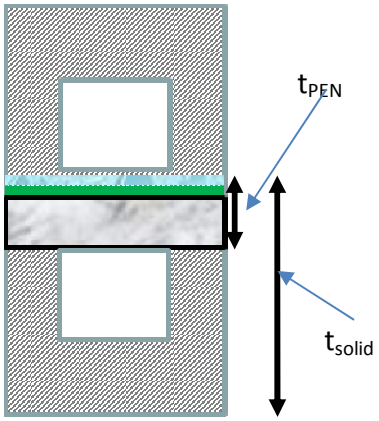

Figure 5.22. Cross-sectional view of the control volume displaying the characteristic lengths for Biot number calculations.

$$Bi = h_{avg} \sum_i \frac{t_i}{k_i} \tag{5.5}$$

In Equation 5.5, h_{avg} the average heat transfer coefficient, t_i is the conductive characteristic length, and k_i is the thermal conductivity of the solid material. As in Chapter 4, the two characteristic lengths considered are in the P-E-N and the solid half the cell as shown in Figure 5.22.

The thermal gradients in the axial direction have been the primary focus given the preliminary Biot number analysis done on the baseline design. However, the extreme geometries (*e.g.,* large SR and small IAR) would introduce greater likelihood of significant thermal gradients in the cross-section of the design. For the optimized designs, 3 of the 8 cases exceeded a Biot number of 0.1 as shown in Table 5.10. Figures 5.23-5.26 show the cases with Biot numbers above 0.1 and the Biot number for the entire optimization, respectively. Intermediate values of SR and larger (e.g. 34 and larger) lead to super critical Biot numbers. There were 247 of 392 (63.0%) cases that had Biot numbers in the P-E-N greater than 0.1.

Additionally, there were 122 cases of 392 (31.1%) that had Biot numbers greater than 0.1 in the solid length. This implies that consideration of cross-sectional thermal gradients is needed. This analysis is left as a future works item. Nevertheless, the axial thermal gradients offer at least a conservative estimate of maximum thermal gradients seen in a design.

Table 5.10. Biot number of the optimized designs at 0.4 A/cm^2 with baseline results shaded.

Maximum Thermal Gradient (°C/m)	Biot Number P-E-N	Biot Number Solid	IAR	SR
219	0.0160	0.0135	2	4
479	0.0343	0.0152	1.75	10
746	0.0521	0.0181	1.25	20
979	0.0703	0.0196	2	18
1249	0.0963	0.0231	1.75	28
1486	0.1328	0.0283	2	34
1583	0.1561	0.0320	2	40
1758	0.2410	0.0468	2	62
750.2	0.0549	0.0196	1	24

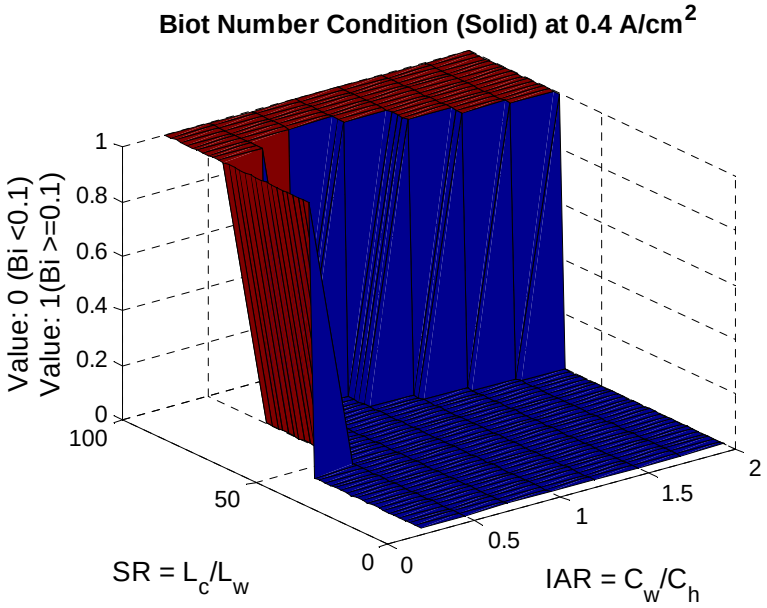

Figure 5.23. Critical Biot number condition in the solid (i.e., below 0.1) at 0.4 A/cm^2.

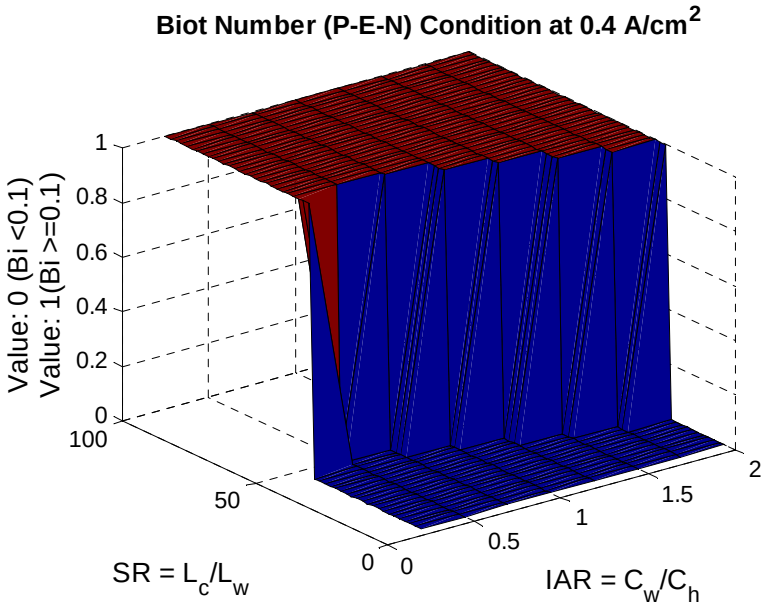

Figure 5.24. Critical Biot number condition in the P-E-N (i.e., below 0.1) at 0.4 A/cm^2.

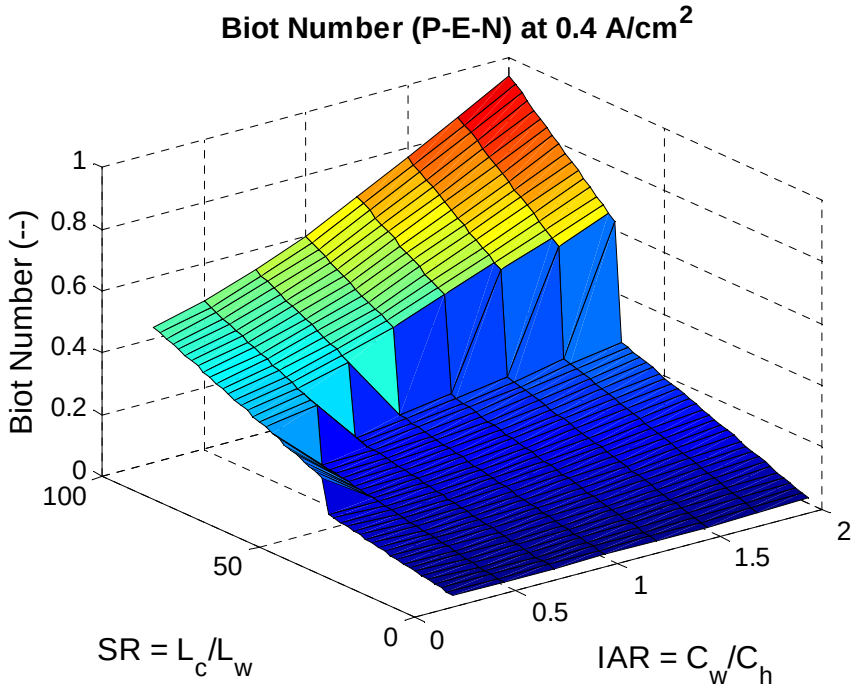

Figure 5.25. Biot number (P-E-N) surface plot at 0.4 A/cm^2.

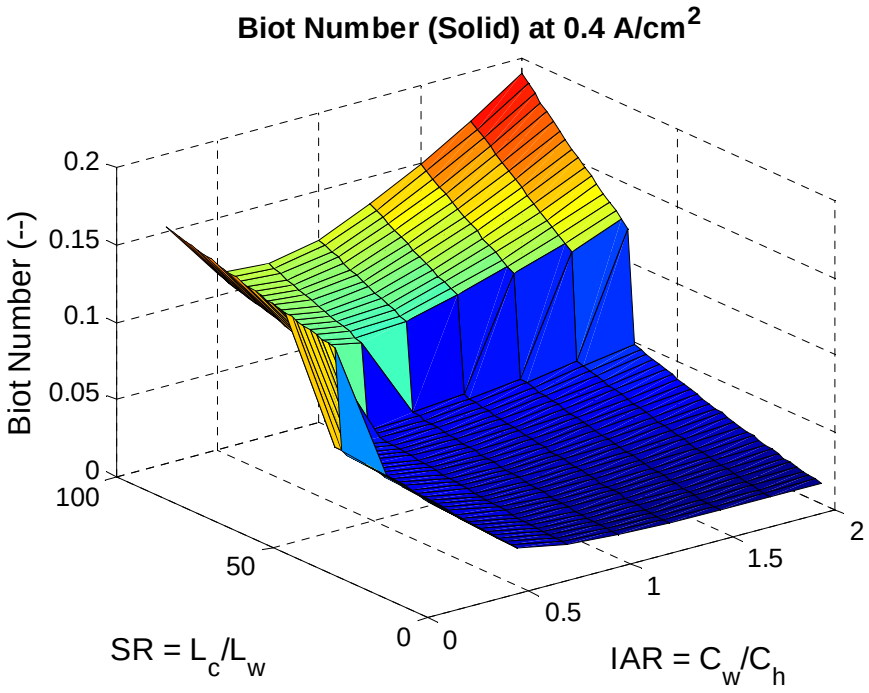

Figure 5.26. Biot number (solid) surface plot at 0.4 A/cm^2.

Given the results of the heat transfer analysis, design recommendations can now be presented. The key point of recommendation is for designs that have higher tolerances of thermal gradients. That is, thermal gradients above 1250 °C/m. In considering the performance metrics, pressure drop, manufacturability, and Biot number, for designs that have high thermal gradient tolerances above 1250 °C/m, it is recommended that an IAR value of 1.75 and SR value of 28 be used. The pressure drop is relatively low at 1.29%. The Biot number is less than 0.1 signifying cross-sectional thermal gradients are not significant. Performance metrics are relatively high at 92.6%, 307.7 mW/cm^2, and 52.6% for 2nd law efficiency, power density, and fuel cell efficiency, respectively. These performance metrics are within 1% of the maximum for the entire optimization domain. For designs that require maximum thermal gradients below

1000 °C/m, the results presented in Table 5.6 would suffice given the low pressure drop values and Biot numbers.

5.4 Conclusions

A thermodynamic optimization was conducted that noted the effects of thermal gradients on the design a planar SOFC. Conclusions are made concerning design trends and recommendations. It was concluded that a planar SOFC can be designed for maximum 2nd law efficiency to accommodate different maximum thermal gradient tolerances. Given the present results, in designing a planar SOFC, consideration for maximum thermal gradients must be included. A high performing planar SOFC design can be wrought, while limiting maximum thermal gradients. Through modification of dimensionless geometric parameters IAR and SR, total entropy generation was minimized to maximize 2nd law efficiency. The 2nd law efficiency, power density, and fuel cell efficiency had nearly identitical profile shapes because of the dominance of electrochemical losses. It was concluded that as SR and IAR increased, all performance parameters asymptotically increased with marginal decreases in performance beyond SR of 40 and IAR of 2. A maximum 2nd law efficiency of 92.8% was noted for a SR value of 40 and a IAR value of 2.

Despite asymptotic improvements in performance with increased SR and IAR values, the pressure drop can be as high as 80% with manufacturing requirements on the order of 1/100th of a millimeter. This implies that pressure drop limitations and manufacturability must be considered in the design limitation of the SOFC.

Another key conclusion was concerning the correlation of thermal conductance and maximum thermal gradients. Thermal conductance values are inversely correlated to maximum

thermal gradients. As thermal conductance decreased, maximum thermal gradients increased. It was observed that thermal conducance values above 0.44 mW-m/K had maximum thermal gradients below 1000 °C/m. Thermal gradients can be significant in the P-E-N and solid composite.

Per recommendations, in order to design a SOFC with maximum thermal gradients below 1000 °C/m, thermal conductance of the solid material needs to be above 0.44 mW-m/K. For the set of modeling assumptions and operating conditions, the best design in this regime is with IAR of 2 and SR of 18. If design thermal gradient tolerances need to be relaxed or more restrictive, the present dissertation recommends the following designs shown in Table 5.11. For maximum thermal gradients above 1250 °C/m, IAR of 1.75 and SR of 28 are recommended, because high performance is preserved, pressure drop is limited to 1.29%, and cross-sectional thermal gradients are not significant. This design has a 2nd law efficiency of 92.6%, power density of 307.7 mW/cm^2, and fuel cell efficiency of 52.6%. As shown in Table 5.12, this design is within 1% of maximum performance metrics.

Table 5.11. Recommended optimized designs with thermal conductance values at 0.4 A/cm^2 with baseline results shaded (for all designs DGCW is 0.25 and EER is 50).

Maximum Thermal Gradient (°C/m)	IAR	SR	Thermal Conductance (mW/(m-K))
250	2	4	8.84
500	1.75	10	1.62
750	1.25	20	0.569
1000	2	18	0.440
1250 or higher	1.75	28	0.208
1583	2	40	0.0894

Table 5.12. Recommended design performance metrics at 0.4 A/cm^2 with the baseline results shaded.

Maximum Thermal Gradient (°C/m)	2nd Law Efficiency (%)	1st Law Efficiency (%)	Power Density (mW/cm^2)
250	87.0	45.2	264.7
500	90.7	50.0	292.8
750	91.6	51.2	299.9
1000	92.2	52.1	305.1
1250 or higher	92.6	52.6	307.7
1583	92.8	52.9	309.3

In closing, the present dissertation has offered a nuanced design methodology and recommendations to aid in the advancement of SOFC technology. The next chapter will summarize the entirety of conclusions for the dissertation.

6 CONCLUSIONS

The dissertation had two major conclusions. First, four dimensionless geometric parameters were developed and can be used to design a planar solid oxide fuel cell. Second, entropy generation minimization may be used to modify the architecture of a SOFC to optimally balance thermal gradients and performance. Each of these conclusions and sub points are presented next.

6.1 Dimensionless Geometric Parameters

- Dimensionless Gas Channel Width (DGCW), Internal Aspect Ratio (IAR), Electrolyte to Electrode Ratio (EER), and Slenderness Ratio (SR) impacted power density by as much as 35%, 284%, 1%, and 192%, respectively.
- DGCW had a limit of 0.85. Above DGCW of 0.85, the cell does not produce power due to high constriction resistance in the interconnect.
- 2^{nd} law efficiency varied from 42.9% to 89.5% for IAR ranging from 0.2 to 5 under baseline conditions of DGCW of 0.5, EER of 50, and SR of 24.
- 2^{nd} law efficiency varied from 40.6% to 94.6% for SR ranging from 5 to 100 under baseline conditions of DGCW of 0.5, EER of 50, and IAR of 1.
- Thermal gradients ranged from 410 °C/m to 1862 °C/m for IAR of 0.2 to 5.
- Thermal gradients ranged from 120 °C/m to 1488 °C/m for SR of 5 to 100.

6.2 Thermodynamic Optimization for SOFC

A thermodynamic optimization was conducted that noted the effects of thermal gradients on the design of a planar SOFC. In designing a planar SOFC for maximum performance, consideration for maximum thermal gradients must be included. Conclusions are made concerning design trends, recommendations, and insight on physical phenomena.

- As SR and IAR increased, all performance parameters (2^{nd} law efficiency, fuel cell efficiency, and power density) asymptotically increased with less than 1% decreases beyond SR of 40 and IAR of 2.
- A maximum 2^{nd} law efficiency of 92.8% was noted for a SR value of 40 and a IAR value of 2.
- As IAR increased from 0.2 to 2 and SR increased from 4 to 100, maximum thermal gradients increased from 62.9 °C/m to 1985 °C/m.
- Pressure drop limitations and manufacturability must be considered in the design of SOFC.
- Despite asymptotic improvements in performance with increased SR and IAR values, the pressure drop can be as high as 80%.
- Manufacturing requirements can require accuracy on the order of $1/100^{th}$ of a millimeter.

Another key conclusion was concerning the correlation of thermal conductance and maximum thermal gradients.

- Thermal conductance values above 0.44 mW-m/K had maximum thermal gradients below 1000 °C/m.
- As thermal conductance decreased, maximum thermal gradients increased.
- There is strong correlation between maximum thermal gradient and thermal conductance. Thermal conductance values are inversely correlated to maximum thermal gradients. The R^2 value for curve fit of the data is 0.944 indicating a strong relationship between thermal conductance and maximum thermal gradients.
- The Biot number analysis indicate that thermal gradients may arise in the P-E-N and solid composite (*i.e.,* P-E-N and of the interconnect).
- Thermal gradients significantly impacted the design in 63% of the cases studied, indicating the importance of optimal selection of the dimensionless geometric parameters.

Based upon the research presented in this thesis, the following design recommendations are provided:

- In order to design a SOFC with maximum thermal gradients below 1000 °C/m, thermal conductance of the solid material needs to be greater than 0.44 mW-m/K.
- For the set of modeling assumptions and operating conditions with current density of 0.4 A/cm^2, fuel utilization of 85%, and NOS of 7, the best design in this regime is with IAR of 2 and SR of 18. This design has a 2nd law efficiency of 91.6%, power density of 299.9 mW/cm^2, and fuel cell efficiency of 51.2%.

- If thermal gradient tolerances need to be relaxed or more restrictive, the present dissertation recommends the following designs shown in Table 6.1.

Table 6.1. Recommended optimized designs with thermal conductance values at 0.4 A/cm^2 with baseline results shaded (for all designs DGCW is 0.25 and EER is 50).

Maximum Thermal Gradient (°C/m)	Internal Aspect Ratio (IAR)	Slenderness Ratio (SR)	Thermal Conductance (mW/(m-K))
250	2	4	8.84
500	1.75	10	1.62
750	1.25	20	0.569
1000	2	18	0.440
1250 or higher	1.75	28	0.208
1583	2	40	0.0894

- For maximum thermal gradients above 1250 °C/m, IAR of 1.75 and SR of 28 is recommended because high performance is preserved, pressure drop is limited to 1.29%, and cross-sectional thermal gradients are not significant. This design has a 2nd law efficiency of 92.6%, power density of 307.7 mW/cm^2, and fuel cell efficiency of 52.6%. As shown in Table 6.2, this design is within 1% of maximum performance metrics.

Table 6.2. Recommended design performance metrics at 0.4 A/cm^2 with the baseline results shaded.

Maximum Thermal Gradient (°C/m)	2nd Law Efficiency (%)	1st Law Efficiency (%)	Power Density (mW/cm^2)
250	87.0	45.2	264.7
500	90.7	50.0	292.8
750	91.6	51.2	299.9
1000	92.2	52.1	305.1
1250 or higher	92.6	52.6	307.7
1583	92.8	52.9	309.3

7 FUTURE WORK

The present dissertation broaches potential future works items. Potential future works items include adding internal reformation effects, including higher fidelity in the modeling approach (e.g., constriction resistance effects in the electrode and 3D model), performing a statistical analysis on the dimensionless geometric parameters and noting their impact on performance (*i.e.,* 2^{nd} law efficiency, power density, thermal gradients, thermal conductance, and sources of entropy generation), and developing dimensionless transport groups to gain further insight in design and performance analysis. Each of these future works items are discussed in more detail.

7.1 Internal Reformation Effects

Recently, the literature has noted the impact of internal reformation effects on SOFC performance. Wang [69] noted the impact internal reformation effects have on concentration polarization. This indicates that there would be greater sensitivity to EER when internal reformation effects are included. Wongchanapai [50] noted the impact of including internal reformation of methane in modeling a SOFC. It was concluded that geometry and operating conditions must be carefully selected given the greater sensitivity to thermal gradients when internal reformation effects are included. From this work, location and magnitude of thermal gradients would be impacted by inclusion of internal steam reformation. Selection of IAR, SR, DGCW, and EER would be effected. Park [85] studied the effects of steam to carbon ratio and its ultimate impact on temperature fields when including the effects of internal reformation of methane. In light of the significance of steam to carbon ratio, a proper selection must be made in order to frame the significance of steam internal reformation on the performance of a SOFC.

7.2 Higher Fidelity Modeling

Including constriction resistance effects and utilizing a 3D model to supercritical Biot number scenarios would create a higher fidelity model. There were 247 of 392 cases simulated that had Biot numbers greater than 0.1. A 3D model would characterize the thermal gradients in the cross-section of such designs. First discussion of the constriction resistance effects is given, then the potential of 3D modeling.

Nelson and Haynes [52] included the effects interconnect constriction resistance on mass transport through the porous electrodes. As shown in Figure 7.1, both mass and electronic path lengths are impacted by the geometry of the interconnect. Nelson showed that smaller unit cell widths result in lower ohmic resistances and higher fuel depletion current densities. Though Nelson showed improved cell performance through modifying the interconnect geometry, thermal considerations were not accounted for. The future work should modify the 1D fuel cell model to include constriction resistance effects. The dimensionless geometric parameter would be varied again in the same manner used in the sensitivity study. It is expected that EER, DGCW, and IAR will be significantly impacted. With constriction resistance effects included in the modeling approach, the P-E-N structure can be optimized.

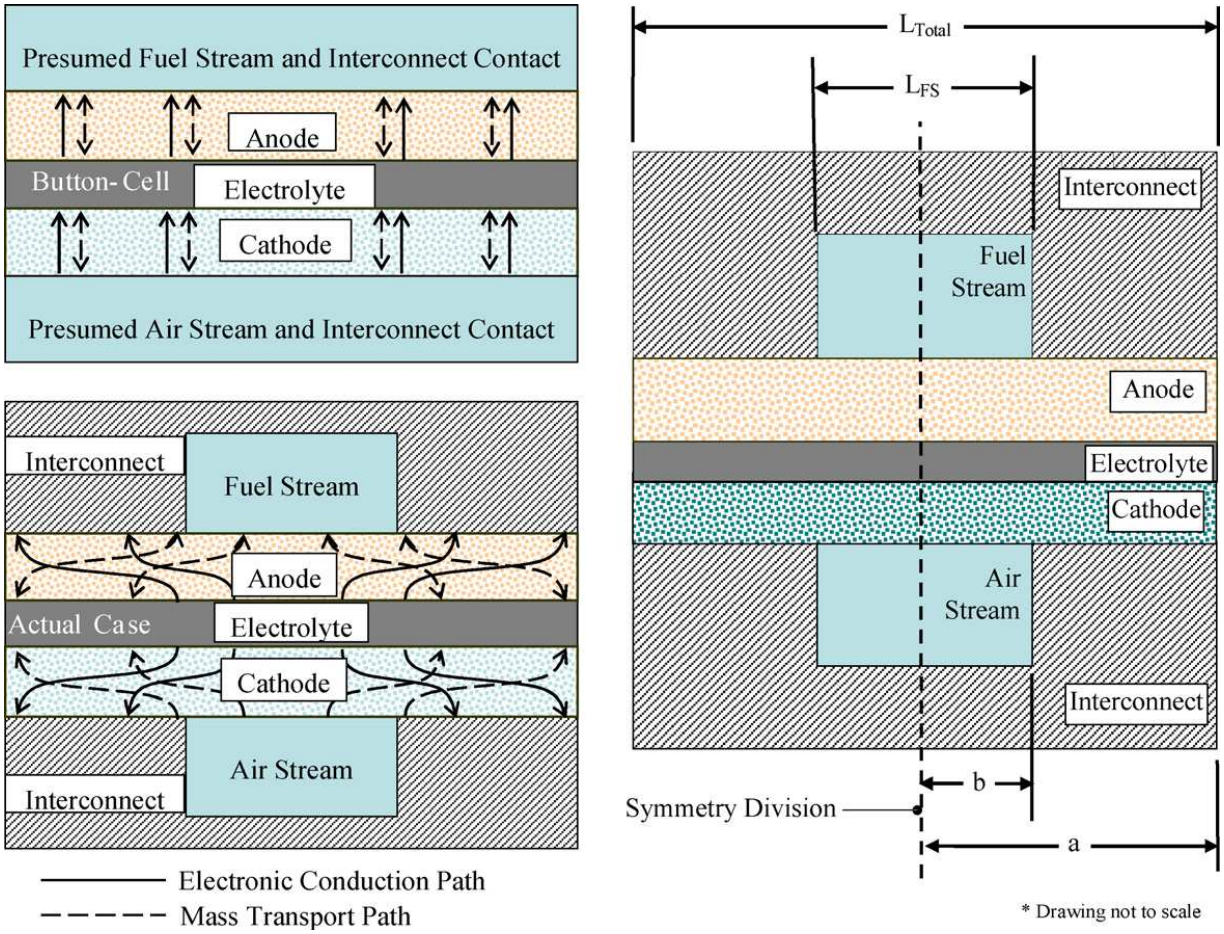

Figure 7.1. Diagram detailing impact of interconnect geometry on mass and electronic transport in comparison to traditional button cell presumptions.

The optimization had cases when the Biot number was above 0.1 thereby indicating that thermal gradients in the cross-section of the control volume were significant. Given such, a 3D modeling approach is needed to quantify the significance of such thermal gradients as well as offer further insights to the optimization approach. Recently, Nikooye [113] noted the significance of thermal gradients in the cross-section by conducting a 3D finite element analysis of a planar SOFC. It was noted that when including the effects of internal reformation of methane, thermal gradients in the cross-section can exceed that in the axial direction. In one

case, axial thermal gradients were 1600 °C/m while cross-sectional thermal gradients were 3500 °C/m.

7.3 Statistical Analysis on Dimensionless Parameters and Performance

Chapters 5 highlighted the impact of the dimensionless parameters on performance and thermophysical properties. Exergetic efficiency, 1^{st} law efficiency, power density, thermal gradients, thermal conductance, and sources of entropy generation were all impacted by changes in the dimensionless geometric parameters. The results highlighted a need to statistically quantify the how each dimensionless geometric parameter impacts aforementioned performance and thermophysical metrics. A Monte Carlo analysis is needed to note how IAR, DGCW, SR, EER, and their interactions impact performance. A sensitivity study can be conducted which includes a Monte Carlo sensitivity analysis. The effects of IAR, DGCW, SR, EER, and their interactions will be quantified. It will be interesting to perform a probabilistic study of how likely exergetic efficiency, power density, thermal conductance, and sources of entropy generation are to change and the amount of their variability. These results would provide SOFC designers insight and quantification on how the effects of geometry impact performance.

7.4 Dimensionless Group Exploration

While the developed dimensionless geometric parameters helped design and analyze planar SOFC designs, there were pertinent information gathered from classic dimensionless parameters such as Biot number. Given this, there would be further insights gathered by analyzing designs based upon dimensionless transport groups such as Biot number. The governing equations would be recast in dimensionless form and the relevant dimensionless groups would fall out. Insights on dimensionless groups relate to thermal gradients and

performance would arise. This would add greatly to design and performance analysis of planar SOFC.

BIBLIOGRAPHY

1. Atkinson, A. and B. Sun, *Residual stress and thermal cycling of planar solid oxide fuel cells.* Materials Science and Technology, 2007. **23**(10): p. 1135-1143.
2. Nakajo, A., et al., *Simulation of thermal stresses in anode-supported solid oxide fuel cell stacks. Part I: Probability of failure of the cells.* Journal of Power Sources, 2009. **193**(1): p. 203-215.
3. Achenbach, E., *Three-dimensional and time-dependent simulation of a planar solid oxide fuel cell stack.* 1994. **49**: p. 333.
4. Achenbach, E., *Response of a solid oxide fuel cell to load change.* Journal of Power Sources, 1995. **57**(1-2): p. 105.
5. Aguiar, P., C.S. Adjiman, and N.P. Brandon, *Anode-supported intermediate temperature direct internal reforming solid oxide fuel cell. I: model-based steady-state performance.* Journal of Power Sources, 2004. **138**(1-2): p. 120.
6. Aguiar, P., D. Chadwick, and L. Kershenbaum, *Modelling of an indirect internal reforming solid oxide fuel cell.* Chemical Engineering Science, 2002. **57**(10): p. 1665.
7. Bessette, N.F., II and W.J. Wepfer, *A mathematical model of a tubular solid oxide fuel cell.* Transactions of the ASME. Journal of Energy Resources Technology, 1995. **117**(1): p. 43.
8. Brandon, N.P., P. Aguiar, and C.S. Adjiman, *Anode-supported intermediate-temperature direct internal reforming solid oxide fuel cell.* Journal of Power Sources, 2005. **147**(1-2): p. 136.
9. Damm, D.L. and A.G. Fedorov. *Simplified thermal analysis of the SOFC transients during startup/shutdown.* in *Proceedings of the ASME Summer Heat Transfer*

Conference. 2005. San Francisco, CA, United States: American Society of Mechanical Engineers, New York, NY 10016-5990, United States.

10. Damm, D.L. and A.G. Fedorov, *Reduced-order transient thermal modeling for SOFC heating and cooling.* Journal of Power Sources, 2006. **159**(2): p. 956-967.
11. Ferguson, J.R., J.M. Fiard, and R. Herbin, *Three-dimensional numerical simulation for various geometries of solid oxide fuel cells.* Journal of Power Sources, 1996. **58**(2): p. 109.
12. Haynes, C., *Simulating process settings for unslaved SOFC response to increases in load demand.* Journal of Power Sources, 2002. **109**(2): p. 365.
13. Haynes, C. and W.J. Wepfer, *Design for power of a commercial grade tubular solid oxide fuel cell.* Energy Conversion and Management, 2000. **41**(11): p. 1123.
14. Iwata, M., et al., *Performance analysis of planar-type unit SOFC considering current and temperature distributions.* Solid State Ionics, 2000. **132**(3-4): p. 297.
15. Khaleel, M.A., et al., *A finite element analysis modeling tool for solid oxide fuel cell development: coupled electrochemistry, thermal and flow analysis in MARC(R).* Journal of Power Sources, 2004. **130**(1-2): p. 136.
16. Larrain, D., et al., *Generalized model of planar SOFC repeat element for design optimization.* 2004. **131**: p. 304.
17. Li, P.-W., L. Schaefer, and M.K. Chyu, *A numerical model coupling the heat and gas species' transport processes in a tubular SOFC.* Journal of Heat Transfer, 2004. **126**(2): p. 219.
18. Li, P.-W. and K. Suzuki, *Numerical Modeling and Performance Study of a Tubular SOFC.* Journal of the Electrochemical Society, 2004. **151**(4): p. 548-557.

19. Nagata, S., et al., *Numerical analysis of output characteristics of tubular SOFC with internal reformer.* Journal of Power Sources, 2001. **101**(1): p. 60.

20. Petruzzi, L., S. Cocchi, and F. Fineschi, *A global thermo-electrochemical model for SOFC systems design and engineering.* Journal of Power Sources, 2003. **118**(1-2): p. 96-107.

21. Sedghisigarchi, K. and A. Feliachi, *Dynamic and transient analysis of power distribution systems with fuel Cells-part I: fuel-cell dynamic model.* IEEE Transactions on Energy Conversion, 2004. **19**(2): p. 423.

22. Sudaprasert, K., R.P. Travis, and R.F. Martinez-Botas, *A computational fluid dynamics model of a solid oxide fuel cell.* Proceedings of the Institution of Mechanical Engineers, Part A (Journal of Power and Energy), 2005. **219**(A3): p. 159.

23. Bejan, A., *Advanced engineering thermodynamics*. 2nd ed. ed. 1997, New York :: J. Wiley & Sons.

24. Haynes, C. and W.J. Wepfer, *Characterizing heat transfer within a commercial-grade tubular solid oxide fuel cell for enhanced thermal management.* International Journal of Hydrogen Energy, 2001. **26**(4): p. 369.

25. Recknagle, K.P., et al., *Three-dimensional thermo-fluid electrochemical modeling of planar SOFC stacks.* Journal of Power Sources, 2003. **113**(1): p. 109-114.

26. Yakabe, H., et al., *3-D model calculation for planar SOFC.* Journal of Power Sources, 2001. **102**(1-2): p. 144-154.

27. Sciacovelli, A., *Thermodynamic optimization of a monolithic-type solid oxide fuel cell.* International Journal of Thermodynamics, 2010. **13**(3): p. 95-103.

28. Sciacovelli, A. and V. Verda, *Entropy generation minimization in a tubular solid oxide fuel cell.* Journal of Energy Resources Technology, Transactions of the ASME, 2010. **132**(1): p. 0126011-01260111.

29. Sciacovelli, A. and V. Verda, *Entropy generation analysis for the design optimization of solid oxide fuel cells.* International Journal of Numerical Methods for Heat and Fluid Flow, 2011. **21**(Compendex): p. 535-558.

30. Ordonez, J.C., et al., *Constructal flow structure for a single SOFC.* International Journal of Energy Research, 2007. **31**(Copyright 2008, The Institution of Engineering and Technology): p. 1337-57.

31. Al-Sulaiman, F.A., I. Dincer, and F. Hamdullahpur, *Exergy analysis of an integrated solid oxide fuel cell and organic Rankine cycle for cooling, heating and power production.* Journal of Power Sources, 2010. **195**(8): p. 2346-2354.

32. Amati, V., E. Sciubba, and C. Toro. *Exergy analysis of a solid oxide fuel cell-gas turbine hybrid power plant*. 2009. Boston, MA, United states: American Society of Mechanical Engineers.

33. Baniasadi, E. and I. Dincer, *Energy and exergy analyses of a combined ammonia-fed solid oxide fuel cell system for vehicular applications.* International Journal of Hydrogen Energy, 2011. **36**(17): p. 11128-11136.

34. Barelli, L., et al., *An energetic-exergetic comparison between PEMFC and SOFC-based micro-CHP systems.* International Journal of Hydrogen Energy, 2011. **36**(4): p. 3206-3214.

35. Calise, F., M. Dentice d'Accadia, and G. Restuccia, *Simulation of a tubular solid oxide fuel cell through finite volume analysis: Effects of the radiative heat transfer and exergy analysis.* International Journal of Hydrogen Energy, 2007. **32**(17): p. 4575-4590.

36. Calise, F., G. Ferruzzi, and L. Vanoli, *Parametric exergy analysis of a tubular Solid Oxide Fuel Cell (SOFC) stack through finite-volume model.* Applied Energy, 2009. **86**(11): p. 2401-2410.

37. Casas, Y., et al., *Energy and exergy analysis of an ethanol fueled solid oxide fuel cell power plant.* Chemical Engineering Journal, 2010. **162**(3): p. 1057-1066.

38. Dincer, I., M.A. Rosen, and C. Zamfirescu, *Exergetic performance analysis of a gas turbine cycle integrated with solid oxide fuel cells.* Journal of Energy Resources Technology, Transactions of the ASME, 2009. **131**(3): p. 0320011-03200111.

39. Douvartzides, S., F. Coutelieris, and P. Tsiakaras, *Exergy analysis of a solid oxide fuel cell power plant fed by either ethanol or methane.* Journal of Power Sources, 2004. **131**(1-2): p. 224-230.

40. Ghosh, S. and S. De, *Thermodynamic performance study of an integrated gasification fuel cell combined cycle: An exergy analysis.* Proceedings of the Institution of Mechanical Engineers, Part A: Journal of Power and Energy, 2003. **217**(6): p. 575-582.

41. Ghosh, S. and S. De, *First and second law performance variations of a coal gasification fuel-cell-based combined cogeneration plant with varying load.* Proceedings of the Institution of Mechanical Engineers, Part A: Journal of Power and Energy, 2004. **218**(7): p. 477-485.

42. Haseli, Y., I. Dincer, and G.F. Naterer, *Thermodynamic analysis of a combined gas turbine power system with a solid oxide fuel cell through exergy*. Thermochimica Acta, 2008. **480**(1-2): p. 1-9.

43. Haynes, C. and W.J. Wepfer, *Enhancing the performance evaluation and process design of a commercial-grade solid oxide fuel cell via exergy concepts.* Journal of Energy Resources Technology, Transactions of the ASME, 2002. **124**(2): p. 95-104.

44. Hotz, N., S.M. Senn, and D. Poulikakos, *Exergy analysis of a solid oxide fuel cell micropowerplant*. Journal of Power Sources, 2006. **158**(1): p. 333-347.

45. Leal, E.M. and J. Brouwer, *A thermodynamic analysis of electricity and hydrogen co-production using a solid oxide fuel cell.* Journal of Fuel Cell Science and Technology, 2006. **3**(2): p. 137-143.

46. Odukoya, A., I. Dincer, and G.F. Naterer, *Exergy analysis of a gasification-based combined cycle with solid oxide fuel cells for cogeneration.* International Journal of Green Energy, 2011. **8**(8): p. 834-856.

47. Rashidi, R., I. Dincer, and P. Berg, *Energy and exergy analyses of a hybrid molten carbonate fuel cell system.* Journal of Power Sources, 2008. **185**(2): p. 1107-1114.

48. Rosen, M.A., *Comparison based on energy and exergy analyses of the potential cogeneration efficiencies for fuel cells and other electricity generation devices.* International Journal of Hydrogen Energy, 1990. **15**(4): p. 267-274.

49. Wang, J., et al. *Thermodynamic analysis of an integrated power generation system driven by solid oxide fuel cell*. 2012. Langford Lane, Kidlington, Oxford, OX5 1GB, United Kingdom: Elsevier Ltd.

50. Wongchanapai, S., et al., *Selection of suitable operating conditions for planar anode-supported direct-internal-reforming solid-oxide fuel cell.* Journal of Power Sources, 2012. **204**: p. 14-24.

51. Liu, S., C. Song, and Z. Lin, *The effects of the interconnect rib contact resistance on the performance of planar solid oxide fuel cell stack and the rib design optimization.* Journal of Power Sources, 2008. **183**(1): p. 214-225.

52. Nelson, G.J. and C.L. Haynes, *Continuum-level solid oxide electrode constriction resistance effects.* Journal of Power Sources, 2008. **185**(2): p. 1168-1178.

53. Liu, S., W. Kong, and Z. Lin, *Three-dimensional modeling of planar solid oxide fuel cells and the rib design optimization.* Journal of Power Sources, 2009. **194**(2): p. 854-863.

54. Selimovic, A., et al., *Steady state and transient thermal stress analysis in planar solid oxide fuel cells.* Journal of Power Sources, 2005. **145**(2): p. 463-469.

55. Lin, C.-K., et al., *Thermal stress analysis of a planar SOFC stack.* Journal of Power Sources, 2007. **164**(1): p. 238-251.

56. Divisek, J., R. Jung, and I.C. Vinke, *Structure investigations of SOFC anode cermets. Part II: Electrochemical and mass transport properties.* Journal of Applied Electrochemistry, 1999. **29**(2): p. 165-170.

57. Chan, S.H., K.A. Khor, and Z.T. Xia, *Complete polarization model of a solid oxide fuel cell and its sensitivity to the change of cell component thickness.* Journal of Power Sources, 2001. **93**(1-2): p. 130-140.

58. Ackmann, T., et al., *Modeling of mass and heat transport in planar substrate type SOFCs.* Journal of the Electrochemical Society, 2003. **150**(6): p. A783-A789.

59. Muller, A.C., et al. *Characterization of multilayer anodes for SOFC*. 2003. Boston MA, United states: Materials Research Society.

60. Yoon, S.P., et al., *Improvement of anode performance by surface modification for solid oxide fuel cell running on hydrocarbon fuel.* Journal of Power Sources, 2004. **136**(1): p. 30-36.

61. Laurencin, J., et al., *Thermo-mechanical model of solid oxide fuel cell fed with methane.* Fuel Cells, 2006. **6**(1): p. 64-70.

62. Gross, M.D., J.M. Vohs, and R.J. Gorte, *A strategy for achieving high performance with SOFC ceramic anodes.* Electrochemical and Solid-State Letters, 2007. **10**(4): p. B65-B69.

63. Gross, M.D., J.M. Vohs, and R.J. Gorte, *An examination of SOFC anode functional layers based on ceria in YSZ.* Journal of the Electrochemical Society, 2007. **154**(7): p. B694-B699.

64. Kim, S.-D., et al., *Effects of anode and electrolyte microstructures on performance of solid oxide fuel cells.* Journal of Power Sources, 2007. **169**(2): p. 265-270.

65. Kong, J., et al., *Ni-YSZ gradient anodes for anode-supported SOFCs.* Journal of Power Sources, 2007. **166**(2): p. 337-342.

66. Lee, Y.H., et al. *Influence of anode thickness on cell performance in internal reforming operation of SOFCs*. 2007. Montreal, QC, Canada: Electrochemical Society Inc.

67. Magar, Y.N. and R.M. Manglik, *Modeling of convective heat and mass transfer characteristics of anode-supported planar solid oxide fuel cells.* Journal of Fuel Cell Science and Technology, 2007. **4**(2): p. 185-193.

68. Son, H.-J., et al. *Effect of anode support thickness on the performance of tubular SOFCs*. 2007. Japan: Electrochemical Society Inc.

69. Wang, G., et al., *3-D model of thermo-fluid and electrochemical for planar SOFC.* Journal of Power Sources, 2007. **167**(2): p. 398-405.

70. Chen, K., et al., *Performance of an anode-supported SOFC with anode functional layers.* Electrochimica Acta, 2008. **53**(27): p. 7825-7830.

71. DeCaluwe, S.C., H.Y. Zhu, and G.S. Jackson. *The predicted effects of anode microstructure on SOFC overpotentials*. 2008. Washington, DC, United states: Electrochemical Society Inc.

72. Zhou, L., et al., *Performance of an anode-supported tubular solid oxide fuel cell (SOFC) under pressurized conditions.* Electrochimica Acta, 2008. **53**(16): p. 5195-5198.

73. Bhattacharyya, D. and R. Rengaswamy, *Transport, sensitivity, and dimensional optimization studies of a tubular Solid Oxide Fuel Cell.* Journal of Power Sources, 2009. **190**(2): p. 499-510.

74. Liu, S., W. Kong, and Z. Lin, *A microscale modeling tool for the design and optimization of solid oxide fuel cells.* Energies, 2009. **2**(2): p. 427-444.

75. Wang, Z., et al., *Improved SOFC performance with continuously graded anode functional layer.* Electrochemistry Communications, 2009. **11**(6): p. 1120-1123.

76. Xia, W., Y. Yang, and Q. Wang, *Effects of operations and structural parameters on the one-cell stack performance of planar solid oxide fuel cell.* Journal of Power Sources, 2009. **194**(2): p. 886-898.

77. Lima da Silva, A. and I.L. Muller, *Operation of solid oxide fuel cells on glycerol fuel: A thermodynamic analysis using the Gibbs free energy minimization approach.* Journal of Power Sources, 2010. **195**(17): p. 5637-5644.

78. Menzler, N.H. and V.A.C. Haanappel, *Influence of anode thickness on the power output of solid oxide fuel cells with (La,Sr)(Co,Fe)-type cathode.* Journal of Power Sources, 2010. **195**(16): p. 5340-5343.

79. Zuo, N., et al. *Fabrication and characterization of large size anode substrate of solid oxide full cell*. 2010. Harbin, China: Trans Tech Publications.

80. Akhtar, N., et al., *Modeling of Co-planar type single-chamber solid oxide fuel cells.* Journal of Fuel Cell Science and Technology, 2011. **8**(4).

81. Farhad, S. and F. Hamdullahpur, *Micro-modeling of porous composite anodes for solid oxide fuel cells.* AIChE Journal, 2012. **58**(6): p. 1893-1906.

82. Kuo, J.-K. and J.-K. Wang, *Characteristic simulation with various anode support thicknesses of membrane electrode assembly in SOFC.* Journal of Solid State Electrochemistry, 2012. **16**(1): p. 329-340.

83. Mukhopadhyay, M., et al. *Engineered anode structure for enhanced electrochemical performance of anode-supported planar solid oxide fuel cell*. 2012. Langford Lane, Kidlington, Oxford, OX5 1GB, United Kingdom: Elsevier Ltd.

84. Park, J., J. Bae, and J.-Y. Kim, *A numerical study on anode thickness and channel diameter of anode-supported flat-tube solid oxide fuel cells.* Renewable Energy, 2012. **42**: p. 180-185.

85. Park, Y.M., et al. *Effect of anode thickness on impedance response of anode-supported solid oxide fuel cells*. 2012. Langford Lane, Kidlington, Oxford, OX5 1GB, United Kingdom: Elsevier Ltd.

86. Sciacovelli, A., *Thermodynamic optimization of a monolithic-type solid oxide fuel cell.* International Journal of Thermodynamics. **13**(3): p. 95-103.

87. Bejan, A., *Thermal design and optimization*, ed. G. Tsatsaronis and M.J. Moran. 1996, New York :: John Wiley.

88. Keeney, R.L., *Value-focused thinking : a path to creative decisionmaking*. 1st Harvard University Press pbk. ed. ed. 1996, Cambridge, Mass. :: Harvard University Press.

89. Hughes, D., et al. *A Real-Time Spatial SOFC Model for Hardware-Based Simulation of Hybrid Systems*. in *Proceedings of ASME 2011 5th International Conference on Energy Sustainability & 9th Fuel Cell Science, Engineering and Technology Conference*. 2011.

90. Incropera, F.P. and D.P. DeWitt, *Fundamentals of Heat and Mass Transfer*. 5th ed. 2002, New York: John Wiley and Sons.

91. Li, M., D.P. James, and B. Jacob, *A Finite Volume SOFC Model for Coal-Based Integrated Gasification Fuel Cell Systems Analysis*. Journal of Fuel Cell Science and Technology, 2010. **7**(4): p. 041017.

92. Liese, E.A., et al. *A Dynamic Bulk SOFC Model Used in a Hybrid Turbine Controls Test Facility*. in *2006 ASME 51st Turbo Expo, May 6, 2006 - May 11, 2006*. 2006. Barcelona, Spain: American Society of Mechanical Engineers.

93. Li, M., et al., *A Finite Volume SOFC Model For Coal-Based Integrated Gasification Fuel Cell System Analysis*, in *ASME 7th International Fuel Cell Science, Engineering and Technology Conference*, ASME, Editor 2009, ASME: Newport Beach, CA.

94. Li, M., et al., *A Finite Volume SOFC Model For Coal-Based Integrated Gasification Fuel Cell System Analysis.* Journal of Fuel Cell Science and Technology, 2010.

95. Yakabe, H., et al., *Evaluation and Modeling of Performance of Anode-Supported Solid Oxide Fuel Cell.* Journal of Power Sources, 2000. **86**: p. 9.

96. Perry, R. and D. Green, *Perry's Chemical Engineer's Handbook.* 7th ed. 1997, New York, NY: McGraw-Hill.

97. Cayan, F.N., et al., *On Modeling Multi-Component Diffusion Inside the Porous Anode of Solid Oxide Fuel Cells Using Fick's Model.* Journal of Power Sources, 2009. **192**(2): p. 467-474.

98. Hernandez-Pacheco, E., et al., *A Cell-Level Model for a Solid Oxide Fuel Cell Operated with Syngas from a Gasification Process.* International Journal of Hydrogen Energy, 2005. **30**(11): p. 1221-1233.

99. Noren, D.A. and M.A. Hoffman, *Clarifying the Butler-Volmer Equation and Related Approximations for Calculating Activation Losses in Solid Oxide Fuel Cell Models.* Journal of Power Sources, 2005. **152**(Compendex): p. 175-181.

100. Campanari, S. and P. Iora, *Comparison of Finite Volume SOFC Models for the Simulation of a Planar Cell Geometry.* Fuel Cells, 2005. **5**(Compendex): p. 34-51.

101. Costamagna, P., et al., *Electrochemical Model of the Integrated Planar Solid Oxide Fuel Cell (IP-SOFC).* Chemical Engineering Journal, 2004. **102**(1): p. 61-69.

102. ThyssenKrupp, *Crofer22APU Material Data Sheet No. 4046*, ThyssenKrupp, Editor 2010, ThyssenKrupp: Werdohl, Germany.

103. Achenbach, E., *SOFC Stack Modeling, Final Report of Activity A2, Annex II: Modeling and Evaluation of Advanced Solid Oxide Fuel Cells, International Energy Agency*

Programme on R, D&D on Advanced Fuel Cells, 1996, International Energy Agency: Juelich, Germany.

104. *JMatPro*, 2005, Sente Software Ltd., Surrey Technology Centre: United Kingdon.

105. Evans, N.D., et al., *Microstructure evolution of alloy 625 foil and sheet during creep at 750 °C.* Materials Science and Engineering: A, 2008. **498**(1-2): p. 412-420.

106. Hughes, D.O., et al., *Transient Behavior of a Fuel Cell/Gas Turbine Hybrid Using Hardware Based Simulation With a 1-D Distributed Fuel Cell Model*, in *International Colloquium on Environmentally Preferred Advanced Power Generation*, ASME, Editor 2010, ASME: Costa Mesa, CA. p. 10.

107. KakacÌ§, S., R.K. Shah, and W. Aung, *Handbook of single-phase convective heat transfer*, ed. S. KakacÌ§, R.K. Shah, and W. Aung. 1987, New York :: Wiley.

108. Achenbach, E., *Three-Dimensional and Time-Dependent Simulation of a Planar Solid Oxide Fuel Cell Stack.* Journal of Power Sources, 1994. **49**(Compendex): p. 333-348.

109. Modest, M.F., *Radiative heat transfer*. 2nd ed. ed. 2003, San Diego, Calif. :: Academic.

110. Press, W.H., *Numerical recipes in C : the art of scientific computing*. 2nd ed. ed, ed. W.H. Press. 1992, Cambridge [Cambridgeshire] ;: Cambridge University Press.

111. Turns, S.R., *An Introduction to Combustion: Concepts and Applications*. Second ed. 2002: Mc-Graw Hill.

112. Kays, W. and M. Crawford, eds. *Convective Heat and Mass Transfer*. 1993, McGraw-Hill. 480.

113. Nikooyeh, K., A.A. Jeje, and J.M. Hill, *3D modeling of anode-supported planar SOFC with internal reforming of methane.* Journal of Power Sources, 2007. **171**(2): p. 601-609.